HOMOGENIZATION AND BRIDGING MULTI-SCALE METHODS FOR THE DYNAMIC ANALYSIS OF PERIODIC SOLIDS

A Thesis
Presented to
The Academic Faculty

by

Stefano Gonella

In Partial Fulfillment
of the Requirements for the Degree
Doctor of Philosophy
in the School of Aerospace Engineering

Georgia Institute of Technology
August 2007

HOMOGENIZATION AND BRIDGING MULTI-SCALE METHODS FOR THE DYNAMIC ANALYSIS OF PERIODIC SOLIDS

Approved by:

Professor Massimo Ruzzene, Advisor
School of Aerospace Engineering
Georgia Institute of Technology

Professor Laurence J. Jacobs
School of Civil and Environmental Engineering
Georgia Institute of Technology

Professor Sathya V. Hanagud
School of Aerospace Engineering
Georgia Institute of Technology

Professor David L. McDowell
School of Mechanical Engineering
Georgia Institute of Technology

Professor Dewey H. Hodges
School of Aerospace Engineering
Georgia Institute of Technology

Date Approved: 18 April 2007

This is dedicated to La Tipografica

where mum and dad taught me

the passion for hard work

the love for beauty

and the desire to achieve great things

ACKNOWLEDGEMENTS

Almost four years have elapsed since that hot and humid Monday August 4^{th} 2003, when I landed at Hartsfield International with my heart filled with a mixture of gloominess and enthusiasm. It was not going to be easy, for America, to live up to the expectations. To confirm the mythology of her that I had been nurturing inside my head. To match the degree of affection for her that I had built upon a few inspiring childhood memories and one huge philosophical belief. But America did speak to my soul beyond expectations, and so did the splendid ATL, that I now call home, and this phenomenal school that makes me so proud to be a ramblin' wreck.

All along this journey, I have been thrusted by the support of the most outstanding, creative, committed and caring people. An inspired and determined advisor, who always made sure that the goals that I was setting for my work were as high and as compelling as my dreams. Some truly special professors, versed teachers all the while mentors, to whom I am grateful, among other things, for having interpreted my many unrelenting and loud talks as sincere symptoms of my passion. My new American friends, those who were born American as well as those who have been here for so long that they have embraced this place as their own: I owe them my survival during the inevitable tough times of graduate school and a big chunk of the fun that I have had over past four years. And, of course, the good friends back home, those who correctly realized, since the beginning, the spiritual relevance of the adventure that I was about to undertake.

And, above all, the one person without whom there would be no America, because America has always been the name of my boldest and most precious gift to her.

Thank you all

TABLE OF CONTENTS

LIST OF TABLES

LIST OF FIGURES

CHAPTER I

INTRODUCTION

1.1 Overview

The objective of this work is the investigation of the dynamic behavior of periodic media through the application of homogenization techniques in conjunction with multi-scale analysis. This introductory chapter is intended to serve two purposes. First, we want to introduce the concept of periodic media, providing a general definition along with some inherent vocabulary and showing some examples out of the natural and technical fields. The properties of periodic assemblies that make this kind of structures appealing from a technological standpoint are also highlighted. Although the discussion of such properties is not a direct objective of this work, they will be mentioned in the following chapters when highlighted by the results of the numerical analysis. Then, we intend to provide an overview on the field of multi-scale analysis and homogenization, through reference to some of the most influential contributions, from the pioneering work to present techniques.

1.2 Periodic Media and Their Properties

1.2.1 Definition of periodic medium and repetitive volume element

Periodic structures can be defined as heterogeneous domains with a characteristic recursive pattern obtained through the translation in space of a repetitive element called elementary unit cell or repetitive volume element (RVE). The bi-material truss of fig. 1 is an example of the kind of periodic assemblies studied in this work. Unit cells feature different levels of structural complexity, according to shape and composition of the medium. The more complex the pattern of the medium the higher the complexity and/or the size of the representative unit cell. Several considerations about the behavior of a periodic assembly can be made through a simple unit cell analysis, and are therefore independent from the size of the domain or the number of unit cells it contains.

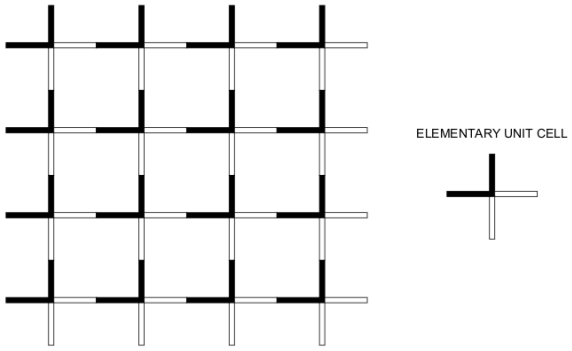

Figure 1: Periodic structure with highlighted unit cell

1.2.2 Periodic structures of engineering interest

Structures featuring periodicity are very common both in nature and among man-made artifacts. Some natural periodic systems have been observed since the dawn of times and have served as a source of inspiration for hi-tech applications. The honeybee cells of fig. 2.a

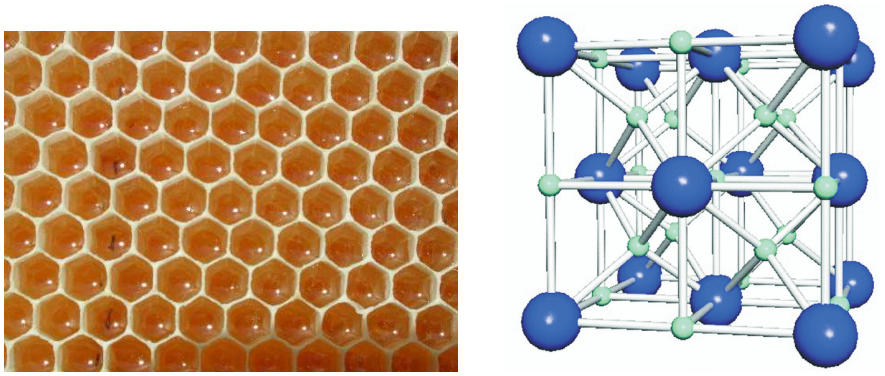

(a) Honeybee cells (b) Iron-carbon lattice architecture

Figure 2: Examples of natural periodic structures

are an example of an efficient periodic architecture that has been imported from the natural into the technical world without major modifications. Periodic patterns are also very common in chemistry and biology. Crystalline solids, for example, are known to feature a periodic geometry based on the repetition of unit cells. Typically, crystals are described as lattices whose nodal positions are occupied by atoms (fig. 2.b). Several biological systems feature periodicity as well. Figures 3.a and 3.b, for example, show the periodic distribution

of subunits in a lattice protein.

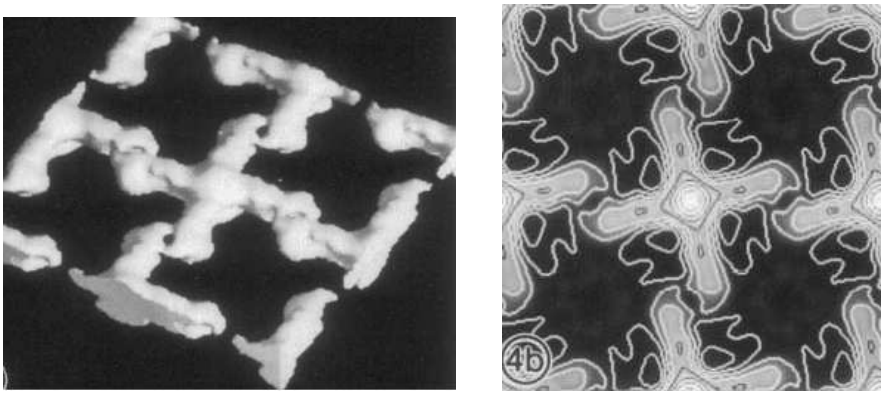

(a) 3D visualization of subunits in a lattice protein

(b) Periodic pattern of subunits in a lattice protein

Figure 3: Examples of periodic structures in biology (from *Journal of Bacteriology* vol. 169 n.12)

Classical engineering widely employs periodic structures. Civil engineering applications, for example, include trusses and frames of beams, which are used in the majority of large steel constructions (see fig. 4). Modern engineering has exploited periodic media to produce advanced materials and to design structures with superior performance. The aerospace industry has often pioneered the research on these innovative concepts. In the case of aeronautical engineering, weight is a fundamental criterion for the design of structures. More precisely, the strength-to-weight ratio is the critical parameter that defines the efficiency of a structural configuration. Composite materials represent an important example of periodic

Figure 4: Bridge with steel truss architecture

structures developed within the aerospace industry and later exported to other fields. Composites are known to offer a great trade-off between excellent mechanical properties and low weight and are therefore progressively replacing aluminum alloys for many structural aircraft components. The ultimate establishment of this technology took place with the design of the Boeing 787 which features as much as 50% of the airframe made of composites. The family of composite materials is extremely broad and diversified: among composites with obvious periodicity are woven composites, honeycomb-based assemblies, sandwich panels and fiber reinforced matrix plates. Woven composites (fig. 5.a) are inspired by fabrics and

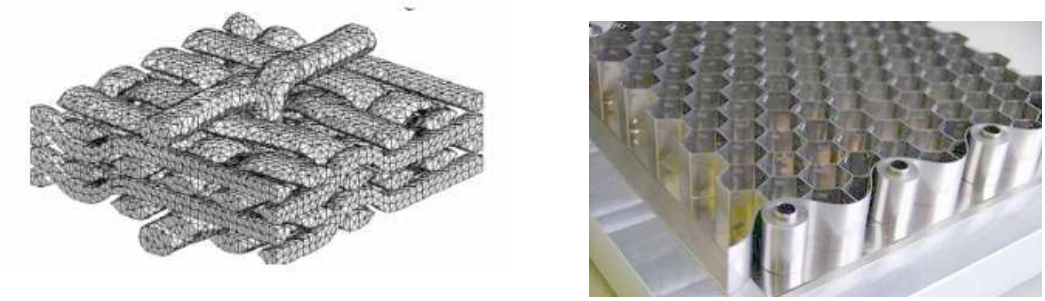

(a) Material-like woven composite (b) Honeycomb structure

Figure 5: Examples of periodic composite materials

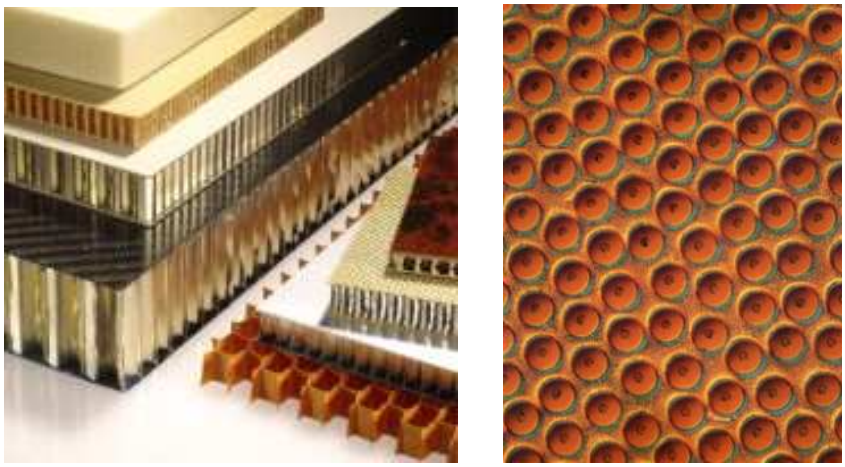

(a) Sandwich panels (b) Fiber-reinforced composite

Figure 6: Examples of periodic composite materials

derive their strength from the dense web of flexible polymeric wires. Honeycombs (fig. 5.b)

are commonly used in the aerospace industry, where their extremely low weight and good resistance to shear loads is exploited for the core of blades and wing sections. Honeycombs are often used in conjunction with standard thin metal structures to produce sandwich panels (fig. 6.a), that combine the properties of regular honeycombs with an improved resistance to bending loads. Finally, fiber-reinforced composites, with high resistance fibers dispersed in a generally more ductile matrix (fig. 6.b), can improve the strength of standard polymeric and metal structures, while containing the overall weight. Based on the

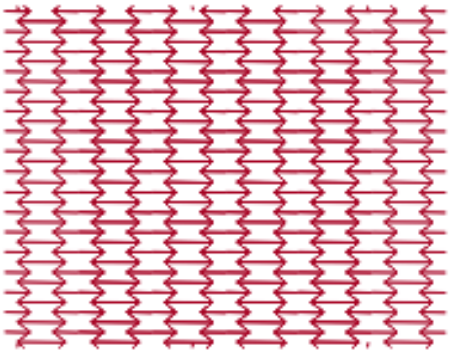

(a) Periodic pattern in an auxetic material

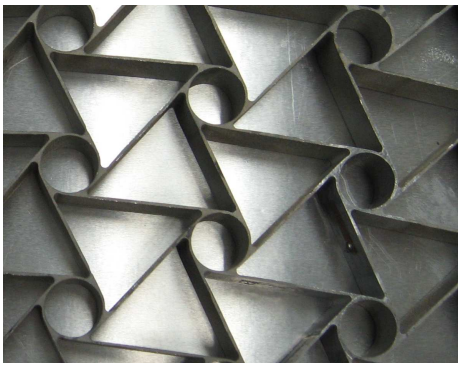

(b) Sandwich panel with chiral honeycomb core

Figure 7: Examples of auxetic materials

success of standard honeycomb and sandwich architectures, that are now widely used in the industry, some other periodic assemblies have been suggested featuring specific mechanical properties. Among these advanced configurations are the so-called auxetic lattices [37, 74], which feature a negative Poisson's ratio, and chiral honeycombs [44]. The unique static and dynamic properties of this class of materials are still under investigation. Lastly, prismatic materials (fig. 8.a) and lattice block materials (fig. 8.b) derive their strength characteristics from their structure of highly ordered internal tetrahedra. They can be manufactured in steel, aluminum, plastics, rubber or ceramics. The technological feature that makes lattice block materials very appealing is the nearly optimal strength-to-weight ratio. Lattice structures feature an interesting filtering behavior and can be used as vibration absorption devices.

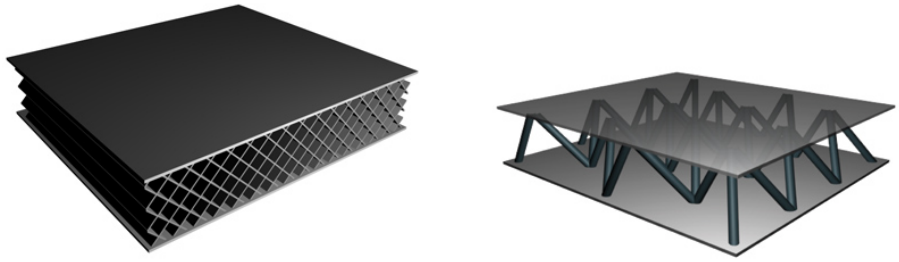

(a) Prismatic material (b) Truss-core sandwich configuration

Figure 8: Examples of lattice blocks

1.2.3 General considerations on the repetitive volume elements

The unit cell of a periodic domain is not always uniquely defined. The selection of the most suitable unit cell to describe a periodic domain is often based on convenience considerations: for instance, it is important to make sure that the selected unit cell is irreducible, i.e. the smallest repetitive unit identifiable in the domain carrying all the geometric features necessary to fully define the medium [10]. Figure 9 shows a periodic structure (a flat panel with circular holes) and two possible unit cells: both cells can be interpreted as repetitive volume elements, but only the first one is irreducible in the sense of the definition given above.

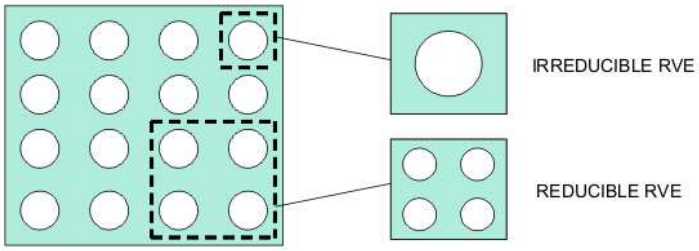

Figure 9: Plate with holes - Irreducible and reducible RVEs

On the other hand, the same periodic structure can be interpreted as the repetition of more than one unit cell with different geometry and structure and yet similar dimensions and level of complexity. For example, both repetitive volume elements shown in fig. 10 are

suitable elementary unit cells. However, sometimes one is better than the other as far as getting the mathematical analysis more manageable. The selection of the best RVE is based on considerations related to the particular application, the nature of the problem and the kind of analysis needed.

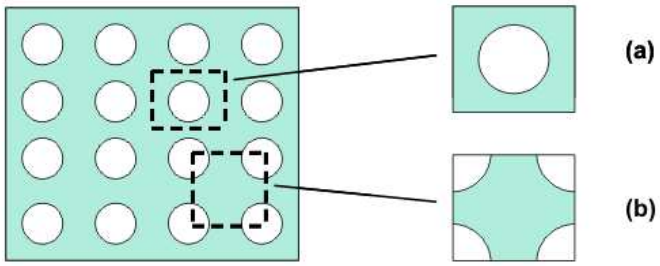

Figure 10: Plate with holes - Two possible RVE choices

1.2.4 Classical analyses of periodic assemblies

Periodic structures have been the object of extensive scientific investigation, aiming both at understanding the behavior of natural systems with periodicity and at designing materials with specified properties. Periodic assemblies feature in fact some unique dynamic characteristics that can be exploited for a variety of applications. An interesting peculiarity in periodic structures is that wave propagation only occurs over specific frequency bands known as 'pass bands', while significant attenuation occurs over other regions of the frequency domain called 'stop bands' or 'band gaps'. The spectral width and location of these bands are dependent upon the geometry and the topology of the unit cell. The phenomenon of band gaps in periodic structures has been widely investigated, for example by Sigmund, Jensen and coworkers [78] and Hussein et al. [36] among others.

A big effort has also been placed in the definition of equivalent mechanical properties for periodic media, in order to conduct the analysis of these structures with the same tools used for homogeneous media. The core of this approach falls into the class of homogenization methods discussed in the next section. Composites led the way for this type of analysis: equivalent static material properties, such as equivalent stiffnesses are now available for

composite materials such as fiber reinforced matrices and reinforced panels as well as for honeycomb materials [26].

1.3 Homogenization and Multi-scale Solution Approaches

1.3.1 Multi-scale methods

Periodic assemblies are a special class of heterogeneous structures. In order to conduct a numerical analysis of this kind of structures, the grid scale used for the numerical scheme needs to be sufficiently small to capture the effects of the individual constituents within the periodic pattern. Hence, the size of the spatial discretization is dictated by the size of the microstructure, which may result in a formidable computational problem. From here the need to develop techniques which make the analysis of periodic structures more manageable, while maintaining the fidelity of the results. This goal can be achieved by making a distinction between macro-scale and micro-scale within the assembly, keeping in mind what are the pieces of information that compete to each of them. This is generally the approach of the so-called multi-scale methods. The fundamentals of such techniques are given in [4, 12, 16, 70, 72] and are based on the idea of global-local analysis. While the local analysis focuses on the peculiarities of the domain that actually make the medium heterogeneous, the global analysis predicts the *global* behavior of the complete structure, without dealing with the details at the microstructural level. The distinctive idea behind global-local methods is to bridge the two analyses enriching one with the other. For example, with loading inputs from the global problem, the local model can recover the effects of the microstructure on the mechanical response. Conversely, with geometric and constitutive characteristics from the local problem, the microstructure can be successfully embedded into the global problem.

1.3.2 The homogenization method

Homogenization methods can be classified as global-local techniques. They are based on the following fundamental assumptions. First of all, the structure must be periodic, according to the definition given in the previous paragraph, i.e. it can be considered as a spatial repetition of RVEs. Accordingly, the exact solution of the dynamic problem is to be searched among

spatially periodic solutions. Also, the macroscopic fields are assumed to be constant within a single RVE, which means that the RVE has to be small enough to be independent from any macroscopic variation of the structure. Typically, these assumptions are valid far from the boundary of the domain of interest and when the size of the microstructure is significantly smaller than the wavelength of the considered response.

The homogenization method itself consists in replacing an heterogeneous periodic domain with an equivalent homogeneous continuum whose behavior approximates, to some extent, that of the original assembly. Mathematically speaking, this translates into describing the elastomechanics of the periodic medium in terms of one or more partial differential equations and a set of consistent boundary conditions. The formulation of the homogeneous field equations is based on a unit cell analysis that accounts for the geometry and internal organization of the repetitive element.

1.3.3 Literature review of homogenization techniques

Homogenization was first introduced in the 1970s for the solution of static problems involving elliptic partial differential equations. The theoretical fundamentals of this technique can be found in the works of Lions [48], Bensoussan et al. [7], Bakhvalov et al. [3] and Sanchez-Palencia [75]. Recent works in the field have been oriented towards the numerical evaluation of the boundary value problems deriving from the application of the homogenization approach to periodic domains. The finite element method, in particular, has been often chosen as the reference method to solve the homogenized equations of motion. Guedes [28] and Kikuchi [34] were among the first to implement a finite element analysis for the homogenization of the governing equations of elasticity.

Homogenization has proven to be sufficiently accurate for the investigation of static problems for most engineering applications. Homogenized static mechanical properties have in fact been found and used for several families of periodic assemblies. For instance, equivalent Young's moduli, calculated along different directions, are available in the literature for fiber reinforced composites, honeycomb structures and sandwich panels [26]. Stochastic cellular solids, such as foams, can be also approximated with deterministic periodic models

and therefore studied from the homogenization point of view. For this class of materials, equivalent values for stiffness are tabled as functions of some parameters like temperature or density. Wood, which is an extremely common natural composite material, has also been extensively studied and its average properties are also available in the literature. Several multi-material structures, both one-dimensional and two-dimensional, have been investigated in the attempt to derive equivalent properties. Hassani and coworkers [30, 31, 32] have conducted detailed studies of multi-material plates with different layer configurations. Research is also being conducted to determine equivalent mechanical properties for auxetic materials and chiral honeycombs [44]. Another popular homogenization technique is the quasi-continuum method [43, 77, 76, 61, 60, 83]. It was first introduced by Ortiz, Phillips and Tadmor at Brown University where the method was applied to single crystal f.c.c. metals and shown to reproduce lattice static results for a variety of line and surface defects and used to study nanoindentation in thin films. Additional research in the field was then added by Shenoy, Miller and Rodney among others [61, 60].

The homogenization techniques for dynamic problems are still quite unexplored. Finding equivalent continuous differential equations for the full elastodynamic problem turns out to be a challenging task if compared with the calculation of equivalent stiffness or density. Fish et al. [20, 21] worked on expansion homogenization methods showing that higher order expansions are needed to capture accurately the dynamic behavior of structures. More precisely, they investigated the propagation of longitudinal waves in bi-material rods with constant cross section and showed that the *order zero* expansion, corresponding to the rule of mixtures and typically sufficient for static analysis, fails to capture the dispersive behavior of the bar. On the basis of this analysis, they also suggested a correction of the classical rule of mixtures to account for dynamic behavior. A big advancement in the field of dynamic homogenization is due to research on composite materials. In the late 1960s, Sun and coworkers [82] introduced the concept of *effective stiffness* for the dynamic analysis of laminated media and unidirectional fiber-reinforced composites. During the early 1970s, Hegemier et al. [64] developed a binary mixture theory for the analysis of waveguide-type propagation for that same class of materials. More recently, Murakami et al.

[62, 63] constructed dispersive continuum models for angle-ply laminates with orthotropic lamina, fiber reinforced media and particulate composites. In spite of all these outstanding results, a definitive computational methodology to obtain a dispersive elastodynamic model for complex structures is still not available. Some recent research, like that of McDevitt, Kikuchi and coworkers [58], has tried to fill this gap.

A peculiar approach to dynamic homogenization was developed between the late 1990s and the early 2000s at the University of Texas at Austin and is described in the works by Oden [67], Babuska [2] and Martinsson et al. [53, 54, 55], where the theoretical layout of the method is fully detailed and the application to lattices is described. The spatial periodicity of lattices is exploited to obtain dynamic equilibrium equations in the Fourier domain. This latter approach is embraced in this work and applied to describe both wave motion and harmonic behavior of simple periodic lattice structures. Some other periodic structures that do not exactly qualify as lattices, like multi-material solids and frames of beam elements, are also addressed in accordance to the technique. In particular, the effectiveness of the homogenized models in predicting the harmonic response of finite one-dimensional and two-dimensional domains and a strategy for refining the accuracy of the technique are added with respect to the investigation of [53, 54, 55].

1.3.4 Beyond multi-scale analysis

A very new and quite unexplored approach to the analysis of periodic domains is based on the concept of multi-cell analysis. The inspiration is derived from the classical unit-cell based approach widely used for periodic structures. The main idea, now, is to conduct the same kind of analysis on larger non irreducible repetitive elements (macro-cells). This allows capturing the behavior of the structure both in the long as well as in the short wavelength domain. Among the first to develop this approach are Dmitriev, Vasiliev, Miroshnichenko and coworkers, who have described the basic rules for multi-cell analysis in [86] (where the method is called multi-field analysis), and applied it to a Cosserat solid [85]. In [86] and [85], the multi-cell approach is only applied to lumped parameters systems for applications

to molecular dynamics, and no use of any multi-scale analysis is done to bridge the microstructure solution with macroscopic structural dynamics. Part of the contribution of the present work is trying to integrate multi-scale and multi-cell analysis into a comprehensive technique.

1.4 The Bridging Multi-scale Method

1.4.1 Genesis and objectives of the method

An interesting multi-scale approach was introduced by researchers at Nortwestern University on the basis of the pioneering research by Liu, Belytschko and coworkers [87, 51, 50, 49, 38, 39, 92, 42, 88, 68, 40, 89]. This technique goes under the name of bridging multi-scale method [92, 38, 88] and was designed with the objective of partitioning a given structural domain using multiple discretizations with different levels of details. This allows capturing the global behavior of the structure at a low computational cost through a coarse-scale discretization while, at the same time, achieving a detailed description of local behavior through a fine-scale discretization of a local region. According to the definition given above, the bridging method qualifies as a global-local technique. A natural application of this method is to investigate localization problems, such as cracks, inclusions and sudden variations of the material properties, thanks to its capability to provide high-fidelity analysis of localized phenomena within a global framework. Among the tools required to implement the bridging multi-scale method, the definition of non-reflective interface conditions [89] at the boundary between the scales plays a key role. The method also considers the microstructure as periodic and applies the Fourier Transform [42] in a similar fashion as presented in [53, 54, 55].

1.4.2 Characteristics and limitations of the method

The bridging scales method was developed with an eye to rising issues in nanotechnology and MEMS [41]. Purely physiological matters such as vascular flow and blood rheology and problems of biology like cell migration and cell-substrate adhesion can nowadays be tackled through a multi-scale approach. Because of the extremely small size of the microstructure in this kind of applications, the fine-scale analysis is typically carried out at the atomistic

or molecular level, while a continuum representation is left for a coarse-scale analysis of the macrostructure. The intention is here to apply the method systematically to structures with different levels of complexity.

1.5 Motivations and Objectives

Several components of industrial applications can be classified as periodic structures. Most of these structures are analyzed experimentally: among the classical experimental investigations, wave-based non-destructive methods, for instance, are widely used for health monitoring purposes to inspect regions of the structure that cannot be observed by naked eye. The interpretation of experimental results is not always straightforward and must be supported by analytical or numerical models. Typically, analytical models can be obtained only for simple configurations and require advanced mathematical tools for their solution. Numerical modelling, on the other hand, is dominated by the issue of computers speed and memory. Since computational models for periodic structures require detailed discretizations of the domain, the problem of reducing the size of the numerical model seems to be of major concern for people working on this kind of assemblies and definitely represents the number one motivation behind the development of the homogenization method.

While static homogenization is a fairly established theory, with plenty of available results in the literature, dynamic homogenization still needs to be definitively compounded and interesting results have been only found for a limited number of applications. A first objective of this work is to explore the potentials of dynamic homogenization for the approximation of the dynamic response and for wave propagation analysis of periodic lattices and lattice-like structures. The theoretical approach used for this task is derived from the work of Martinsson [54] with the following advancements. While the mathematical tools are mostly borrowed from his work, we are here primarily interested in practical considerations about the performance of the method to get approximate solutions. Specifically, we try to obtain approximate frequency response functions and dispersion relations. The most original contribution to the mathematical layout of the method is a technique to refine standard homogenization approximation, based on the exploitation of the exact dispersion

relations. This technique allows stretching considerably the region of the frequency domain where good agreement between exact and approximate solutions is observed. An alternative formulation is also introduced to simplify the implementation of the technique. Taylor series expansions are performed to convert discretized equations of motion into equivalent continuous ones, which approximate the behavior of the periodic domain in the low frequency, long wavelength regime. It will be shown that this operation based on Taylor series expansion is equivalent to the Fourier-based analysis of the periodic domain, while considerably simplifying its numerical implementation.

One of the problems with homogenization techniques lies in the fact that approximations usually work exclusively in the long wavelength/low frequency domain. This becomes a major limitation as some peculiar phenomena of periodic structures take place at higher frequencies. Bandgaps, for example, which are unique to this class of media, and extremely interesting from an engineering standpoint, typically occur at higher frequencies and cannot be captured by homogenized models. The multi-cell analysis, as implemented in this work, is a tool to eliminate this constraint and stretch the potentials of standard homogenization towards a broader frequency range. The analysis presented here takes inspiration from the multi-field technique of Vasiliev and coworkers [86, 85], but features a few differences. First of all, it is used in deep conjunction with the multi-scale approach typical of homogenization. In addition, a general and compact formulation is introduced to extend the approach to nearly all kinds of unit cell configurations.

Single-cell and multi-cell homogenization requires structural periodicity and therefore fails to account for geometric and/or material discontinuities. The bridging scale method can be used to address this issue, since it allows in fact to obtain a global coarse-scale FE solution of the homogenized equations of motion over the entire domain, while conducting a full fine-scale FE analysis of the periodic domain within the particular subregion where the discontinuity is located.

1.6 Organization of the Work

The present dissertation is organized according to the outline presented in the previous paragraph. In Chapter II the Fourier-based homogenization technique is introduced on the basis of some of the existing published work. First the Fourier analysis of periodic media is discussed. The concept of multiple scale analysis is then introduced and detailed. Chapter II also includes a few examples of applications of the homogenization method to simple periodic domains.

Chapter III introduces an alternative homogenization method based on the application of Taylor series expansion in the spatial domain. Chapter III also explores the topic of identification of equivalent mechanical properties. In particular, hexagonal and re-entrant (auxetic) lattices are examined, for which the homogenization method is used to construct equivalent differential equations involving classical elasticity operators. Among the quantities predicted are equivalent elasticity constants (Young's modulus, Poisson's ratio and shear modulus) along with wave velocities for the low-frequency propagation modes.

Chapter IV presents the concept of multi-cell analysis. The theoretical background and practical motivations behind this extension of the single-cell approach are first explained. A general compact formulation for the technique is then suggested to fit different unit cell configurations and make the multi-cell analysis straightforward and easy to code. The chapter is concluded by examples of two-cell and four-cell investigations of one-dimensional lattices, with special attention to dispersion relations and frequency response functions.

The bridging multi-scale method is discussed in Chapter V. The topic of wave propagation in solid media is recalled from Chapter II and III and the issue of modelling discontinuities within a regular assembly is discussed. The method is successfully applied to two test structures with localized defects. The limits of applicability are also considered and the issue of increasing the speed of the method is addressed by introducing a control on the integration scheme based on the total energy of the system.

A summary of the results obtained and possible directions for future research are presented in Chapter VI.

CHAPTER II

FOURIER-BASED HOMOGENIZATION OF PERIODIC MEDIA

2.1 Introduction

This chapter is devoted to the formulation and application of a homogenization method for periodic lattice structures. The aim of this technique is to obtain a continuum representation of the elastodynamic behavior of a given periodic domain, while preserving information about the geometric and material properties of its individual components. More specifically, the objective of homogenization is to obtain a set of continuum partial differential equations, whose solution approximates the behavior of the original structure. The advantage of a continuum representation of a discrete elastic problem is twofold. First, it may provide additional insight into the elastic and inertial properties of the structure, thus highlighting some features of its global behavior. Secondly, it provides a faster and more efficient way to calculate the dynamic response of the structure of interest. Conducting a full FE analysis of periodic structures, such as lattices, can in fact be extremely costly from a computational standpoint, since a detailed discretization of the domain needs in general a very high number of elements to properly represent the periodic pattern. A numerical solution of the homogenized equations of motion, on the other hand, can be obtained through a finite element (FE) analysis employing a coarse discretization using equivalent macro finite elements.

As stated in Chapter I, homogenization has been successfully applied to the analysis of static structural problems for the last thirty years. Equivalent homogeneous parameters have been derived to solve problems of static elasticity for many periodic assemblies of engineering interest. However, so far, not as much has been done for dynamic problems, such as vibrational problems and wave motion analysis.

The multi-scale method for lattice structures presented in [54, 53, 55], in which the spatial periodicity of lattices is exploited to write their static equilibrium equations in the

Fourier domain, is here embraced and extended to describe the harmonic behavior of one-dimensional (1D) and two-dimensional (2D) assemblies.

2.2 Fourier Analysis for Discrete Periodic Media

We consider elastic domains composed of elementary cells (see fig. 11) which define a periodic pattern. The displacement field of the domain can be described in terms of the degrees of freedom at the nodal locations within each cell. For a generic cell at location $\mathbf{m}$, $\mathbf{u}(\mathbf{m})$ denotes the vector of the cell's degrees of freedom, while $\mathbf{f}(\mathbf{m})$ contains the corresponding generalized forces. In here and in the following, bold letters denote vectors, while matrices are indicated as bold capital letters.

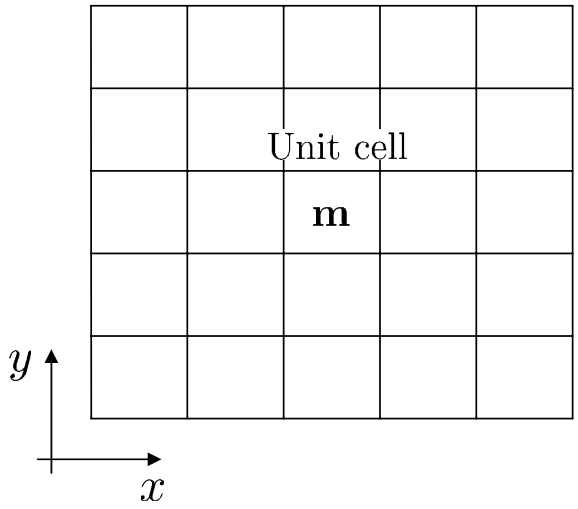

Figure 11: Schematic of a generic, two-dimensional periodic domain

The discretized equations of equilibrium for cell $\mathbf{m}$ can be expressed in the general following form:

$$\mathcal{D}[\mathbf{u}(\mathbf{m})] = \mathbf{f}(\mathbf{m}) \tag{1}$$

In eq. (1), $\mathcal{D}$ is a dynamic stiffness operator which can be expressed as:

$$\mathcal{D}[\mathbf{u}(\mathbf{m})] = \sum_{\mathbf{n}} \boldsymbol{D}_n \mathbf{u}(\mathbf{m} - \mathbf{n}) \tag{2}$$

with $\boldsymbol{D}_n$ being a constant coefficient matrix and $\mathbf{n}$ a parameter which identifies the cells of the domain interacting with the cell in $\mathbf{m}$. Hence $\mathbf{n} \in \mathbb{I}^d$, where $\mathbb{I}^d$ is a subset of $\mathbb{Z}^d$.

The discrete Fourier Transform can be defined as:

$$\hat{\mathbf{u}}(\boldsymbol{\xi}) = \sum_{\mathbf{m}\in\mathbb{Z}^d} \mathbf{u}(\mathbf{m})\, e^{i\mathbf{m}\cdot\boldsymbol{\xi}} \tag{3}$$

where:

$$\boldsymbol{\xi} \in (-\pi, \pi)^d$$

Likewise, a discrete Fourier Transform can be introduced for the force array in eq. (1) as:

$$\hat{\mathbf{f}}(\boldsymbol{\xi}) = \sum_{\mathbf{m}\in\mathbb{Z}^d} \mathbf{f}(\mathbf{m})\, e^{i\mathbf{m}\cdot\boldsymbol{\xi}} \tag{4}$$

Performing the transformations of eq. (3) and eq. (4) on eq. (1) yields:

$$\boldsymbol{\Gamma}(\boldsymbol{\xi})\hat{\mathbf{u}}(\boldsymbol{\xi}) = \hat{\mathbf{f}}(\boldsymbol{\xi}) \tag{5}$$

where the $\boldsymbol{\Gamma}(\boldsymbol{\xi})$ is called the symbol of $\mathcal{D}$ and it is given, in compact form, by:

$$\boldsymbol{\Gamma}(\boldsymbol{\xi}) = \sum_{\mathbf{n}} e^{i\mathbf{n}\cdot\boldsymbol{\xi}} \boldsymbol{D}_n \tag{6}$$

where the spatial periodicity of $\mathbf{u}$ has been employed. Details about the derivation of eq. (6) for a two-dimensional domain like the one of fig. 11 are given in the work by Karpov et al. [42] for static problems and are extended to dynamics in Appendix A. Solving the linear system of eq. (5) and evaluating the inverse Fourier Transform gives the solution in terms of the cell nodal degrees of freedom, which is expressed as:

$$\mathbf{u}(\mathbf{m}) = \frac{1}{(2\pi)^d} \int_{(-\pi,\pi)^d} \boldsymbol{\Gamma}(\boldsymbol{\xi})^{-1} \hat{\mathbf{f}}(\boldsymbol{\xi}) e^{-i\mathbf{n}\cdot\boldsymbol{\xi}} d\boldsymbol{\xi} \tag{7}$$

The described methodology allows a convenient description of the harmonic behavior of periodic media. The symbol representation provides the tool for estimating the asymptotic behavior of the system as $\boldsymbol{\xi} \to \mathbf{0}$. This condition in Fourier space corresponds to modes of deformation in the physical space which are long compared to the cell size. The asymptotic value of the symbol can also be utilized to formulate equivalent continuum equations whose solution describes the system's response as the cell characteristic dimensions tend to 0. The symbol formulation of the corresponding dynamic equilibrium equations are tools required to carry out the homogenization of the periodic domain and to perform a multi-scale analysis.

2.3 Evaluation of the Symbol For Discretized Periodic Domains

2.3.1 One-dimensional example

A simple illustrative case is the periodic system composed of an infinite sequence of identical springs and masses. The considered configuration is shown in fig. 12, where the unit cell is also highlighted. The dynamic stiffness formulation for the mass belonging to the i^{th} cell can be written as:

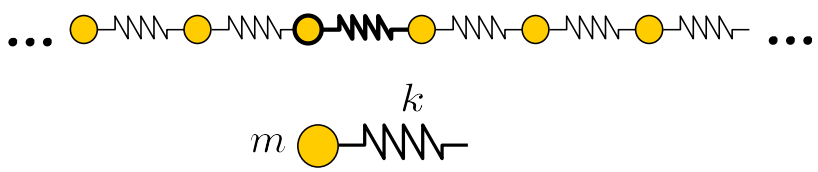

Figure 12: Periodic spring mass system

$$\left[2k - \omega^2 m\right] u(i) - k\left[u(i+1) + u(i-1)\right] = 0 \tag{8}$$

where it is assumed for simplicity that no loads are applied to the masses. According to eq. (6), the symbol for this one-dimensional (1D) periodic domain is given by:

$$\Gamma(\xi) = \sum_{n=-1}^{n=+1} e^{in\xi} D_n \tag{9}$$

which gives:

$$\Gamma(\xi) = 2k - \omega^2 m - k(e^{-i\xi} + e^{i\xi}) = 2k(1 - \cos\xi) - \omega^2 m \tag{10}$$

2.3.2 General formulation for a 1D periodic domain

The procedure shown for the spring-mass system can be generalized for a generic 1D periodic assembly. According to the configuration depicted in fig. 13, the behavior of the unit cell i is described by the following set of degrees of freedom

$$\mathbf{q} = \{\mathbf{q}_L,\ \mathbf{q}_R\}^T \tag{11}$$

where $\mathbf{q}_L = \mathbf{q}^{(i)}$ and $\mathbf{q}_R = \mathbf{q}^{(i+1)}$, with the subscripts L and R denoting left and right nodes of the i-th cell. It is assumed that the unit cell's behavior is described only in terms of the degrees of freedom of the boundary nodes. This assumption implies that complex

unit cell structures may be analyzed through the application of traditional condensation techniques which treat the internal degrees of freedom as "slaves" [13]. Alternatively, more sophisticated sub-structuring techniques, or wave-based methods such as the one presented in [11] may be applied to obtain a description of the cell's behavior in terms of generalized displacements of its boundaries. Suitable analytical or numerical discretization can be used

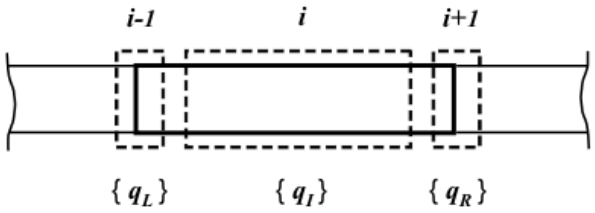

Figure 13: Schematic of unit cell and boundary degrees of freedom and generalized forces.

to describe the harmonic behavior of the unit cell, and its interaction with the subsequent cell $i+1$, in terms of mass and stiffness matrices, according to the well-known relation:

$$(\mathbf{K} - \omega^2 \mathbf{M}) \;\; \mathbf{q} = \mathbf{f} \tag{12}$$

where $\mathbf{f}$ is the vector of the generalized loads:

$$\mathbf{f} = \{\mathbf{f}_L, \;\; \mathbf{f}_R\}^T \tag{13}$$

with $\mathbf{f}_L = \mathbf{f}^{(i)}$ and $\mathbf{f}_R = \mathbf{f}^{(i+1)}$. The following periodic conditions are then applied to the boundary degrees of freedom:

$$\mathbf{q}_R = e^{-i\xi} \mathbf{q}_L \tag{14}$$

so that the following relation can be imposed:

$$\left\{ \begin{array}{c} \mathbf{q}_L \\ \mathbf{q}_R \end{array} \right\} = \mathbf{W} \mathbf{q}_r \tag{15}$$

where $\boldsymbol{q}_r = \boldsymbol{q}_L$, and

$$\mathbf{W} = \left[\begin{array}{c} \mathbf{I}_n \\ e^{-i\xi} \mathbf{I}_n \end{array} \right] \tag{16}$$

In eq. (16) $\mathbf{I}_n$ is a $n \times n$ identity matrix, where n is the number of degrees of freedom at each node. Imposing equilibrium and periodicity relations to the boundary forces, i.e. letting $\mathbf{f}_R = -e^{i\xi}\mathbf{f}_L$, and pre-multiplying the resulting equation by $\mathbf{W}^H$, with $()^H$ denoting the hermitian operator, yields the following reduced equation for the cell:

$$[\mathbf{K}_r(\xi) - \omega^2 \mathbf{M}_r(\xi)] \ \mathbf{q}_r = \mathbf{0} \tag{17}$$

where the reduced stiffness and mass matrices are given by

$$\begin{aligned} \mathbf{K}_r &= \mathbf{W}^H \mathbf{K} \mathbf{W} \\ \mathbf{M}_r &= \mathbf{W}^H \mathbf{M} \mathbf{W} \end{aligned} \tag{18}$$

Explicit expressions for $\mathbf{K}_r, \mathbf{M}_r$ can be obtained by considering partitions of the original matrices $\mathbf{K}, \mathbf{M}$ corresponding to the boundary degrees of freedom, i.e.:

$$\mathbf{K} = \begin{bmatrix} \mathbf{K}_{LL} & \mathbf{K}_{LR} \\ \mathbf{K}_{RL} & \mathbf{K}_{RR} \end{bmatrix}, \quad \mathbf{M} = \begin{bmatrix} \mathbf{M}_{LL} & \mathbf{M}_{LR} \\ \mathbf{M}_{RL} & \mathbf{M}_{RR} \end{bmatrix} \tag{19}$$

Performing the reduction suggested in eq. (18) and keeping track of the decomposition of $\mathbf{K}$ and $\mathbf{M}$ highlighted in eq. (19) yields the following expressions for the reduced stiffness and mass matrices $\mathbf{K}_r$ and $\mathbf{M}_r$:

$$\mathbf{K}_r = \mathbf{K}_{LL} + e^{i\xi}\ \mathbf{K}_{LR} + e^{-i\xi}\ \mathbf{K}_{RL} + \mathbf{K}_{RR} \tag{20}$$

$$\mathbf{M}_r = \mathbf{M}_{LL} + e^{i\xi}\ \mathbf{M}_{LR} + e^{-i\xi}\ \mathbf{M}_{RL} + \mathbf{M}_{RR} \tag{21}$$

From $\mathbf{K}_r$ and $\mathbf{M}_r$, the symbol for the considered domain can be obtained as:

$$\mathbf{\Gamma}_r(\xi) = [\mathbf{K}_r\,(\xi) - \omega^2 \mathbf{M}_r\,(\xi)] \tag{22}$$

2.3.3 Formulation for a 2D periodic domain

The technique can be easily extended to two-dimensional (2D) and three-dimensional (3D) domains. For simplicity, however, reference is made to the 2D lattice shown in fig. 14. The behavior of the elementary cell also highlighted in fig. 14 is described by a set of degrees of freedom which are related to those of neighboring cells through a classical dynamic stiffness formulation:

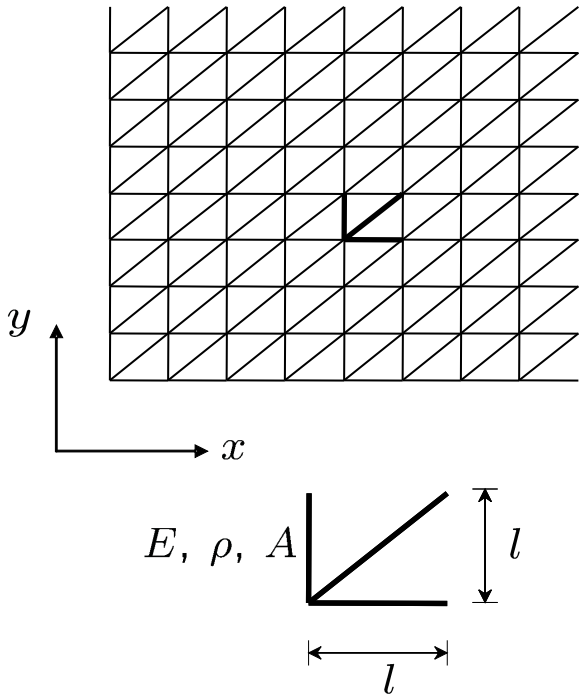

Figure 14: Two-dimensional truss lattice

$$\Big(\mathbf{K} - \omega^2 \mathbf{M}\Big)\mathbf{u} = \mathbf{0} \tag{23}$$

where $\mathbf{K}$ and $\mathbf{M}$ are the mass and stiffness matrices of the cell, and $\mathbf{u}$ is a vector containing the generalized nodal displacements of the cell and its neighbors. The evaluation of the symbol for the lattice can be conveniently obtained through the following matrix operation:

$$\mathbf{\Gamma}(\boldsymbol{\xi}) = \mathbf{A}^H(\xi_1, \xi_2)\Big[\mathbf{K} - \omega^2 \mathbf{M}\Big]\mathbf{A}(\xi_1, \xi_2) \tag{24}$$

where matrix $\mathbf{A}$ is defined, for the lattice of fig. 14, as:

$$\mathbf{A} = \begin{bmatrix} \mathbf{I} & e^{-i\xi_1}\mathbf{I} & e^{-i\xi_2}\mathbf{I} & e^{-i(\xi_1+\xi_2)}\mathbf{I} \end{bmatrix} \tag{25}$$

where $\mathbf{I}$ is a 2*2 identity matrix. Also in eq. (24), $\boldsymbol{\xi} = [\ \xi_1 \quad \xi_2\ ]$ is the vector of the Fourier Transform variables describing the dynamic equilibrium equations for the 2D lattice with $\xi_k \in [-\pi, \pi]$, $(k = 1, 2)$.

2.4 Multi-scale Formulation

2.4.1 Scaling of the physical quantities

The introduction of the symbol representation gives the opportunity to define a multi-scale formulation and equivalent continuum equations whose solution approximate the lattice dynamic equilibrium conditions to an arbitrary order of accuracy. The underlying assumption is that the wavelength of the dynamic response of the lattice is much higher than the characteristic dimensions of the unit cell. Different length scales result from the description of the global deformation of the entire periodic assembly, and the detailed description of the unit cell. A small parameter ϵ is introduced to relate these different length scales:

$$\epsilon = \frac{l}{L} \tag{26}$$

where L is the characteristic dimension of the periodic assembly, while l is the characteristic

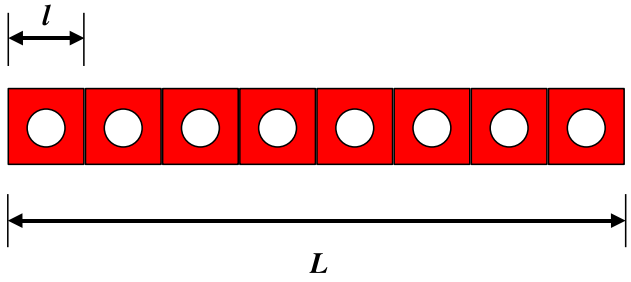

Figure 15: Macro and micro-scale characteristic lengths

dimension of the unit cell (see fig. 15). Within this framework, the cell's degrees of freedom are denoted as $\mathbf{u}^{(\epsilon)}(\mathbf{m})$, and the corresponding dynamic stiffness operator defined in eq. (1) becomes $\mathcal{D}^{(\epsilon)}$. The lattice matrix equation can be expressed in the physical space as:

$$\mathcal{D}^{(\epsilon)}[\mathbf{u}^{(\epsilon)}(\mathbf{m})] = \mathbf{f}^{(\epsilon)}(\mathbf{m}) \tag{27}$$

or in the Fourier space as

$$\mathbf{\Gamma}^{(\epsilon)}(\boldsymbol{\xi})\hat{\mathbf{u}}^{(\epsilon)}(\boldsymbol{\xi}) = \hat{\mathbf{f}}^{(\epsilon)}(\boldsymbol{\xi}) \tag{28}$$

In [54] it is shown that the symbol of lattice operator $\mathbf{\Gamma}^{(\epsilon)}$ for truss structures is related to the unscaled operator as follows:

$$\mathbf{\Gamma}^{(\epsilon)}(\boldsymbol{\xi}) = \epsilon^2\mathbf{\Gamma}(\epsilon\boldsymbol{\xi}) \tag{29}$$

This can be verified by actually individually scaling all the quantities in the equations of motion that are direct or indirect functions of lengths: such quantities include lengths, areas and volumes, as well as mass and stiffness terms and body or area forces.

2.4.2 Derivation of continuum equations

The objective is to approximate eq. (27) through a system of partial differential equations, denoted as homogenized equations, which can be expressed as follows:

$$\mathcal{A}^{(\epsilon,p)}\boldsymbol{u}^{(\epsilon,p)} = \boldsymbol{f} \tag{30}$$

where $\mathcal{A}^{(\epsilon,p)}$ is a constant coefficient quasi-differential operator such that the solution of eq. (30) $\mathbf{u}^{(\epsilon,p)}$ satisfies:

$$\mathbf{u}^{(\epsilon)}(\mathbf{m}) = \boldsymbol{u}^{(\epsilon,p)} + \mathrm{O}(\epsilon^{2p+2}) \tag{31}$$

provided that $\boldsymbol{f}$ is regular enough (the regularity requirements increase rapidly with increasing order p). In eq. (30) a distinction has been made between nodal arrays denoted with bold letters and continuum field vectors denoted in *italics*: this distinction is maintained throughout the thesis. The continuum equations described above through a general notation can be obtained by means of the Fourier Transform solution method. In the Fourier domain, the solution of the transformed dynamic equilibrium equations for the scaled lattice is given by:

$$\hat{\mathbf{u}}^{(\epsilon)}(\boldsymbol{\xi}) = \left[\boldsymbol{\Gamma}^{(\epsilon)}(\boldsymbol{\xi})\right]^{-1}\hat{\mathbf{f}}^{(\epsilon)}(\boldsymbol{\xi}) \tag{32}$$

Denoting with $\boldsymbol{S}^{(\epsilon,p)}(\boldsymbol{\xi})$ the first $2p+2$ terms of the Taylor series expansion of $\left[\boldsymbol{\Gamma}^{(\epsilon)}(\boldsymbol{\xi})\right]^{-1}$, i.e.:

$$\left[\boldsymbol{\Gamma}^{(\epsilon)}(\boldsymbol{\xi})\right]^{-1} = \boldsymbol{S}^{(\epsilon,p)}(\boldsymbol{\xi}) + \mathrm{O}(\epsilon^{2p+2}) \tag{33}$$

yields the following expression for the approximate solution in the Fourier domain:

$$\hat{\boldsymbol{u}}^{(\epsilon)}(\boldsymbol{\xi}) = \boldsymbol{S}^{(\epsilon,p)}(\boldsymbol{\xi})\hat{\mathbf{f}}^{(\epsilon)}(\boldsymbol{\xi}) + \mathrm{O}(\epsilon^{2p+2}) \tag{34}$$

The continuous variable approximating the solution of eq. (27) can be expressed as [55]:

$$\boldsymbol{u}^{(\epsilon,p)} = \mathcal{F}^{-1}\left[\boldsymbol{S}^{(\epsilon,p)}\hat{\mathbf{f}}^{(\epsilon)}\right] \tag{35}$$

This solution can be alternatively obtained through the inverse transform of the approximated version of the symbol, which yields a differential equation in physical space describing the behavior of the lattice within a defined level of approximation. In the following section, a distinction is made between "mono-atomic" and "multi-atomic" lattices. Mono-atomic lattices are composed of unit cells whose behavior can be reduced to that of a single representative node with a single degree of freedom, while multi-atomic include all other cases where multiple nodes, or a single node with multiple degrees of freedom describe the behavior of the unit cell [54]. This distinction is introduced since the homogenization technique can be fairly simply addressed for mono-atomic lattices, while the general case of multi-atomic lattices is more involved and it is here introduced as an extension of the simpler case. The symbol for mono-atomic lattices is a scalar quantity, while it is a square matrix in the general case of multi-atomic lattices.

2.4.3 Mono-atomic lattices

It has been shown [54] that the unscaled symbol $\Gamma(\boldsymbol{\xi})$ for a generic mono-atomic lattice reduces to a trigonometric function and, as such, has an absolutely convergent power series. Therefore it can be expressed as follows:

$$\Gamma(\boldsymbol{\xi}) = \boldsymbol{\xi}^T \, \boldsymbol{\Psi} \, \boldsymbol{\xi} + \sum_{j=2}^{\infty} b_j(\boldsymbol{\xi}) \tag{36}$$

where $\boldsymbol{\Psi}$ is a positive definite matrix and b_j's are homogeneous polynomials of order $2j$. Using eq. (36), it can be shown that there exist polynomials a_{2j} such that the inverse of the symbol can be expressed as:

$$\Gamma^{-1}(\boldsymbol{\xi}) = \frac{1}{\boldsymbol{\xi}^T \, \boldsymbol{\Psi} \, \boldsymbol{\xi}} + \sum_{j=1}^{p} \frac{a_{2j}(\boldsymbol{\xi})}{(\boldsymbol{\xi}^T \, \boldsymbol{\Psi} \, \boldsymbol{\xi})^{j+1}} + \mathcal{R}_p(\boldsymbol{\xi}) \tag{37}$$

The scaled version of the symbol can be easily obtained by considering eq.s (29) and (37), to obtain:

$$\Gamma^{(\epsilon)^{-1}}(\boldsymbol{\xi}) = \frac{1}{\boldsymbol{\xi}^T \, \boldsymbol{\Psi} \, \boldsymbol{\xi}} + \sum_{j=1}^{p} \epsilon^{2j} \frac{a_{2j}(\boldsymbol{\xi})}{(\boldsymbol{\xi}^T \, \boldsymbol{\Psi} \, \boldsymbol{\xi})^{j+1}} + \mathcal{R}_p^{(\epsilon)}(\boldsymbol{\xi}) \tag{38}$$

so that the Taylor series expansion to order p for the inverse of the symbol can be expressed as:

$$S^{(\epsilon,2p)}(\boldsymbol{\xi}) = \frac{1}{\boldsymbol{\xi}^T \, \boldsymbol{\Psi} \, \boldsymbol{\xi}} + \sum_{j=1}^{p} \epsilon^{2j} \frac{a_{2j}(\boldsymbol{\xi})}{(\boldsymbol{\xi}^T \, \boldsymbol{\Psi} \, \boldsymbol{\xi})^{j+1}} \tag{39}$$

Evaluating the inverse Fourier Transform of eq. (39), yields an equivalent continuous differential equation with $\mathbf{u}^{(\epsilon,p)}$ as unknown. The general formulation for the inverse Fourier Transform, with the approximated symbol expression given in eq. (39) is given by:

$$\big(-\nabla\ \boldsymbol{\Psi}\nabla\big)^{p+1}\boldsymbol{u}^{(\epsilon,p)} = \big(-\nabla\ \boldsymbol{\Psi}\nabla\big)^{p}\boldsymbol{f} + \sum_{j=1}^{p}\epsilon^{2j}\big(-\nabla\boldsymbol{\Psi}\ \nabla\big)^{p-j}a_{2j}(\partial)\boldsymbol{f} \tag{40}$$

where $\nabla = [\ \frac{\partial}{\partial x}\quad \frac{\partial}{\partial y}\ ]^T$. Eq. (40) shows how increasing the order of approximation corresponds to higher order of differentiation of the continuous variable. This introduces the difficulty of identifying the appropriate set of boundary conditions, which allow the solution of associated boundary value problems. In addition, the applied loads need to satisfy increasing regularity requirements, which require them to be very smooth if high order approximations are to be considered. The issue of defining the appropriate set of boundary conditions in multi-scale formulations for periodic domains has been identified as a problem by other authors (see for example [21, 20]), and requires the development of solutions on a case-by-case basis. The identification of proper boundary conditions is probably the main obstacle in the development of a homogenized formulation and often dictates where to truncate the Taylor series and the order of the approximation itself. The continuous formulation truncated to the first order, i.e. by setting $p = 0$ in eq. (39), gives:

$$\big(-\nabla\ \boldsymbol{\Psi}\nabla\big)\boldsymbol{u}^{(\epsilon,0)} = \boldsymbol{f} \tag{41}$$

where the continuous displacement variable $\boldsymbol{u}^{(\epsilon,0)}$ does not depend on the small scale parameter ϵ and no differentiation of the force terms is needed.

In the remainder of this work, the presented methodology will be applied to obtain approximations of the dispersion relations of the considered periodic domains. It will be shown how the continuum representation approximates the discrete lattice in a limited frequency range centered at the point where the Taylor series expansion is performed, typically around zero. The solution of the continuum equations for an assigned set of boundary conditions and loads is then presented. The issues of boundary conditions and load regularity will be at this time avoided by considering limited homogenization orders and applied point loads which can be accounted for as boundary conditions.

2.4.4 Multi-atomic lattices

The previous methodology can be extended to apply to the general case of multi-atomic lattices. The cell of a generic multi-atomic lattice contains k nodes and s degrees of freedom. The unscaled symbol $\mathbf{\Gamma}$, which can be obtained through the general procedure described in Section 2.3.3, is a uniformly bounded, Hermitian, semi-definite positive matrix made of trigonometric polynomials. Its inverse can be expressed as:

$$\left[\mathbf{\Gamma}(\boldsymbol{\xi})\right]^{-1} = \frac{1}{\det[\mathbf{\Gamma}(\boldsymbol{\xi})]}\,\mathbf{L}(\boldsymbol{\xi}) \tag{42}$$

where $\mathbf{L}(\boldsymbol{\xi})$ is the matrix of the co-determinants of $\mathbf{\Gamma}$, and where it may be shown [54] that:

$$\det[\mathbf{\Gamma}](\boldsymbol{\xi})] = \boldsymbol{\xi}^T\ \mathbf{\Psi}\ \boldsymbol{\xi} + \sum_{j=2}^{\infty} c_j(\boldsymbol{\xi}) \tag{43}$$

In eq. (43), $c_j(\boldsymbol{\xi})$'s denote higher order polynomials, such that:

$$\det[\mathbf{\Gamma}(\boldsymbol{\xi})] = \boldsymbol{\xi}^T\ \mathbf{\Psi}\ \boldsymbol{\xi} + \mathrm{O}(|\boldsymbol{\xi}|^4)$$

All co-determinants of $\mathbf{\Gamma}$ are trigonometric polynomials, and thus there exist multinomials p_{nm} such the the n, m entry of $\mathbf{L}(\boldsymbol{\xi})$ can be expressed as:

$$\boldsymbol{L}_{nm}(\boldsymbol{\xi}) = p_{nm}(e^{i\boldsymbol{\xi}}) \tag{44}$$

Equations (43) and (44) provide the tools for the evaluation of the series expansion of $\left[\mathbf{\Gamma}(\boldsymbol{\xi})\right]^{-1}$. Considering in addition the scaling relation for the symbol (eq. (29)), gives the following series expansion for the scaled symbol $\left[\mathbf{\Gamma}^{(\varepsilon)}(\boldsymbol{\xi})\right]^{-1}$:

$$\left[\left[\mathbf{\Gamma}^{(\epsilon)}(\boldsymbol{\xi})\right]^{-1}\right]_{nm} = \frac{p_{nm}(e^{i\epsilon\boldsymbol{\xi}})}{\boldsymbol{\xi}^T\ \mathbf{\Psi}\ \boldsymbol{\xi}} + \sum_{j=1}^{p} \epsilon^{2j}\frac{p_{nm}(e^{i\epsilon\boldsymbol{\xi}})a_{2j}(\boldsymbol{\xi})}{(\boldsymbol{\xi}^T\ \mathbf{\Psi}\ \boldsymbol{\xi})^{j+1}} + \epsilon^2\mathrm{O}((\epsilon|\boldsymbol{\xi}|)^{2p}) \tag{45}$$

The expansion in eq. (45) can be used to obtain an approximate continuous description of the multi-atomic lattice's behavior. Within an accuracy of order p, the solution is described by the continuous displacement function $\mathbf{u}^{(\epsilon,p)}$ introduced in eq. (31), which is given by:

$$\boldsymbol{u}^{(\epsilon,p)} = \mathcal{F}^{-1}\left[\boldsymbol{S}^{(\epsilon,p)}\hat{\mathbf{f}}^{(\epsilon)}\right] \tag{46}$$

where $\boldsymbol{S}^{(\epsilon,p)}$ is the expansion of the inverse symbol truncated to the p-th term. Examples of the results obtained from the procedure outlined above can be easily illustrated when

the series is truncated to the first term. In this case, the co-determinants take the following form:

$$p_{nm}(e^{i\boldsymbol{\xi}}) = c_0 + \mathbf{v}^{(nm)} \cdot (i\boldsymbol{\xi}) + \mathrm{O}(|\boldsymbol{\xi}|^2) \tag{47}$$

where c_0 is a constant independent of n, m, and where $\mathbf{v}^{(nm)} \in \mathbb{R}^d$ is a vector. Accordingly, eq. (45) becomes:

$$\left[\left[\boldsymbol{\Gamma}^{(\epsilon)}(\boldsymbol{\xi})\right]^{-1}\right]_{nm} = \left[\boldsymbol{S}^{(\epsilon,0)}(\boldsymbol{\xi})\right]_{nm} + \epsilon^2 \mathrm{O}(\epsilon|\boldsymbol{\xi}|^0) \ , \ (\epsilon|\boldsymbol{\xi}| \to 0) \tag{48}$$

where

$$\left[\boldsymbol{S}^{(\epsilon,0)}(\boldsymbol{\xi})\right]_{nm} = \frac{c_0 + \epsilon \mathbf{v}^{(nm)} \ (i\boldsymbol{\xi})}{\boldsymbol{\xi}^T \ \boldsymbol{\Psi} \ \boldsymbol{\xi}}$$

The corresponding homogenized equation for the n-th degree of freedom of the cell then reads:

$$-\nabla \ \boldsymbol{\Psi} \ \nabla u_n^{(\epsilon,0)} = c_0 f_n + \epsilon \sum_{m=1}^{k+s} \mathbf{v}^{(nm)} \ \nabla f_m \tag{49}$$

where $u_n^{(\epsilon,0)}$ is the n-th component of $\boldsymbol{u}^{(\epsilon,0)}$. The resulting differential operator in eq. (49) is independent of the index n. Therefore, within the first order approximation, the behavior of all of the cell's degrees of freedom is governed by homogenized equations of the same kind. In addition, the differential operator refers to the inverse Fourier Transform of the term $\boldsymbol{\xi}^T \ \boldsymbol{\Psi} \ \boldsymbol{\xi}$, which corresponds to the determinant of the lattice symbol (eq. (43)). These two observations suggest that the homogenized equations can be thought of as obtained by considering some fictitious mono-atomic lattice whose symbol is $\det[\boldsymbol{\Gamma}(\boldsymbol{\xi})]$. The application of this concept can be useful for the reduction of multi-atomic lattices to simpler, equivalent mono-atomic lattices, which results in a convenient way to evaluate homogenized equations.

2.5 Application to One-dimensional Periodic Domains

2.5.1 Spring-mass system

Let us consider a chain of particles having constant mass m coupled with the nearest neighbors by linear elastic springs of unit length and stiffness constant k as shown in fig. 12. Let us label u_0 and u_1 the axial displacements of the two nodes defining the geometry of the unit cell. The equations of motion for the cell nodal displacements, under the assumption

of harmonic motion, are:

$$-\omega^2 \begin{bmatrix} m/2 & 0 \\ 0 & m/2 \end{bmatrix} \begin{pmatrix} u_0 \\ u_1 \end{pmatrix} + \begin{bmatrix} k & -k \\ -k & k \end{bmatrix} \begin{pmatrix} u_0 \\ u_1 \end{pmatrix} = \mathbf{0} \tag{50}$$

According to the procedure introduced above, the exact symbol is found to be:

$$\Gamma(\xi) = -m\omega^2 + [2k\,(1 - \cos\xi)] \tag{51}$$

Scaling the quantities in eq. (51), taking a Taylor series expansion of the cosine term with respect to the scaled wave number $\epsilon\xi$, and solving for the frequency ω, yields the expression:

$$\omega^2 = \frac{k}{m}\left[\xi^2 - \frac{\epsilon^2\xi^4}{12} + \frac{\epsilon^4\xi^6}{360} + O(\xi^8)\right] \tag{52}$$

The result in eq. (52) is the long wavelength approximation of the dispersion relation for the spring-mass system. The higher the order of the terms retained in the Taylor series expansion of eq. (52), the better the agreement between exact and approximate dispersion relations, as shown in fig. 16.

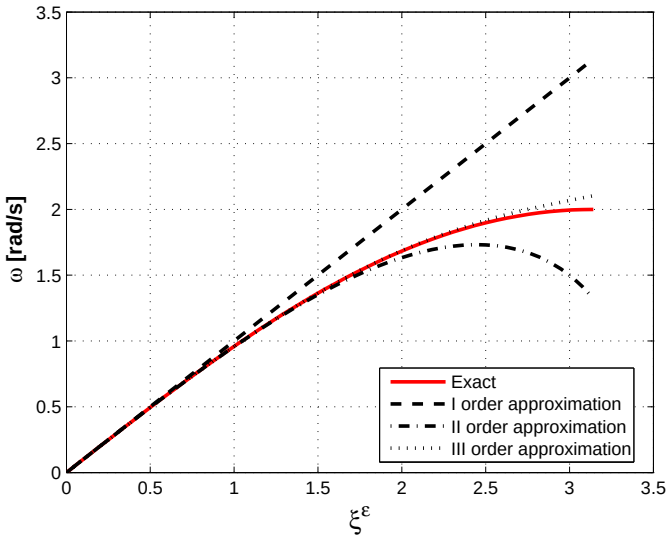

Figure 16: Spring-mass system: approximation of dispersion relation for increasing order p

2.5.2 Bi-material Rod

The one-dimensional bi-material rod of fig. 17.a is constituted of a sequence of elements with same cross sectional area and different lengths and material properties. A lumped

parameters representation of the model is given by the spring-mass system of fig. 17.b made of a sequence of cells containing two masses m_1 and m_2, connected by linear springs of constants k_1 and k_2. These parameters are defined as follows:

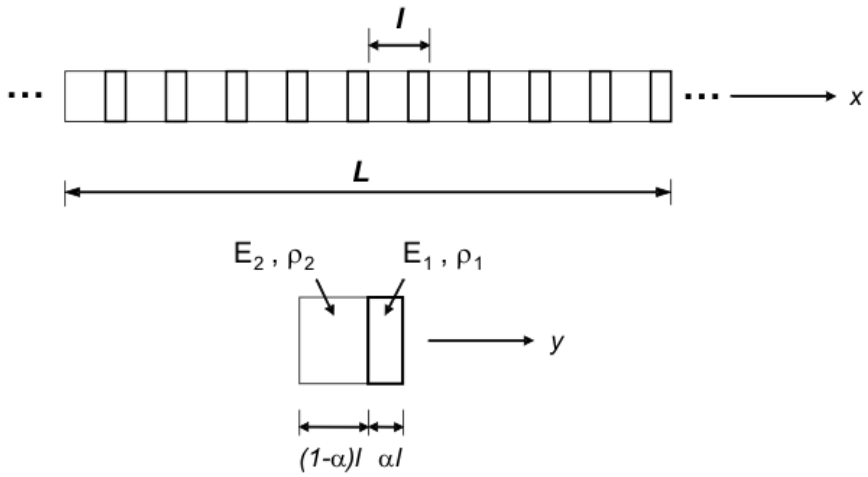

(a) Bi-material Rod

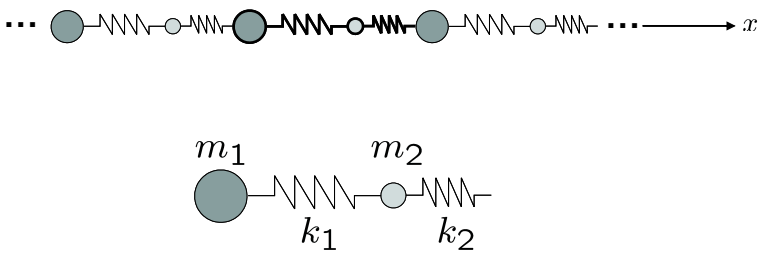

(b) Spring Mass System

Figure 17: One-dimensional periodic domain

$$k_1 = \frac{E_1 A}{\alpha}, \quad k_2 = \frac{E_2 A}{(1-\alpha)} \tag{53}$$

$$m_1 = \rho_1 A\alpha, \quad m_2 = \rho_2 A(1-\alpha) \tag{54}$$

where A denotes the rod's cross sectional area. The unscaled symbol for the system is a $2 * 2$ matrix given by:

$$\mathbf{\Gamma}(\xi, \omega) = \begin{bmatrix} k_1 + k_2 - m_1\omega^2 & -(k_1 e^{i\xi} + k_2) \\ -(k_1 e^{i\xi} + k_2) & k_1 + k_2 - m_2\omega^2 \end{bmatrix} \tag{55}$$

where the dependency of the symbol on frequency ω is now explicitly indicated. The dispersion relation for the domain is obtained by solving in terms of frequency ω the following

equation:

$$\det\left[\mathbf{\Gamma}(\xi,\omega)\right]=0 \tag{56}$$

for assigned values of $\xi \in (0,\pi)$. The scaled version of the symbol $\mathbf{\Gamma}^{(\epsilon)}(\xi,\omega)$ is obtained through eq. (29), while the corresponding homogenized equation is derived for $\epsilon\xi \to 0$ through a Taylor series expansion which gives:

$$\det\left[\mathbf{\Gamma}^{(\epsilon)}(\xi,\omega)\right]=b(\omega)+\sum_{j=0}^{p}a_j(\omega)\epsilon^{2j}\xi^{2(j+1)}+\mathrm{O}\left[(\epsilon\xi)^{2(p+2)}\right] \tag{57}$$

where p is the order of the approximation, and where a_j, b are frequency dependent coefficients. The corresponding continuous equation can be obtained through inverse Fourier transformation of eq. (57), which after truncation to order p gives:

$$\left[b(\omega)+\sum_{j=0}^{p}a_j(\omega)\epsilon^{2j}\frac{d^{2(j+1)}}{dx^{2(j+1)}}\right]u^{(\epsilon,p)}(x)=0 \tag{58}$$

where $u^{(\epsilon,p)}(x)$ is a continuous function approximating to order p the displacement of the homogenized periodic domain along the longitudinal direction x. The coefficients $a_j(\omega), b(\omega)$ define the properties of the continuum domain whose behavior approximates that of the considered periodic system up to the desired order. Insight in the considered process can be again obtained by truncating the expansion in eq. (57) at the first order ($p=1$). This gives:

$$a_0(\omega)\frac{d^2u^{(\epsilon,0)}(x)}{dx^2}+b(\omega)u^{(\epsilon,0)}(x)=0 \tag{59}$$

where, after neglecting higher powers of ω, b and a_0 are found to be:

$$\begin{aligned} b(\omega) &= \omega^2(m_1+m_2) \\ a_0(\omega) &= \frac{k_1k_2}{k_1+k_2} \end{aligned} \tag{60}$$

From the obtained continuum equation a homogenized density and a homogenized Young's modulus can be isolated such that:

$$\begin{aligned} \rho_H A &= (m_1+m_2) \\ E_H A &= \frac{k_1k_2}{k_1+k_2} \end{aligned} \tag{61}$$

This result corresponds with the one presented for the same example in various papers [16] which show how the homogenized properties of the bi-material rod are obtained by taking

the harmonic average of the material's Young's moduli and the weighted mean of their density, in accordance with the *rule of mixtures* [21].

2.5.3 Approximation of the dispersion relations

For an assigned frequency ω, eq. (58) is a homogeneous, ordinary differential equation with constant coefficients. Its solution can be easily obtained provided the appropriate set of boundary conditions is available. Regardless, a general solution can be expressed as:

$$u^{(\epsilon,p)}(x) = \sum_{j=1}^{2(p+1)} c_j^{(\epsilon)} e^{\kappa_j^{(\epsilon)} x} \tag{62}$$

where the coefficients $c_j^{(\epsilon)}$ are integration constants, while the exponents $\kappa_j^{(\epsilon)}$ are the roots of the characteristic equation:

$$\left[b(\omega) + \sum_{j=0}^{p} a_j(\omega) \epsilon^{2j} {\kappa^{(\epsilon)}}^{2(j+1)} \right] = 0 \tag{63}$$

and represent the wavenumbers describing, with an approximation to the order p, the wave propagation in the structure. Evaluating and plotting the wavenumbers $\kappa_j^{(\epsilon)}$ versus frequency ω defines an approximation for the dispersion relations up to the desired order. Examples of the obtained dispersion relations for increasing orders of truncation are shown in fig. 18. The plots are obtained for $k_1 = k_2 = 1\,N/m$, and $m_1 = 1\,kg$, $m_2 = 2\,kg$, and are compared to the exact dispersion relations obtained from eq. (56), solved upon imposing wavenumbers belonging to the first Brillouin zone [10] of the periodic domain ($\kappa^{(\epsilon)} l \in [0, \pi]$). The plots of fig. 18 show how the approximation improves by increasing the order of the series expansion.

2.5.4 One-dimensional trusses

An additional example evaluates equivalent continuum equations for the 1D trusses shown in fig. 19. It is assumed that the nodes of the trusses are constrained to move along the longitudinal direction. The displacements of the nodes of the cell are related through the cell's mass and stiffness matrices, formulated according to standard FE techniques.

The symbol is obtained and expanded in Taylor series according to the procedures described in Section 2. These operations yield an expression for the determinant of the symbol

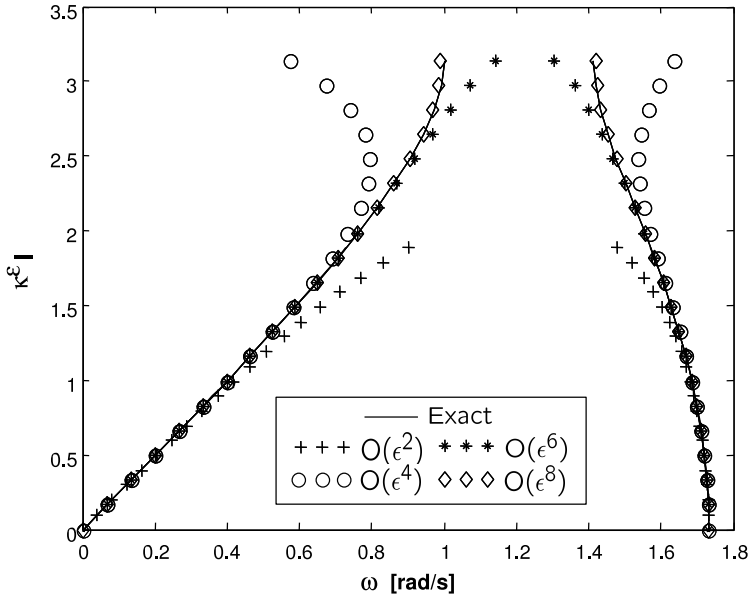

Figure 18: Spring-mass system: approximation of dispersion relation for increasing order p and comparison with exact solution

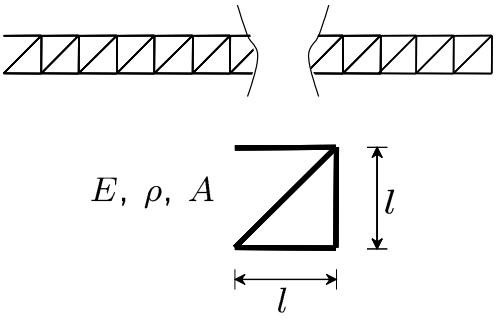

(a) Truss A

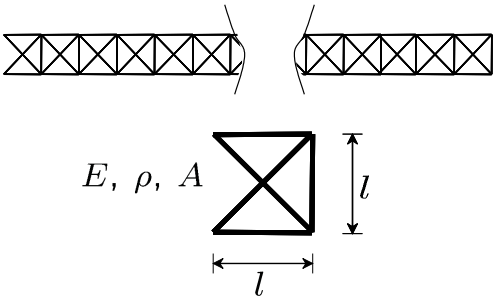

(b) Truss B

Figure 19: One-dimensional trusses

which is equivalent to the one given in eq. (57), with coefficients b, a_j depending upon the topology of the unit cell and defining the homogenized properties for the equivalent continuous structure. The approximated dispersion relations for the trusses are compared to the exact ones in fig. 20. The plots demonstrate the increasing accuracy of the considered homogenization technique and confirm the results shown for the case of the spring-mass system. The major difference with respect to the previous example is that higher orders of expansion are required in order to obtain a good approximation of the wavenumber/frequency relation over the first Brillouin zone. This has important implications on the evaluation of the harmonic response of periodic assemblies through the homogenized models. This issue will be discussed in the following section.

2.5.5 Harmonic Response of One-Dimensional Periodic Domains

The homogenization procedure described above can be applied to formulate a "super-element", which predicts the response of the periodic assembly, without the need for a detailed FE model. This process introduces an approximation which depends on the order of truncation in terms of ϵ. The solution of the resulting continuum equation is only possible if a sufficient number of boundary conditions can be formulated. This introduces limitations on the order of approximation that can be achieved, as refining the order of the series corresponds to increasing the order of the continuous equation.

In here we investigate spring-mass and truss systems that are constrained to displacements along a longitudinal coordinate. This allows imposing a maximum of two conditions on either the boundary displacements or on their spatial rate, so that the maximum order for the continuous equation is limited to $p = 0$. The behavior of both systems is described by equations of the kind of eq. (59). We assume that all the considered structures are fixed at one end and excited at the opposite end by a longitudinal harmonic force. A schematic of the considered configurations is shown in fig. 73, which also highlights the concept of an equivalent uniform rod approximating the considered periodic domains. A solution for eq. (59) can be easily found to be:

$$u^{(\epsilon,0)}(x) = c_1^{(\epsilon)} e^{\kappa_1^{(\epsilon)} x} + c_2^{(\epsilon)} e^{\kappa_2^{(\epsilon)} x} \tag{64}$$

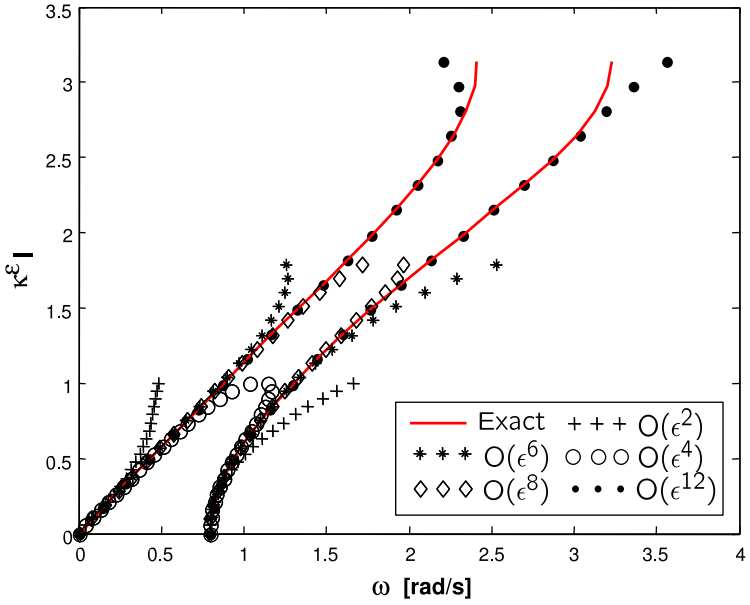

(a) Truss A

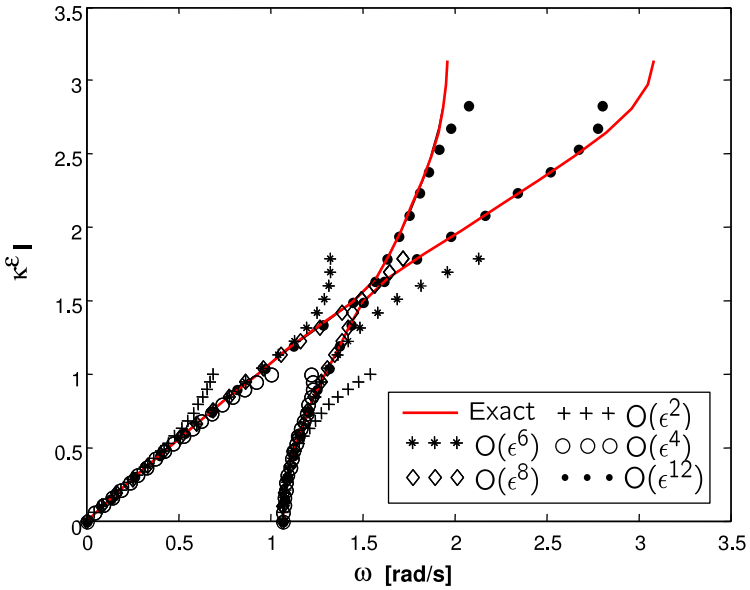

(b) Truss B

Figure 20: Dispersion relations for the one-dimensional trusses

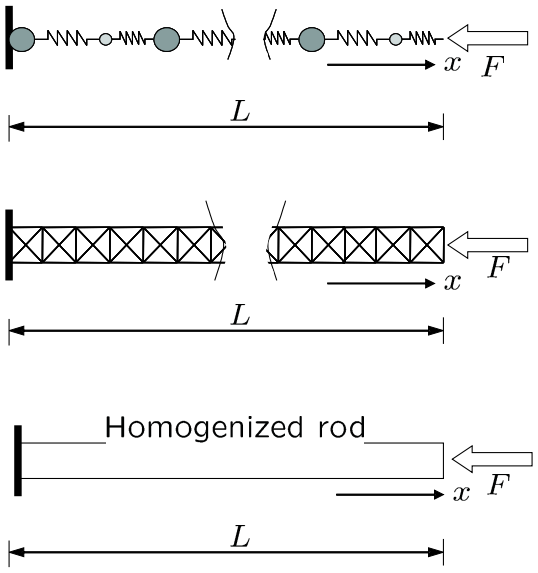

Figure 21: Considered 1D periodic structures and homogenized continuous rod

where $c_j^{(\epsilon)}, (j = 1, 2)$ are integration constants which are determined through the application of the following set of boundary conditions:

$$\begin{aligned} u^{(\epsilon,2)}(x = 0) &= 0 \\ a_0^{(\epsilon)} \tfrac{d}{dx} u^{(\epsilon,2)}(x)\Big|_{x=L} &= -F \end{aligned}$$

Also in eq. (64), the wavenumbers $\kappa_j^{(\epsilon)}, (j = 1, 2)$ are obtained from the solution of the characteristic equation associated with eq. (59). As previously discussed, the characteristic equation approximates the dispersion relation to the lowest order, and the corresponding truncation error increases with the excitation frequency ω. The validity of the approximation in the low frequency range and the increasing error at higher frequencies is demonstrated by evaluating the Frequency Response Function (FRF) for the equivalent uniform rod, computed by evaluating its end displacement for an harmonic force of varying frequency. These predictions are compared with the results obtained from the solution of a detailed model of the periodic assemblies. The results for a periodic sequence of 40 spring-mass cells with $k_1 = 2$ N/m, $k_2 = 1$ N/m, and $m_1 = m_2 = 1$ kg are shown in fig. 22. The comparisons for trusses A and B composed of 50 cells are displayed in fig.s 23.

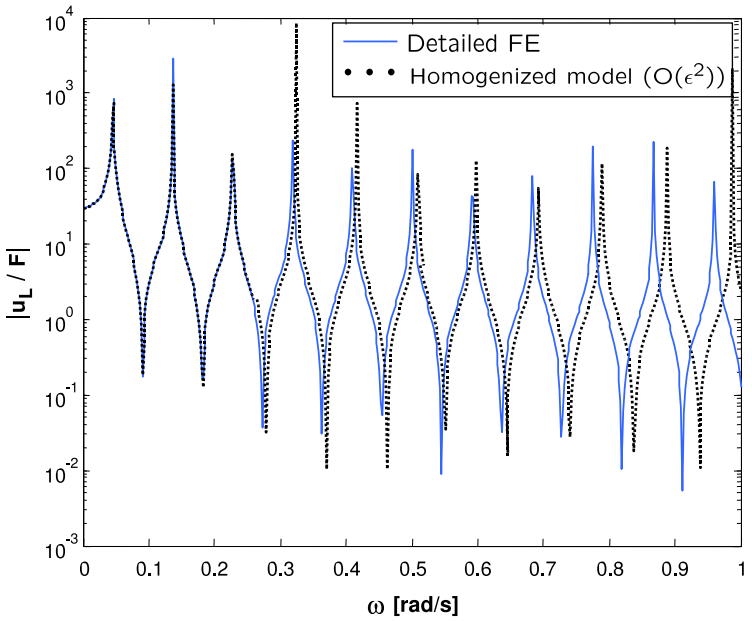

Figure 22: Frequency response function for the spring mass system: comparison between detailed and homogenized models

2.5.6 Solution based on the exact dispersion relation

The technique presented above can be used to approximate the response of the considered periodic system, and to identify its equivalent mechanical properties through the interpretation of the coefficients b, a_j. If no specific knowledge of the coefficients is required, a significant improvement in the accuracy of the response predictions can be achieved by considering wavenumbers $\kappa_j^{(\epsilon)}, (j = 1, 2)$ in eq. (64) obtained from the solution of the exact dispersion relation, which can be estimated through the transfer matrix of the unit cell. A generic 1D periodic system can be represented schematically as in fig. 24. The transfer matrix relates the generalized displacements and forces to the right of the cell to those to the left of it, as follows:

$$\begin{pmatrix} \mathbf{u}_R \\ \mathbf{F}_R \end{pmatrix} = \boldsymbol{T} \begin{pmatrix} \mathbf{u}_L \\ \mathbf{F}_L \end{pmatrix} \tag{65}$$

where $\mathbf{u}, \mathbf{F}$ respectively denote generalized displacements and forces, while subscripts R, L stand for 'right' and 'left'. The transfer matrix can be conveniently obtained by rearranging the dynamic stiffness matrix of the unit cell [84], which needs to be evaluated for the

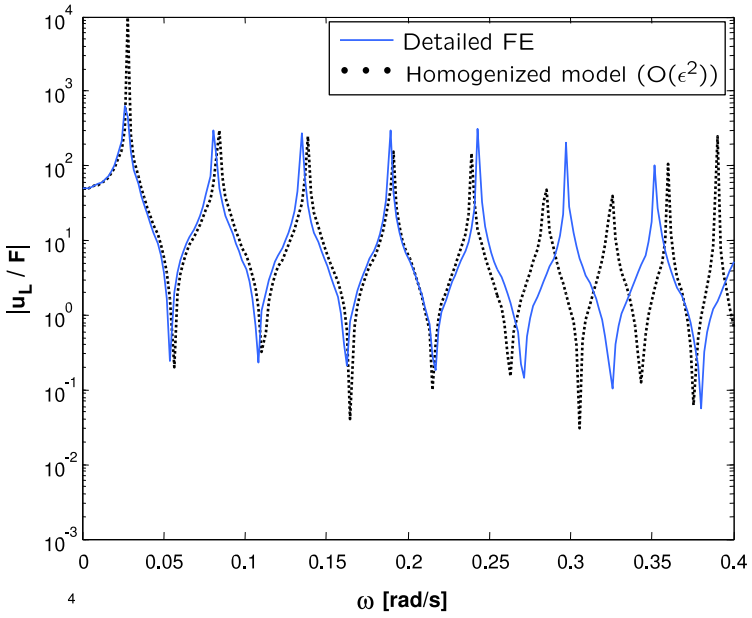

(a) Truss A

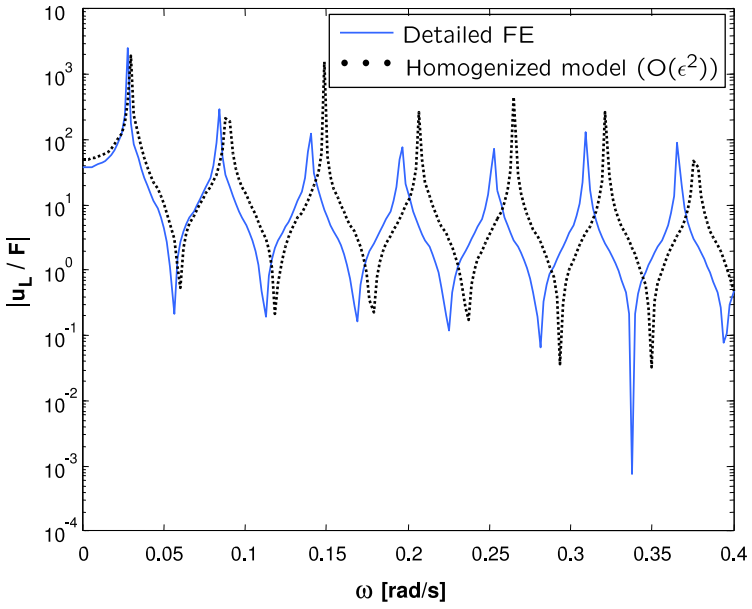

(b) Truss B

Figure 23: Frequency response function for the 1D trusses: comparison between detailed and homogenized models

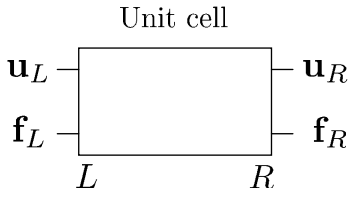

Figure 24: Schematic of a unit cell of a 1D periodic system

homogenization procedure. For varying frequency ω, the dispersion relation for the periodic domain can be simply obtained by imposing:

$$\det(\boldsymbol{T}) = 0 \tag{66}$$

whose solution gives wavenumbers which are as exact as the model used for the dynamic stiffness formulation of the unit cells. The obtained wavenumbers can be used in eq. (64),

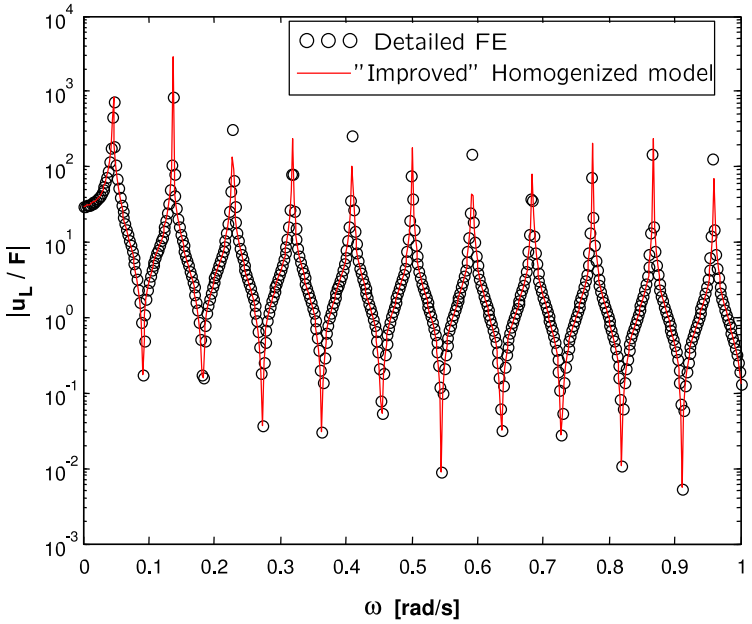

Figure 25: Frequency response function for the spring mass system: comparison between detailed and homogenized models obtained from exact solution of dispersion equation

instead of those obtained from the homogenized equation. The corresponding solution is not affected by approximations related to the truncation of the Taylor series expansion. The predicted FRF for the spring mass system and the trusses computed using the exact

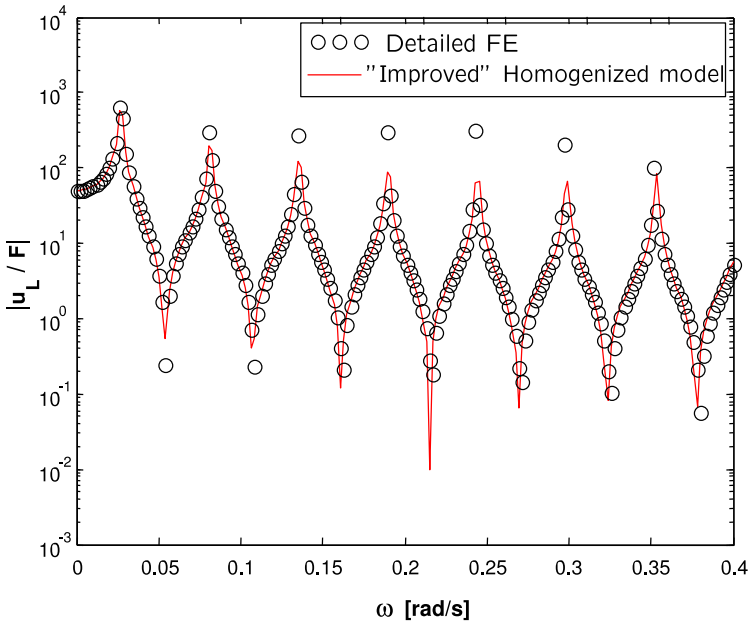

(a) Truss A

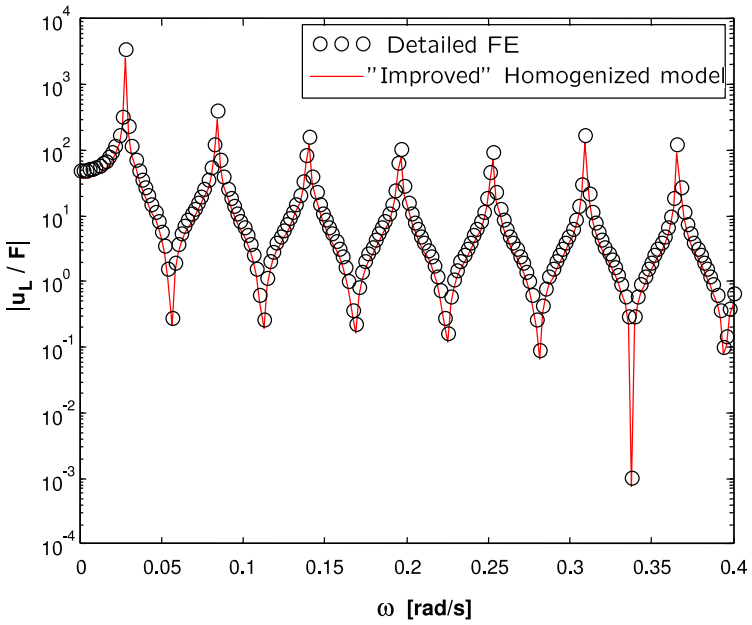

(b) Truss B

Figure 26: Frequency response function for the 1D trusses: comparison between detailed and homogenized models obtained from exact solution of dispersion equation

dispersion relation are shown in fig. 25 and fig. 26, which demonstrate the significant improvement in the accuracy of the response. Such an improvement is obtained through the analytical solution of a 2^{nd} order differential equation, without the need for the formulation of a large FE model accounting for all the components of the structures.

2.6 Two-dimensional Spring-mass Lattice

The homogenization technique is applied to a simple, mono-atomic two-dimensional (2D) system. The structure under consideration consists of a rectangular grid of point masses connected by springs. The grid is obtained by translation of the unit cell shown in fig. 27 along the x, y plane. The masses are assumed to move only along the z direction perpendicular to the plane of the grid. Each spring thus applies a force proportional to the relative out-of-plane displacements of the connected masses.

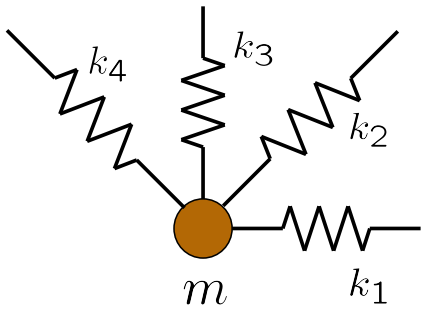

Figure 27: Unit cell of spring-mass lattice

2.6.1 Continuum equations

The scaled symbol for the grid is obtained through the procedure presented in Section 2 and it is given by:

$$\Gamma^{(\epsilon)}(\omega) = -\omega^2 m + 2\frac{k_1}{\epsilon^2}(1-\cos\epsilon\xi_1) + 2\frac{k_3}{\epsilon^2}(1-\cos\epsilon\xi_2) + 2\frac{k_2}{\epsilon^2}(1-\cos[\epsilon(\xi_1+\xi_2)]) + 2\frac{k_4}{\epsilon^2}(1-\cos[\epsilon(\xi_2-\xi_1)]) \tag{67}$$

Taking the Taylor series expansion based on the assumption of $\epsilon\xi \to 0$, and truncating to the first order gives:

$$[S^{(\epsilon,0)}(\omega)]^{-1} = -\omega^2 m + (k_1+k_2+k_4)\xi_1^2 + (k_3+k_2+k_4)\xi_2^2 + 2(k_2-k_4)\xi_1\xi_2 \tag{68}$$

Taking the inverse Fourier transformation of the approximated symbol yields:

$$(k_1 + k_2 + k_4)\frac{\partial^2 w(x,y)}{\partial x^2} + (k_3 + k_2 + k_4)\frac{\partial^2 w(x,y)}{\partial y^2} + \\ + 2(k_2 - k_4)\frac{\partial^2 w(x,y)}{\partial x \partial y} + \omega^2 m w(x,y) = f(x,y) \tag{69}$$

where $f(x,y)$ is the continuum equivalent load distributed over the surface of the grid as it appears in the general expression of eq. (41). Eq. (69) takes interesting forms for particular combinations of the spring constants. For example, if the diagonal springs have the same stiffness ($k_2 = k_4$), the term involving the mixed derivative in the differential equation vanishes, and eq. (69) reduces to:

$$(k_1 + 2k_2)\frac{\partial^2 w(x,y)}{\partial x^2} + (k_3 + 2k_2)\frac{\partial^2 w(x,y)}{\partial y^2} + \omega^2 m w(x,y) = f(x,y) \tag{70}$$

In addition, setting $k_1 = k_3$ results in the following compact expression:

$$\nabla^2 w(x,y) + \frac{\omega^2 m}{(k_1 + 2k_2)} w(x,y) = f(x,y) \tag{71}$$

which can be interpreted as the equation governing the out-of-plane harmonic motion of a membrane [59].

2.6.2 Dispersion relations

Exact and approximate dispersion relations for the considered grid are evaluated and compared. Similarly to what described for the 1D case, the exact dispersion relations are obtained by solving the generalized eigenvalue problem derived from the dynamic stiffness matrix of the unit cell, following the reduction procedure described in Section 2.3.3, and presented extensively in [74]. Exact and approximate relations are solved in terms of frequency ω, for assigned $\xi_k, (k = 1, 2)$. This results in 3D surfaces which represent the frequency of wave propagation corresponding to all the considered combinations of the wavenumbers ξ_k. These surfaces, known as "phase constant surfaces", are here represented using contour plots. As the phase constant surfaces are periodic with period equal to π [10], the representation and the evaluation of the phase constant surfaces is limited to the range $\xi_k \in [0, \pi]$. In fig. 28 dispersion relations for different orders of truncation of the Taylor series are shown respectively for $k_1 = k_3, k_2 = k_4 = 0$ and for $k_1 \neq k_3, k_2 = k_4 = 0$.

When not set equal to zero, the numerical values of the parameters of the system are: $m = 1\,kg$, $k_1 = 1\,N/m$, $k_2 = 0.5\,N/m$, $k_3 = 2\,N/m$, $k_4 = 0.75\,N/m$. It can be observed how the agreement between exact and approximate dispersion relations is generally good at low frequencies, and it improves with the order of the expansion.

2.6.3 Harmonic response through discretization of continuum equations

We consider a square lattice composed of a grid of 21 by 21 masses. This number is selected as a compromise between the need to make the direct computation of the response feasible, and the attempt to analyze a structure for which the homogenization approach might be meaningful. Each mass is loaded by a harmonic load acting along the z axis, which corresponds to a uniform distributed load after homogenization. The structure is constrained by setting all displacements along the boundaries of the grid to zero (see fig. 29).

The evaluation of the harmonic response requires the solution of eq. (69), which is derived from a first order truncation of the Taylor series. This limitation is again dictated by the impossibility of formulating a set of adequate and meaningful boundary conditions for higher order continuum equations. Moreover, the analytical solution of eq. (69) can only be found when the mixed derivative term is absent, i.e. when $k_2 = k_4$. A general approach requires instead the discretization of the equation using finite elements. The continuum equation is discretized by imposing a weak form [73] to obtain a "super-element" which approximates the homogenized continuous domain. This procedure still leads to a significant reduction in the number of degrees of freedom, particularly if large lattices are considered.

The comparison between exact predictions and those obtained from the continuum model is performed in terms of FRF for the displacement at the midpoint of the structure. The results for various lattice configurations are shown in fig. 30. The homogenized results are obtained by discretizing the equivalent continuum domain with a $20 * 20$ super-element mesh. The plots show how the agreement is excellent at the lower frequencies, and decreases as frequency increases, in accordance to the limits of the first order approximation.

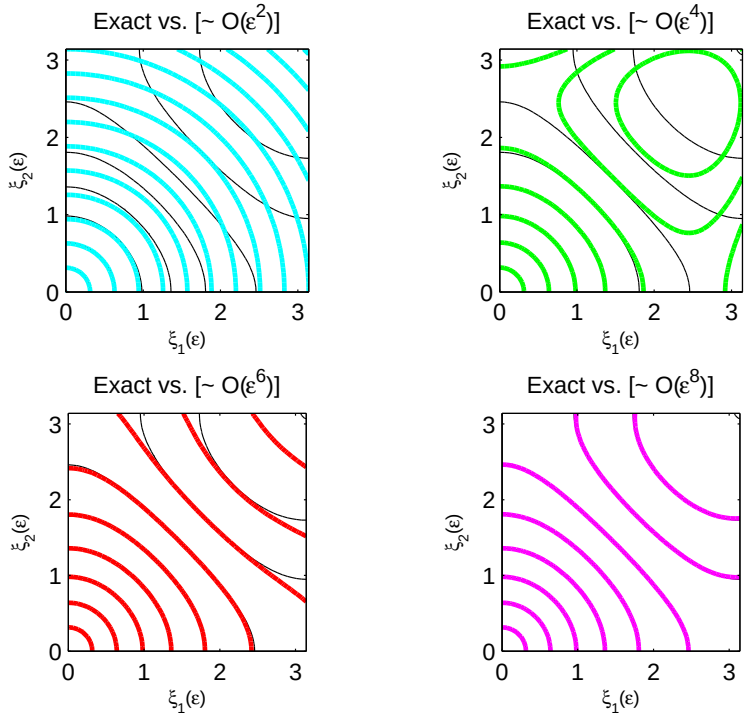

(a) $k_1 = k_3, k_2 = k_4 = 0$

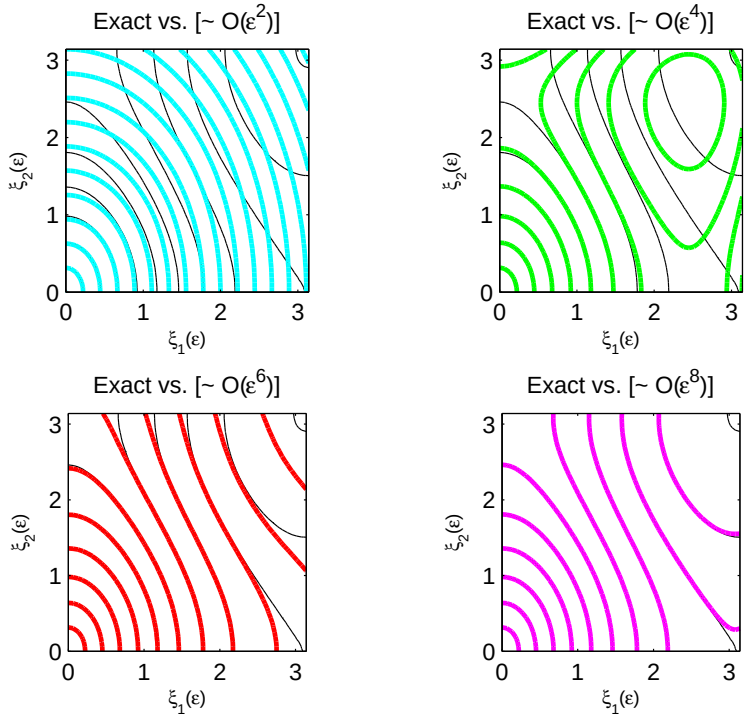

(b) $k_1 \neq k_3, k_2 = k_4 = 0$

Figure 28: Exact (thin line) and approximate (thick line) phase constant plots

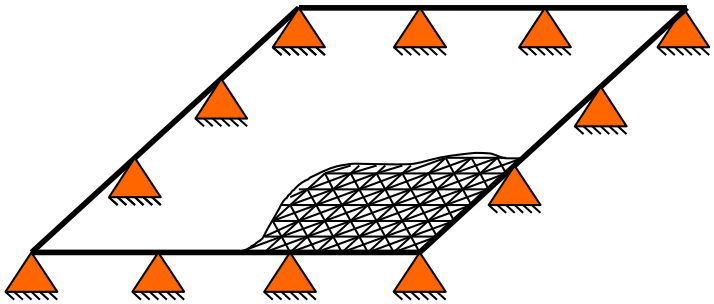

Figure 29: Boundary conditions on 2D grid

2.6.4 Refinement through improved approximation of the dispersion relations

An attempt to overcome the limitations in the evaluation of the response follows the same principles as the refinement technique presented for the 1D examples (section 2.5.6). In the homogenization technique here presented, the scaled symbol derived from the original lattice provides both the structure for the continuum equation and the coefficients of the equation. These coefficients are functions of the mechanical parameters of the system, of the frequency ω and of the scale factor ϵ. The idea is to maintain the structure of the differential equation (69) as suggested by the homogenization, while properly modifying its coefficients. In order to do so, the symbol is approximated with a function of the kind:

$$\Gamma^{(\epsilon)}(\omega) \simeq a_1\xi_1^2 + a_2\xi_2^2 + a_3\xi_1\xi_2 - m\omega^2 \tag{72}$$

where $a_i, (i = 1, .., 3)$ are coefficients of the corresponding continuum equation to be determined. At an assigned value of frequency ω, the coefficients a_i are selected in order to obtain the best fit of the dispersion relations at that frequency. This can be easily done using a standard least square method. To test the quality of the fit, we use eq. (72) to derive new dispersion relations and plot them as phase constant contours to be compared with the exact ones. The comparison shown in fig. 31 demonstrates how the imposed curves interpolate very well the contour lines of the exact phase constant surfaces for all values of ω. Given the coefficients a_i, the refined harmonic response for the system can be calculated by solving the following differential equation:

$$a_1(\omega)\frac{\partial^2 w}{\partial x^2} + a_2(\omega)\frac{\partial^2 w}{\partial y^2} + a_3(\omega)\frac{\partial^2 w}{\partial x \partial y} = f(x, y) \tag{73}$$

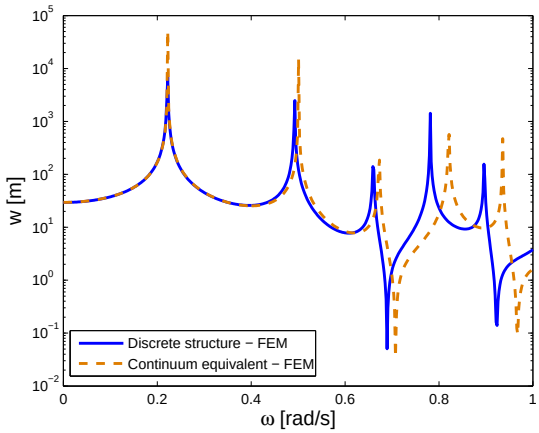

(a) $k_1 = k_3, k_2 = k_4 = 0$

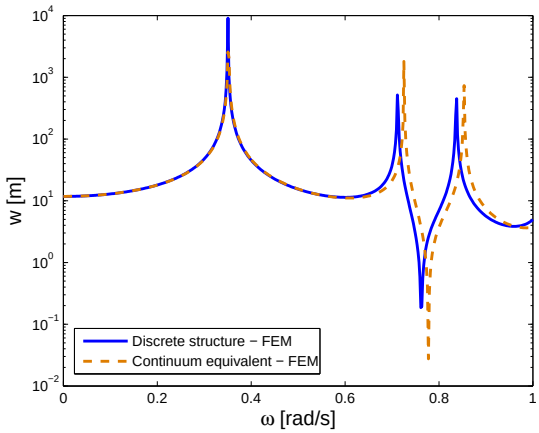

(b) $k_1 \neq k_3, k_2 = k_4$

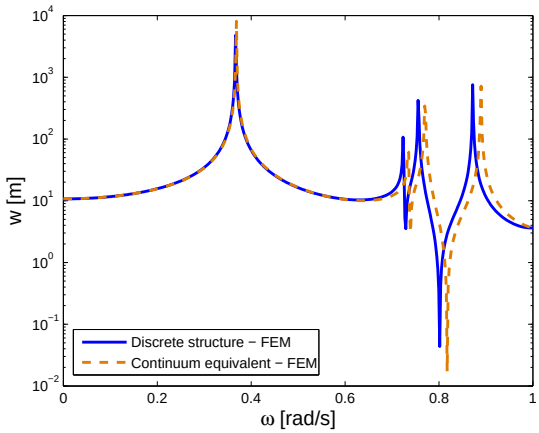

(c) $k_1 \neq k_3 \neq k_2 \neq k_4$

Figure 30: Midpoint displacement vs. frequency: comparison between complete solution and homogenized solution

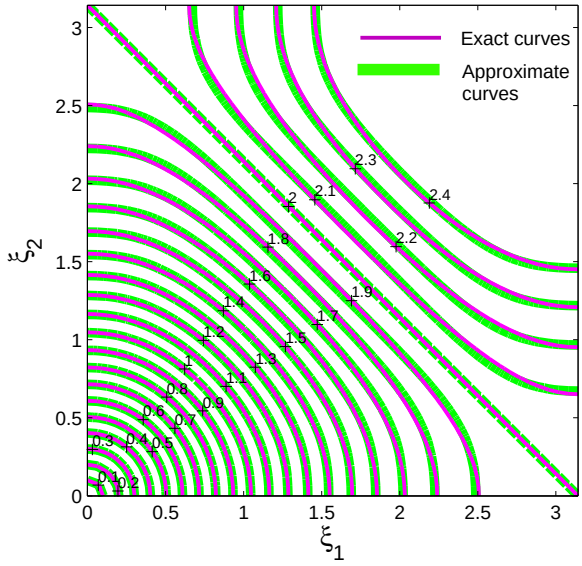

Figure 31: Interpolation of phase constant plots through least square methods - Orthogonal symmetric grid

A set of updated coefficients is calculated for all values of ω, so that eq. (73) can accurately approximate the behavior of the lattice over a wider frequency range. The FRFs obtained through this refined technique are shown in fig. 32, where an improved match can be observed.

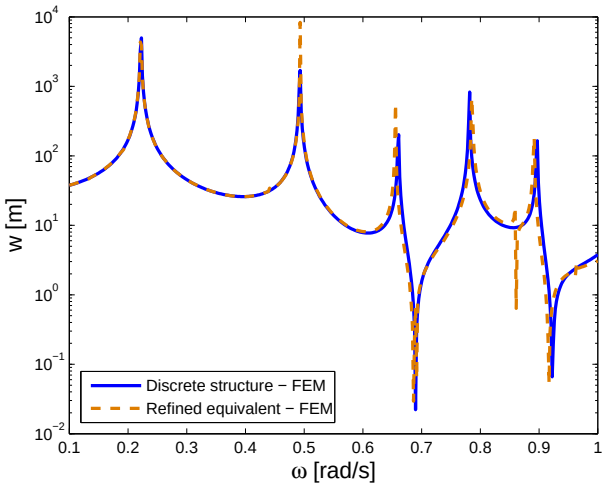

(a) $k_1 = k_3, k_2 = k_4 = 0$

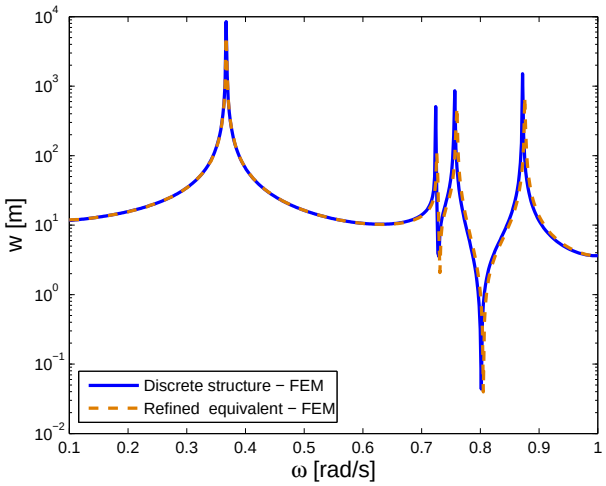

(b) $k_1 \neq k_3 \neq k_2 \neq k_4 \neq 0$

Figure 32: Midpoint displacement vs. frequency: comparison between complete solution and refined homogenized solution

CHAPTER III

HOMOGENIZATION THROUGH DIRECT TAYLOR SERIES EXPANSION IN THE SPATIAL DOMAIN

3.1 Introduction

A second approach to homogenization, alternative to the one presented in Chapter II, considers the approximation of continuum equations through the Taylor series expansion of the continuum variables in the spatial domain. This technique, here applied for the homogenization of periodic lattice structures, relies on the approximation of the discretized equations for the lattice through equivalent continuum equations obtained from their interpretation based on the finite differences formalism [81]. Differential operators replace the finite differences between nodal degrees of freedom of neighboring cells, upon Taylor series expansion. The technique and its results are essentially equivalent to the Fourier-based approach presented in Chapter II, as demonstrated in Appendix B. This alternative formulation is however significantly easier to generalize for complex structures and to implement in a numerical code. This chapter first gives a general presentation of the technique, and presents a simple example of its application to a square lattice. The analysis of regular and re-entrant hexagonal lattices is then presented, with the objective of identifying their equivalent mechanical properties and defining governing equations of elasticity.

3.2 Concept and Mathematical Formulation

3.2.1 Notation and general description of a lattice

Let us consider the two-dimensional lattice shown in fig. 33, where a unit cell of generic, complex internal structure is inscribed in a quadrilateral shaded gray area. As in any periodic assembly, the location of a point P can be described in terms of the location of the corresponding point in a reference unit cell and a set of lattice vectors which define directions along which each unit cell is repeated to generate the assembly. Accordingly, the

location of point P in cell n_1, n_2 can be expressed as:

$$\boldsymbol{\rho}_P(n_1, n_2) = \mathbf{r}_P + n_1\mathbf{e}_1 + n_2\mathbf{e}_2 \tag{74}$$

where $\mathbf{r}_P$ defines the position of the point corresponding to P in the reference cell $(0, 0)$, while $\mathbf{e}_1, \mathbf{e}_2$ respectively denote the lattice vectors. A cartesian reference frame $\mathcal{F}_\mathcal{I}$ in the plane of the lattice is defined by a unit vector basis $\mathcal{I} = (\mathbf{i}_1, \mathbf{i}_2)$. In addition, the lattice vectors define a frame $\mathcal{F}_\mathcal{E}$ with $\mathcal{E} = (\mathbf{e}_1, \mathbf{e}_2)$. The position of a point P in the cell can be expressed in either frame as follows:

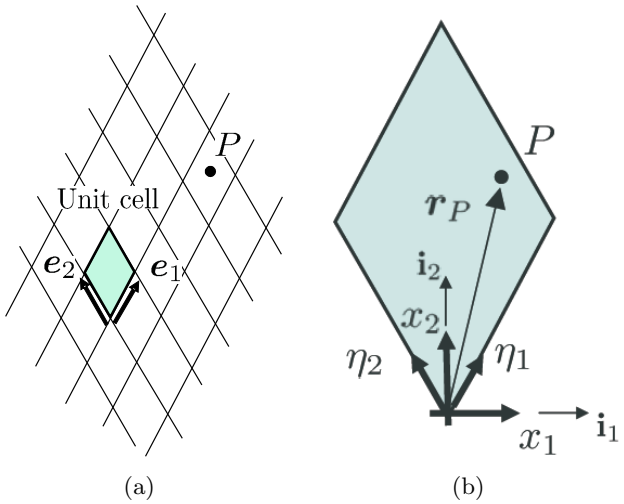

Figure 33: Schematic of generic lattice and unit cell with considered reference frames.

$$\mathbf{r}_P = x_1\mathbf{i}_1 + x_2\mathbf{i}_2 = \eta_1\mathbf{e}_1 + \eta_2\mathbf{e}_2 \tag{75}$$

where $\eta_1, \eta_2 \in [0,\ \ 1]$, with the components of the position vector in the two frames being related by:

$$[x_1,\ \ x_2]^T = \mathbf{E}\,[\eta_1,\ \ \eta_2]^T \tag{76}$$

where

$$\mathbf{E} = \begin{bmatrix} \mathbf{e_1} \cdot \mathbf{i_1} & \mathbf{e_2} \cdot \mathbf{i_1} \\ \mathbf{e_1} \cdot \mathbf{i_2} & \mathbf{e_2} \cdot \mathbf{i_2} \end{bmatrix} \tag{77}$$

Matrix $\mathbf{E}$, known as "lattice (transformation) matrix", maps the quadrilateral geometry inscribing the considered generic unit cell to a square of unit area. The result of this

geometric mapping is represented schematically in fig. 34. The description of the lattice as assembly of square unit cells simplifies the presentation of the homogenization approach to follow.

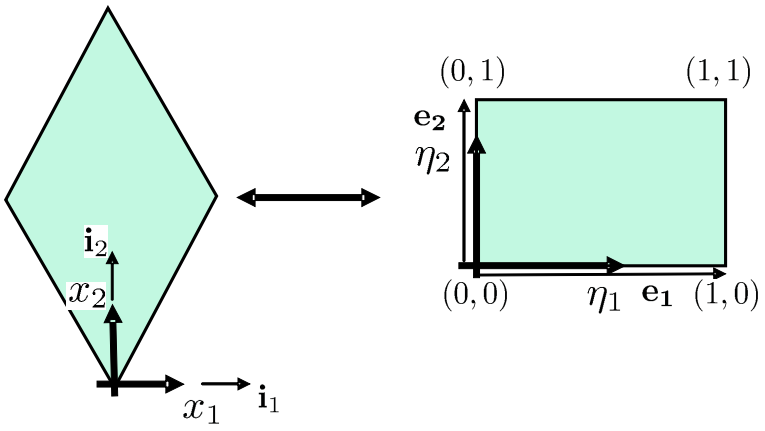

Figure 34: Mapping of the unit cell into the lattice space

3.2.2 Discretized equations of motion and derivation of continuum equations

Consider a unit cell (i, j) connected to three neighboring cells, as shown in fig. 35, where the square topology is the result of its representation in the lattice space. The boundary nodes of the cells are denoted by two indexes $m, n \in [-1, 1]$. It is assumed that the behavior of each unit cell is described in terms of mass and stiffness matrices relating the degrees of freedom of the boundary nodes highlighted in the figure. This implies the absence of internal degrees of freedom, or a previous operation whereby internal degrees of freedom are condensed out through the application of standard condensation techniques [13], or more dedicated and advanced reduction techniques as described in [11]. Accordingly, the equation of motion for the reference node $(0, 0)$ can be expressed as:

$$\sum_{m,n=-1}^{+1} \mathbf{K}^{(m,n)}\mathbf{u}^{(m,n)} + \mathbf{M}^{(m,n)}\ddot{\mathbf{u}}^{(m,n)} = \mathbf{f}^{(0,0)} \tag{78}$$

where $\mathbf{u}^{(m,n)}$ denotes the generalized displacements of node (m, n), $\mathbf{f}^{(0,0)}$ is the vector of the generalized forces applied to node $(0, 0)$, while $\mathbf{K}^{(m,n)}$ and $\mathbf{M}^{(m,n)}$ are proper partitions of the mass and stiffness matrices for the four-cell assembly in fig. 35. The homogenization technique under consideration consists in introducing an equivalent, continuous vector of

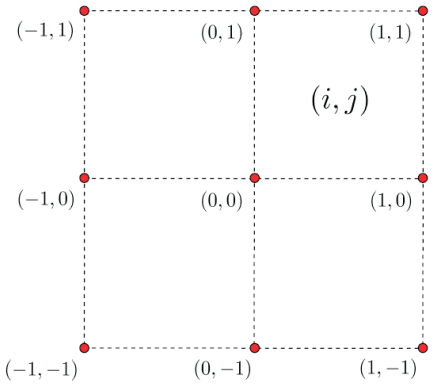

Figure 35: Lattice topology in the lattice space

generalized displacements $\boldsymbol{u} = \boldsymbol{u}(\eta_1, \eta_2)$ which is related to the discrete vector of degrees of freedom $\mathbf{u}^{(m,n)}$ by the following Taylor series expansion:

$$\mathbf{u}^{(m,n)} \approx \boldsymbol{u}(\eta_1, \eta_2) + m\frac{\partial \boldsymbol{u}}{\partial \eta_1} + n\frac{\partial \boldsymbol{u}}{\partial \eta_2} + \frac{1}{2}m^2\frac{\partial^2 \boldsymbol{u}}{\partial \eta_1^2} + \frac{1}{2}n^2\frac{\partial^2 \boldsymbol{u}}{\partial \eta_2^2} + mn\frac{\partial^2 \boldsymbol{u}}{\partial \eta_1 \partial \eta_2} + ... \tag{79}$$

Similarly, the vector of the applied forces is replaced by a continuous force distribution:

$$\mathbf{f}^{(0,0)} \approx \boldsymbol{f}(\eta_1, \eta_2) \tag{80}$$

Substituting eq.s (79) and (80) into eq. (78) yields the following set of Partial Differential Equations (PDEs):

$$A'\boldsymbol{u}_{,\eta_1\eta_1} + B'\boldsymbol{u}_{,\eta_1\eta_2} + C'\boldsymbol{u}_{,\eta_2\eta_2} + D'\boldsymbol{u}_{,\eta_1} + E'\boldsymbol{u}_{,\eta_2} + F'\boldsymbol{u} + \tag{81}$$

$$+A'_m\ddot{\boldsymbol{u}}_{,\eta_1\eta_1} + B'_m\ddot{\boldsymbol{u}}_{,\eta_1\eta_2} + C'_m\ddot{\boldsymbol{u}}_{,\eta_2\eta_2} + D'_m\ddot{\boldsymbol{u}}_{,\eta_1} + E'_m\ddot{\boldsymbol{u}}_{,\eta_2} + F'_m\ddot{\boldsymbol{u}} = \boldsymbol{f}$$

where:

$$\begin{aligned}
A' &= \sum_{m,n} m^2\mathbf{K}^{(m,n)}, \\
B' &= \sum_{m,n} mn\mathbf{K}^{(m,n)}, \\
C' &= \sum_{m,n} n^2\mathbf{K}^{(m,n)}, \\
D' &= \sum_{m,n} m\mathbf{K}^{(m,n)}, \\
E' &= \sum_{m,n} n\mathbf{K}^{(m,n)}, \\
F' &= \sum_{m,n} \mathbf{K}^{(m,n)}
\end{aligned}$$

and

$$\begin{aligned} A'_m &= \sum_{m,n} m^2 \mathbf{M}^{(m,n)}, \\ B'_m &= \sum_{m,n} mn \mathbf{M}^{(m,n)}, \\ C'_m &= \sum_{m,n} n^2 \mathbf{M}^{(m,n)}, \\ D'_m &= \sum_{m,n} m \mathbf{M}^{(m,n)}, \\ E'_m &= \sum_{m,n} n \mathbf{M}^{(m,n)}, \\ F'_m &= \sum_{m,n} \mathbf{M}^{(m,n)} \end{aligned}$$

with the notation $()_{,\eta_i}$ denoting partial derivatives with respect the the variable η_i, $(i = 1, 2)$. Equation (81) is a system of PDEs, whose dimension depends on the number of degrees of freedom used to describe the behavior of the lattice nodes. The PDEs are continuous equations which govern the behavior of the elastic continuum equivalent to the lattice under consideration. The validity of the approximation is related to the Taylor series expansion in which a scaling parameter is introduced to define the order of the approximation. The effect of the scaling parameter will be explained later in this chapter by means of an example.

A simple coordinate transformation can be performed to express the equivalent continuum equations in the cartesian frame $\mathcal{F}_{\mathcal{I}}$. Letting:

$$\begin{pmatrix} \frac{\partial}{\partial \eta_1} \\ \frac{\partial}{\partial \eta_2} \end{pmatrix} = \mathbf{E} \begin{pmatrix} \frac{\partial}{\partial x_1} \\ \frac{\partial}{\partial x_2} \end{pmatrix} \tag{82}$$

and

$$\begin{pmatrix} \frac{\partial^2}{\partial \eta_1^2} \\ \frac{\partial^2}{\partial \eta_2^2} \\ \frac{\partial^2}{\partial \eta_1 \partial \eta_2} \end{pmatrix} = \begin{bmatrix} e_{11}^2 & e_{21}^2 & 2e_{11}e_{21} \\ e_{12}^2 & e_{22}^2 & 2e_{11}e_{12} \\ e_{11}e_{12} & e_{21}e_{22} & e_{12}e_{21} + e_{11}e_{22} \end{bmatrix} \begin{pmatrix} \frac{\partial^2}{\partial x_1^2} \\ \frac{\partial^2}{\partial x_2^2} \\ \frac{\partial^2}{\partial x_1 \partial x_2} \end{pmatrix} \tag{83}$$

with e_{ij} denoting the i, j component of the lattice matrix $\mathbf{E}$, yields:

$$A\boldsymbol{u}_{,x_1x_1} + B\boldsymbol{u}_{,x_1x_2} + C\boldsymbol{u}_{,x_2x_2} + D\boldsymbol{u}_{,x_1} + E\boldsymbol{u}_{,x_2} + F\boldsymbol{u} + \tag{84}$$

$$+A_m\ddot{\boldsymbol{u}}_{,x_1x_1} + B_m\ddot{\boldsymbol{u}}_{,x_1x_2} + C_m\ddot{\boldsymbol{u}}_{,x_2x_2} + D_m\ddot{\boldsymbol{u}}_{,x_1} + E_m\ddot{\boldsymbol{u}}_{,x_2} + F_m\ddot{\boldsymbol{u}} = \boldsymbol{f}$$

where $A \dots F$ and $A_m \dots F_m$ are obtained as linear combinations of $A' \dots F'$ and $A'_m \dots F'_m$ through the coefficients e_{ij}.

The form of the equivalent continuum equations simplifies considerably if a lumped mass description is considered for the lattice. Lumped mass matrices can be obtained from the consistent ones through simple techniques such as the row sum technique presented in [5]. In this case, the discretized equation of motion for node $(0,0)$ common to the four-cell assembly of fig. 35 becomes:

$$\mathbf{M}^{(0,0)}\ddot{\mathbf{u}}^{(0,0)} + \sum_{m,n=-1}^{+1} \mathbf{K}^{(m,n)}\mathbf{u}^{(m,n)} = \mathbf{f}^{(0,0)} \tag{85}$$

Substituting the continuous generalized displacement variables and performing the Taylor series expansion yields:

$$A\boldsymbol{u}_{,x_1x_1} + B\boldsymbol{u}_{,x_1x_2} + C\boldsymbol{u}_{,x_2x_2} + D\boldsymbol{u}_{,x_1} + E\boldsymbol{u}_{,x_2} + F\boldsymbol{u} + F_m\ddot{\boldsymbol{u}} = \boldsymbol{f} \tag{86}$$

3.2.3 Example: in-plane behavior of a square lattice

The technique can be illustrated by considering the simple case of the square lattice shown in fig. 36.a, where L denotes the overall (macroscopic) dimensions of the lattice. The 4-cell assembly and the parameters defining the unit cell geometry are depicted in fig. 36.b. For

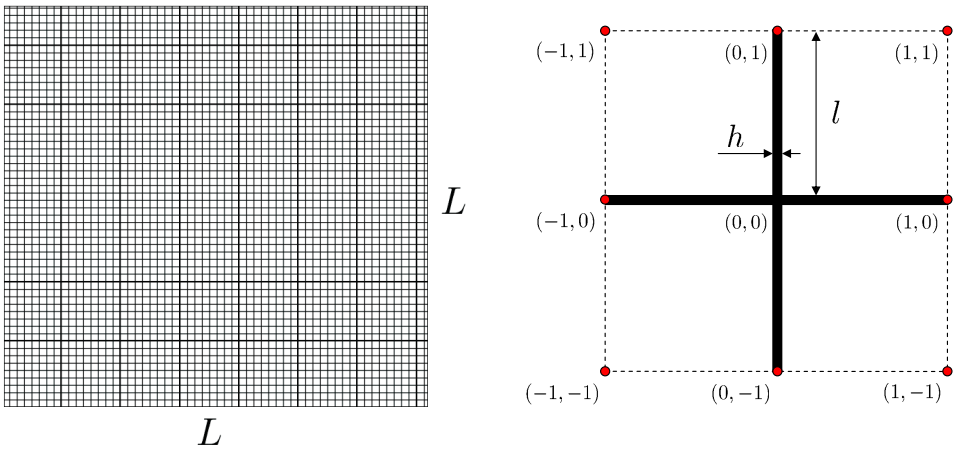

(a) Square lattice (b) Unit cell

Figure 36: Square lattice and unit cell geometry

simplicity the unit cell is modeled as two perpendicular beam elements. The behavior of

each beam is defined by the degrees of freedom of the two nodes, which include two in plane displacements and a rotation about the out-of-plane axis, according to the schematic of fig 37. Accordingly, the vector of the nodal generalized displacements $\boldsymbol{u}^{(m,n)}$ is a 3×1 array, and the sub-matrices $\mathbf{K}^{(m,n)}, \mathbf{M}^{(m,n)}$ in eq. (78) are 3×3. The standard Euler-Bernoulli formulation with hermitian polynomials as shapes functions is employed for simplicity, with the lumped mass matrix being obtained through the application of the row sum technique. It is worth noting that the formulation or the complexity of the procedure are not affected by the consideration of a higher order beam theory, to include for example shear deformations. The simple formulation adopted here is however chosen as it leads to a very convenient interpretation of the results. The simplicity of the lattice topology also introduces the following simplifications:

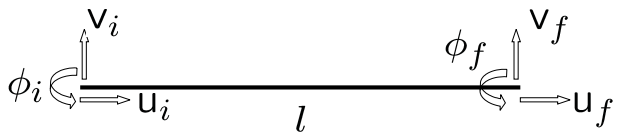

Figure 37: Degrees of freedom of beam elements

$$\mathbf{K}^{(+1,+1)} = \mathbf{K}^{(-1,+1)} = \mathbf{K}^{(+1,-1)} = \mathbf{K}^{(-1,-1)} = \mathbf{0} \tag{87}$$

The geometry of the unit cell can be defined in terms of a slenderness ratio $\beta = h/l$, and of a scaling parameter ϵ which relates the characteristic dimensions of the lattice and of the unit cell, respectively denoted as L and l. According to the underlying assumption of the multiscale analysis:

$$\epsilon = \frac{l}{L} \ll 1 \tag{88}$$

Equation (88) allows the introduction of the scaling parameter in the unit cell stiffness and mass matrices, and its propagation through the process. The results obtained upon performing the Taylor series expansion can be then truncated to a specified order of ϵ. This process can be very conveniently implemented as part of a symbolic solver, where ϵ is left as a symbolic term, or in a completely numerical code, which selects and truncates terms below a specified order of magnitude, as defined by the value of ϵ. The introduction of ϵ in

the formulation is based on the following substitutions:

$$l = \epsilon L \tag{89}$$

and

$$h = \epsilon \beta L \tag{90}$$

which affect the area properties of the beam elements:

$$A = h = \epsilon \beta L \tag{91}$$

$$I = \frac{1}{12} h^3 = \frac{1}{12} \epsilon^3 \beta^3 L^3 \tag{92}$$

and the lattice matrix $\mathbf{E}$ which in this case is given by:

$$\mathbf{E} = \begin{bmatrix} l & 0 \\ 0 & l \end{bmatrix} = \epsilon \begin{bmatrix} L & 0 \\ 0 & L \end{bmatrix} \tag{93}$$

where A and I respectively denote the beam cross sectional area and the 2^{nd} moment of area, evaluated under the assumption of unit out-of-plane width.

Applying the technique and performing truncation to exclude all terms $\mathcal{O}(\epsilon^5)$ yields the following set of PDEs:

$$\begin{gathered} E\frac{h}{l}\epsilon^2 L^2 u_{,x_1x_1} + E\left(\frac{h}{l}\right)^3 \epsilon^2 L^2 u_{,x_2x_2} - E\left(\frac{h}{l}\right)^3 \epsilon^2 L^2 \phi_{,x_2} - \rho\frac{2h}{l}\epsilon^2 L^2 \ddot{u} = f_u \\ E\left(\frac{h}{l}\right)^3 \epsilon^2 L^2 v_{,x_1x_1} + E\frac{h}{l}\epsilon^2 L^2 v_{,x_2x_2} + E\left(\frac{h}{l}\right)^3 \epsilon^2 L^2 \phi_{,x_1} - \rho\frac{2h}{l}\epsilon^2 L^2 \ddot{v} = f_v \\ \frac{1}{6}E\left(\frac{h}{l}\right)^3 \epsilon^4 L^4 \phi_{,x_1x_1} + \frac{1}{6}E\left(\frac{h}{l}\right)^3 \epsilon^4 L^4 \phi_{,x_2x_2} + E\left(\frac{h}{l}\right)^3 \epsilon^2 L^2 v_{,x_1} - E\left(\frac{h}{l}\right)^3 \epsilon^2 L^2 u_{,x_2} + \\ +2E\left(\frac{h}{l}\right)^3 \epsilon^2 L^2 \phi - \frac{1}{105}\rho\frac{h}{l}\epsilon^4 L^4 \ddot{\phi} = m_\phi \end{gathered} \tag{94}$$

where E and ρ are the Young's modulus and the density of the lattice material, u, v, ϕ are the two in-plane displacement components and rotation, while f_u, f_v, m_ϕ denote the corresponding generalized loads. It can be noticed that the elastic terms involving the second derivatives of ϕ and the inertial term in the third equation are $\mathcal{O}(\epsilon^4)$, while all other terms are $\mathcal{O}(\epsilon^2)$. One could alternatively interpret these terms as $o(\epsilon^2)$ for $\epsilon \to 0$ and

directly eliminate them from the equations or divide the equations through by $\epsilon^2 L^2$ and take the limit for $\epsilon \to 0$. Either way the equations reduce to:

$$\begin{aligned} E\frac{h}{l}u_{,x_1x_1} + E\left(\frac{h}{l}\right)^3 u_{,x_2x_2} - E\left(\frac{h}{l}\right)^3 \phi_{,x_2} - \rho\frac{2h}{l}\ddot{u} &= \frac{f_u}{l^2} \\ E\left(\frac{h}{l}\right)^3 v_{,x_1x_1} + E\frac{h}{l}v_{,x_2x_2} + E\left(\frac{h}{l}\right)^3 \phi_{,x_1} - \rho\frac{2h}{l}\ddot{v} &= \frac{f_v}{l^2} \\ E\left(\frac{h}{l}\right)^3 v_{,x_1} - E\left(\frac{h}{l}\right)^3 u_{,x_2} + 2E\left(\frac{h}{l}\right)^3 \phi &= \frac{m_\phi}{l^2} \end{aligned} \tag{95}$$

where the relation $l^2 = \epsilon^2 L^2$ has been used. Equation (95) can be interpreted as a set of in-plane elasticity equations for a micropolar continuum involving two in-plane displacements u and v a microrotation ϕ. If no concentrated couples are applied to the structure ($m_\phi = 0$), the degree of freedom ϕ can be eliminated from the equations. That is done by calculating ϕ from the 3^{rd} equation and substituting the result in the first two. This gives:

$$\begin{aligned} E\frac{h}{l}u_{,x_1x_1} + \frac{1}{2}E\left(\frac{h}{l}\right)^3 u_{,x_2x_2} + \frac{1}{2}E\left(\frac{h}{l}\right)^3 v_{,x_1x_2} - \rho\frac{2h}{l}\ddot{u} &= q_u \\ \frac{1}{2}E\left(\frac{h}{l}\right)^3 v_{,x_1x_1} + E\frac{h}{l}v_{,x_2x_2} + \frac{1}{2}E\left(\frac{h}{l}\right)^3 u_{,x_1x_2} - \rho\frac{2h}{l}\ddot{v} &= q_v \end{aligned} \tag{96}$$

where $q_u = f_u/l^2$ and $q_v = f_v/l^2$ are area loads corresponding to the load distributions on the unit cell. Equation (96) is a system of two equations in the variables u and v and involves a classical linear elasticity operator. The coefficients of the differential operators are functions of the geometric and material properties of the beams constituting the unit cell. The equations of elasticity for an orthotropic, two-dimensional elastic domain in plain stress conditions are:

$$\begin{aligned} \frac{E_1}{1-\nu_{12}\nu_{21}}u_{,x_1x_1} + G_{12}u_{,x_2x_2} + \left(G_{12} + \frac{\nu_{12}E_2}{1-\nu_{12}\nu_{21}}\right)v_{,x_1x_2} - \rho\ddot{u} &= q_u \\ G_{12}v_{,x_1x_1} + \frac{E_2}{1-\nu_{12}\nu_{21}}v_{,x_2x_2} + \left(G_{12} + \frac{\nu_{12}E_2}{1-\nu_{12}\nu_{21}}\right)u_{,x_1x_2} - \rho\ddot{v} &= q_v \end{aligned} \tag{97}$$

where the indexes $'1', '2'$ indicate the directions of the lattice, along the cartesian frame. Direct comparison between the coefficients of the homogenized equations and the elasticity equations for the orthotropic continuum allows the identification of equivalent mechanical properties for the square lattice. For instance, the inertia term contains the relative density of the unity cell, which is given by:

$$\bar{\rho} = \frac{2h}{l} \tag{98}$$

Also, the equivalent moduli of elasticity can be expressed as:

$$E_1 = E_2 = E\frac{h}{l} \tag{99}$$

$$G_{12} = E\frac{1}{2}\left(\frac{h}{l}\right)^3 \tag{100}$$

Finally, the equivalent Poisson's ratios are:

$$\nu_{12} = \nu_{21} = 0 \tag{101}$$

These expressions for the equivalent properties of the square lattice match exactly the expressions available in the literature [26], which are obtained through the application of basic deformation analysis of the lattice beams. The advantage of the proposed formulation with respect to the approach presented in [26] consists on the simplicity of its implementation, and the resulting ease through which more detailed deformation mechanisms can be included in the model, such as for example shear deformation and higher order strain theories. In addition, the present formulation directly provides the inertia term, which is essential for the application of the equivalent continuum equations as part of a dynamic analysis. A drawback of the technique, which will become apparent in the following sections, is the difficulty in obtaining closed-form, analytical expressions for the equivalent properties, particularly when the cell's internal structure increases in complexity. However, the technique is very general and can be employed to obtain equivalent governing equations, which can be solved through typical numerical techniques, or can be directly fed to one of the commercially available PDEs solvers, such as COMSOL Multiphysics®. This may lead to substantial reductions in computational cost, with respect to a full, detailed analysis of the lattice.

An example of dynamic application of the homogenized equations is the evaluation of the phase velocities, and their variation with respect to the direction of wave propagation. This information for non-dispersive media is typically represented in the form of slowness curves [1], which are extremely useful in highlighting for example the anisotropy of the medium under consideration. In here, it is selected to directly evaluate the phase velocities for direct comparison of the results with published values [80]. The procedure for the evaluation of

the phase velocities consists in substituting in the governing equations a solution of the kind:

$$\boldsymbol{u} = \boldsymbol{u}_0 e^{i\boldsymbol{k}\cdot\boldsymbol{r}} e^{i\omega t} \tag{102}$$

where $\boldsymbol{u} = [u \quad v]^T$, while:

$$\boldsymbol{k} = k_1\boldsymbol{i}_1 + k_2\boldsymbol{i}_2 = k(\cos\gamma\boldsymbol{i}_1 + \sin\gamma\boldsymbol{i}_2) \tag{103}$$

$$\boldsymbol{r} = x_1\boldsymbol{i}_1 + x_2\boldsymbol{i}_2 \tag{104}$$

where k is the wavenumber, and γ defines the direction of wave propagation. Substituting eq. (102) into the continuum equations yields the following eigenvalue problem:

$$[c_{ph}^2\boldsymbol{\Gamma}(\gamma) - \rho\mathbf{I}]\boldsymbol{u}_0 = \mathbf{0} \tag{105}$$

where $c_{ph} = k/\omega$ is the unknown phase velocity, $\boldsymbol{\Gamma}$ is a matrix containing the elasticity coefficients of the considered domain, and $\mathbf{I}$ is a 2×2 identity matrix. Results obtained for the two propagation modes and $\gamma \in [0 \;\; 2\pi]$ are shown in fig. 38. Analytical expressions for the wave speeds corresponding to propagation along the lattice axis x_1, obtained by letting $\gamma = 0$ in eq. (105), are:

$$c_P = \sqrt{\frac{E}{2\rho}} \tag{106}$$

$$c_S = \frac{1}{2}\frac{h}{L}\sqrt{\frac{E}{\rho}} \tag{107}$$

whose values are presented as a dot in fig. 38. The analytical expressions for the phase velocities also match those reported in the literature [80, 26].

3.3 Homogenization of Hexagonal and Re-entrant Lattices

3.3.1 Definition of the problem

We investigate the characteristics of hexagonal lattices of the kind shown in fig. 39, which are obtained from the assembly of unit cells of the kind shown in fig. 40. The geometry of the unit cell is defined by the internal angle θ, and by the ratios $\alpha = H/L$ and $\beta = h/L$ which respectively define the relative cell wall lengths, and the walls' slenderness ratio. For

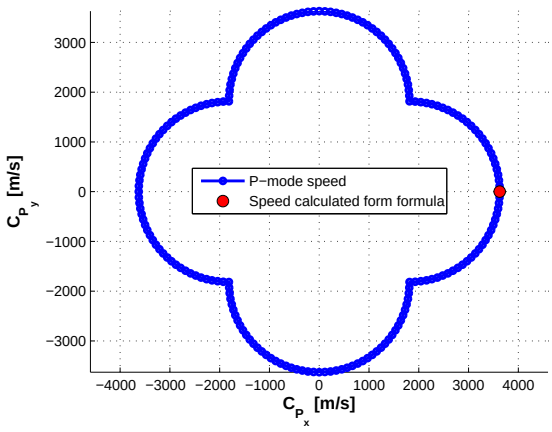

(a) P-mode

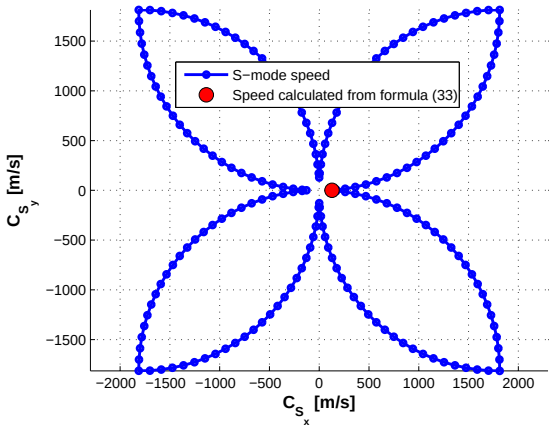

(b) S-mode

Figure 38: Variation of phase velocity in terms of direction of wave propagation for the two propagation modes defined by the homogenized model

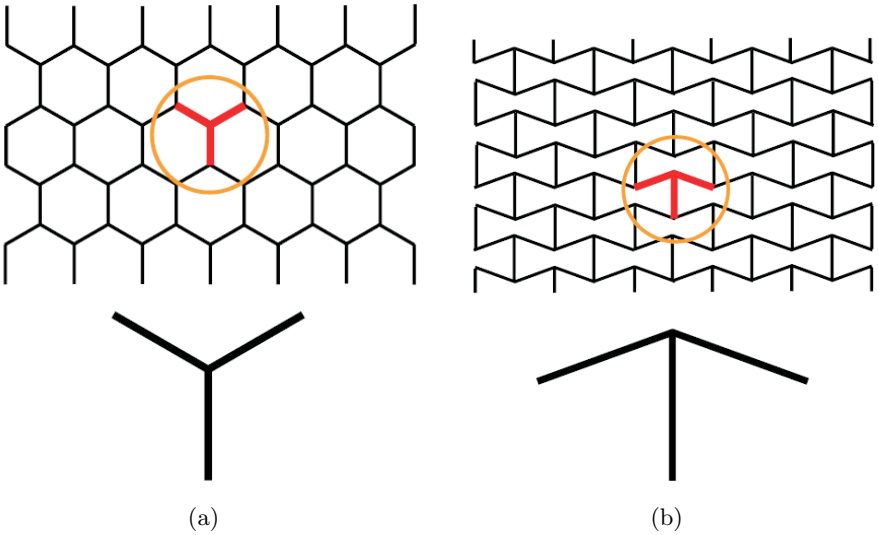

Figure 39: Hexagonal and re-entrant lattices

example, a regular hexagonal lattice is defined by $\theta = 30^o$ and $\alpha = 1$, while re-entrant lattices of the kind shown in fig 39.b are characterized by negative values of θ. Such lattices are of particular interest as they feature a negative in-plane Poisson's ratio, and for this reason they have been termed as *auxetic* [24, 71]. Auxetic lattices also have interesting properties with regards to the propagation of out-of-plane elastic waves as discussed in [74], among others. The lattice vectors can be expressed in terms of the characteristic unit cell

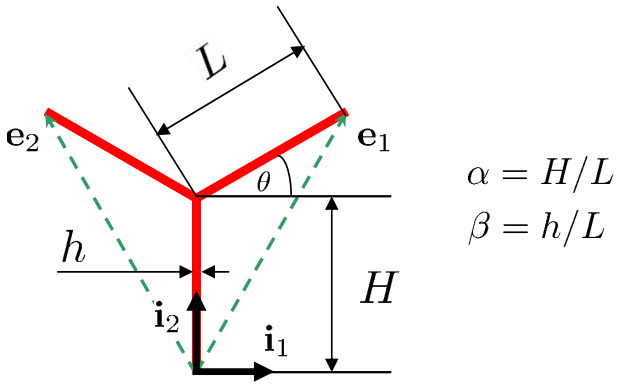

Figure 40: Unit cell and main dimensions

parameters as:

$$\begin{aligned} \mathbf{e}_1 &= L\cos\theta\mathbf{i}_1 + (H + L\sin\theta)\mathbf{i}_2 \\ \mathbf{e}_2 &= -L\cos\theta\mathbf{i}_1 + (H + L\sin\theta)\mathbf{i}_2 \end{aligned} \tag{108}$$

The derivation of homogenized equations of motion governing the in-plane behavior of hexagonal lattices can be obtained following the Taylor-series based procedure introduced in previous paragraphs. The Y-shaped unit cell described above can be maintained as the RVE for the following analysis. Given the lattice space $\mathbf{e}_1, \mathbf{e}_2$, the domain shown in fig. 41.a, consisting of four neighboring unit cells, can be mapped into the lattice space, resulting in the configuration of fig. 41.b. In the case of hexagonal lattices, even when

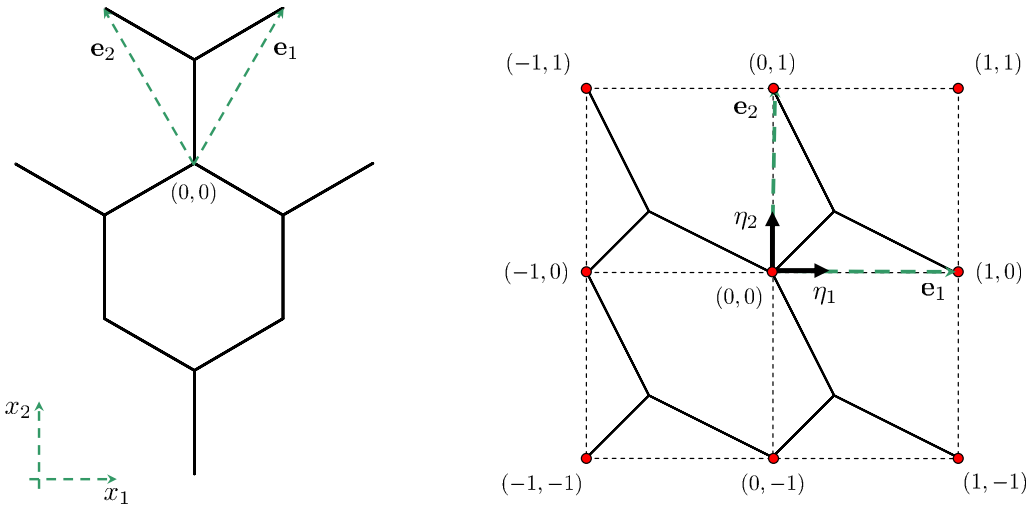

(a) Geometric space

(b) Lattice direct space

Figure 41: Macro-cell of hexagonal lattice in geometric and lattice space

each link of the assembly is modelled with a single beam element, the unit cell features at least one internal node which is not shared with any of the neighboring cells. Since the homogenization technique presented above requires the structure to be described in terms of the degrees of freedom of the boundary nodes, a reduction is needed in order to make the unit cell compatible with the presented procedure. This result can be achieved by performing a condensation of the internal degrees of freedom. This is a quite common procedure in FE analysis and fits perfectly within the FE-based homogenization technique

that is here adopted. Performing a static condensation within the solution of a dynamic problem inevitably introduces an approximation which is as significant as the number of condensed degrees of freedom is large. It is therefore important to estimate the effects of this additional approximation to understand whether it may or may not affect the final outcome of the analysis. The accuracy of the condensation is discussed later in the chapter.

3.3.2 Homogenized equations of motion

Since the beams are modelled to account for both axial and flexural deformations, each lattice node is described in terms of the array of nodal degrees of freedom $[u, v, \phi]^T$. Application of the homogenization procedure yields a system of three equations in the three continuum variables u, v and ϕ, which can be expressed in compact form as:

$$A\boldsymbol{u}_{,x_1x_1} + B\boldsymbol{u}_{,x_1x_2} + C\boldsymbol{u}_{,x_2x_2} + D\boldsymbol{u}_{,x_1} + E\boldsymbol{u}_{,x_2} + F\boldsymbol{u} + F_m\ddot{\boldsymbol{u}} = \boldsymbol{f} \tag{109}$$

where $\boldsymbol{u} = [u, v, \phi]^T$ and matrices $A \dots F$ feature the following internal structure:

$$\begin{aligned} A &= \begin{bmatrix} A_{11} & 0 & 0 \\ 0 & A_{22} & 0 \\ 0 & 0 & 0 \end{bmatrix} \quad B = \begin{bmatrix} 0 & B_{12} & 0 \\ B_{21} & 0 & 0 \\ 0 & 0 & 0 \end{bmatrix} \quad C = \begin{bmatrix} C_{11} & 0 & 0 \\ 0 & C_{22} & 0 \\ 0 & 0 & 0 \end{bmatrix} \\ D &= \begin{bmatrix} 0 & 0 & 0 \\ 0 & 0 & D_{23} \\ 0 & D_{32} & 0 \end{bmatrix} \quad E = \begin{bmatrix} 0 & 0 & E_{13} \\ 0 & 0 & 0 \\ E_{31} & 0 & 0 \end{bmatrix} \quad F = \begin{bmatrix} 0 & 0 & 0 \\ 0 & 0 & 0 \\ 0 & 0 & F_{33} \end{bmatrix} \end{aligned} \tag{110}$$

while F_m, under the assumption of lumped mass, becomes:

$$F_m = \begin{bmatrix} F_{m_{11}} & 0 & 0 \\ 0 & F_{m_{22}} & 0 \\ 0 & 0 & 0 \end{bmatrix} \tag{111}$$

By means of eq. (110), eq. (109) can be recast as:

$$\begin{aligned} A_{11}u_{,x_1x_1} + C_{11}u_{,x_2x_2} + B_{12}v_{,x_1x_2} + E_{13}\phi_{,x_2} - F_{m_{11}}\ddot{u} &= f_u \\ A_{22}v_{,x_1x_1} + C_{22}v_{,x_2x_2} + B_{21}u_{,x_1x_2} + D_{23}\phi_{,x_1} - F_{m_{22}}\ddot{v} &= f_v \\ D_{32}v_{,x_1} + E_{31}u_{,x_2} + F_{33}\phi &= m_\phi \end{aligned} \tag{112}$$

which can be recognized as a set of differential equations governing the behavior of an equivalent 2D continuum in terms of horizontal and vertical displacements and one rotation. Under the assumption that no concentrated couples are applied to the nodes of the lattice, the rank of the system of equations can be reduced from three to two by solving for ϕ in the third equation and substituting in the first two. Performing the reduction yields the following set of equations

$$\begin{aligned} Au_{,xx} + Bu_{,yy} + Cv_{,xy} - F_{m_{11}}\ddot{u} &= f_u \\ Du_{,xx} + Eu_{,yy} + Fv_{,xy} - F_{m_{22}}\ddot{v} &= f_v \end{aligned} \tag{113}$$

where the new coefficients are expressed in terms of the entries of the matrices $A \dots F$ as:

$$\begin{aligned} A &= A_{11} \\ B &= C_{11} - E_{31}E_{13}/F_{33} \\ C &= B_{12} - D_{32}E_{13}/F_{33} \\ D &= A_{22} - D_{32}D_{23}/F_{33} \\ E &= C_{22} \\ F &= B_{21} - E31D_{23}F_{33} \end{aligned} \tag{114}$$

Equation (113) has the structure of a classical elasticity equation, where the coefficients are, in the most general case, different from each other.

3.3.3 Homogenized equations for the regular hexagonal lattice

Let us focus on the case of regular hexagonal lattice ($\theta = 30^o$, $\alpha = 1$). This geometry represents the most widespread honeycomb configuration, whose behavior is well known and abundantly documented in the literature. The relative simplicity of this case allows carrying out the homogenization process symbolically, which presents a few advantages. First, it provides homogenized equations in a form that is easy to compare with analytical solutions available in the literature. Second, it offers insight into the actual dependency of the coefficients of eq. (113) upon the geometric and material parameters of the original lattice. Lastly and most importantly, it shows the way for a correct normalization of the

derived equations of motion. The equations assume the form:

$$\begin{aligned}
&\tfrac{\sqrt{3}}{6}E\tfrac{\beta(1+3\beta^2)}{(1+\beta^2)}u_{,x_1x_1} + \tfrac{\sqrt{3}}{3}E\tfrac{\beta^3}{(1+\beta^2)}u_{,x_2x_2} + \tfrac{\sqrt{3}}{6}E\beta v_{,x_1x_2} - \tfrac{2}{\sqrt{3}}\rho\beta\ddot{u} = \tfrac{2f_u}{3\sqrt{3}L^2} \\
&\tfrac{\sqrt{3}}{3}E\tfrac{\beta^3}{(1+\beta^2)}v_{,x_1x_1} + \tfrac{\sqrt{3}}{6}E\tfrac{\beta(1+3\beta^2)}{(1+\beta^2)}v_{,x_2x_2} + \tfrac{\sqrt{3}}{6}E\beta u_{,x_1x_2} - \tfrac{2}{\sqrt{3}}\rho\beta\ddot{v} = \tfrac{2f_v}{3\sqrt{3}L^2}
\end{aligned} \tag{115}$$

It is useful recalling at this stage the concept of relative density $\bar{\rho}$ for a lattice, defined as the ratio between the mass of a unit cell and that of a portion of continuum occupying the same area of the unit cell. For regular hexagonal lattices, it can be easily shown that

$$\bar{\rho} = \frac{2}{\sqrt{3}}\beta \tag{116}$$

The right hand side of eq. (115) can be rearranged in order to highlight $\bar{\rho}$ as defined in eq. (116). This shows that, like for the square lattice previously described, the coefficients of the time derivatives in eq. (115) can be expressed as $\rho\bar{\rho}$, where the quantity $\rho^* = \rho\bar{\rho}$ is the effective density of the lattice. This result corresponds to a set of equations of motion expressed *per unit area*, consistently with the elastic terms in the left hand side. Direct comparison between the coefficients of the homogenized equations and the elasticity equations for the isotropic continuum, which assume the general following form

$$\begin{aligned}
&\tfrac{E}{(1-\nu^2)}u_{,x_1x_1} + Gu_{,x_2x_2} + \tfrac{E}{2(1-\nu)}v_{,x_1x_2} - \rho\ddot{u} = q_u \\
&Gv_{,x_1x_1} + \tfrac{E}{(1-\nu^2)}v_{,x_2x_2} + \tfrac{E}{2(1-\nu)}u_{,x_1x_2} - \rho\ddot{v} = q_v
\end{aligned} \tag{117}$$

allows the identification of equivalent mechanical properties for the regular hexagonal lattice. The equivalent moduli of elasticity and the equivalent Poisson's ratio can be expressed as:

$$E_h = \frac{4\sqrt{3}}{3}E\frac{\beta^3}{(1+3\beta^2)} \tag{118}$$

$$G_h = \frac{\sqrt{3}}{3}E\frac{\beta^3}{(1+\beta^2)} \tag{119}$$

$$\nu_h = \frac{1-\beta^2}{1+3\beta^2} \tag{120}$$

It can be noticed that, in the case of very slender beams ($\beta \ll 1$), these results approach in the limit the formulae available in the literature [26]

$$E_h = \frac{4\sqrt{3}}{3}E\beta^3 \tag{121}$$

$$G_h = \frac{\sqrt{3}}{3}E\beta^3 \tag{122}$$

Table 1: Elastic properties for regular hexagonal honeycomb ($\theta = 30^o$)

	Homogenization	Reference (G.&A.)	Error
$E\ \left[\frac{N}{m^2}\right]$	$2.0276\,\text{x}10^7$	$2.0496\,\text{x}10^7$	0.6 %
$G\ \left[\frac{N}{m^2}\right]$	$5.0942\,\text{x}10^6$	$5.1240\,\text{x}10^6$	1.1 %
ν	0.9987	1	1.0 %

$$\nu_h = 1 \tag{123}$$

This behavior can be explained by recalling that the expressions in [26] are obtained disregarding the effects of axial deformations, that is considering the axial stiffness of the beams in the lattice much higher than the flexural one. Since the ration between axial and flexural stiffness for a beam is defined as:

$$\frac{\frac{12EI}{L^3}}{\frac{EA}{L}} = \beta^2 \tag{124}$$

this condition corresponds in fact to the limit $\beta \ll 1$ used for eq.s (121), (122) and (123). The expressions obtained by application of the homogenization approach account for the effects of axial deformation in the beams and show that the Poisson's ratio cannot exactly assume the value 1, for which the first coefficients in the equivalent continuum become indeterminate, but tends to 1 in the limit. Numerical results for E, G and ν obtained through the homogenization method and from the formulae in [26] for $\theta = 30^o$, $\alpha = 1$ and $\beta = 0.05$ are compared in Table 1.

3.3.4 Identification of mechanical properties for a generic configuration

The technique is then applied to hexagonal lattices with varying internal angle θ. For angles $\neq 30^o$ the homogenized equations assume the form of eq. (125)

$$\begin{aligned} a u_{,x_1x_1} + d u_{,x_2x_2} + (c+d) v_{,x_1x_2} - \rho^* \ddot{u} = q_u \\ d v_{,x_1x_1} + b v_{,x_2x_2} + (c+d) u_{,x_1x_2} - \rho^* \ddot{v} = q_v \end{aligned} \tag{125}$$

where the coefficients $a \ldots d$ in front of the differential operators and the equivalent density ρ^* are functions of the geometric and material properties of the beams constituting the unit cell. It is worth recalling that eq. (125) constitutes an approximation of the exact

behavior of the lattice in which all terms $\mathcal{O}(\epsilon^3)$ have been neglected. Direct comparison between the coefficients of the homogenized equations and the elasticity equations for the orthotropic continuum can be used to estimate the elastic properties. The results for E_1, E_2, G_{12}, ν_{12} and ν_{21} are plotted for a variety of internal angles in fig. 42 for lattices with $L = 1$, $\alpha = 1$ and $\beta = 1/15$. In fig. 42 both traditional ($\theta > 0^o$) and auxetic ($\theta < 0^o$) configurations are considered, as well as the critical case of $\theta = 0^o$. The values obtained using the formulae in Gibson & Ashby (G.&A.) are superimposed. It can be noticed that, while the accuracy can be considered overall satisfactory, only E_2, G_{12} and ν_{21} feature good agreement for all θs. For E_1 and ν_{12} a discrepancy between the two predictions is observed for $|\theta| < 5^o$ and becomes dramatic in the neighborhood of $\theta = 0^o$ where G.&A. formulae predict ∞ values. The reason for this discrepancy lies in the different beam model used for the two formulations, as stated above. The formulation by G.&A. neglects the axial deformability of the beams and presents a shortcoming at $\theta = 0^o$, where the $E_1 \gg E_2$ is definitely expected but $E_1 \to \infty$ is clearly not acceptable from a physical stand point. The discrepancy is naturally as pronounced as the the slenderness ratio β is small. In fig. 43 a comparison is shown with G.&A. formulae including axial and shear effects. This correction including axial terms produces now an excellent agreement in the curves even for small θ, although $\theta = 0^o$ is still captured correctly by the homogenization method only. The remaining differences between the formulations are believed to be responsible for the slight disagreement observed for ν_{12} and ν_{21} for larger values of θ.

3.4 Wave Propagation in Hexagonal Lattices

In the next step of the work, the propagation of waves in hexagonal honeycombs is considered and the performance of the homogenization method at approximating the wave propagation characteristics is estimated. The first motivation for this analysis lies in the need to further investigate the range of validity of the homogenized equations: in this sense, the level of approximation observed for the wave characteristics is used as an additional metric for the quality of the homogenization technique. From an applicative stand point, wave propagation analysis also shows some interesting and unique dynamic behavior of auxetic lattices.

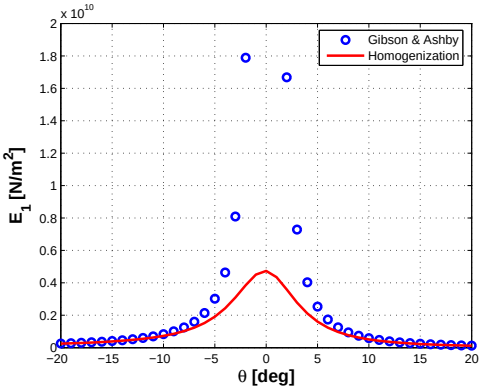

(a) Young's modulus E_1

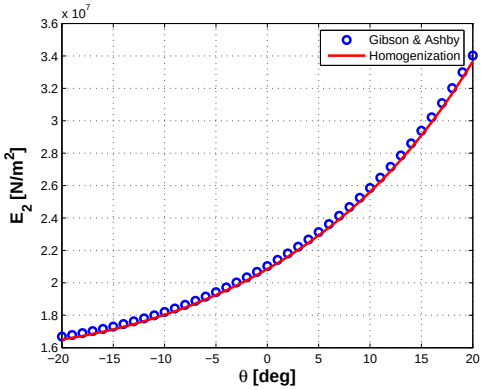

(b) Young's modulus E_2

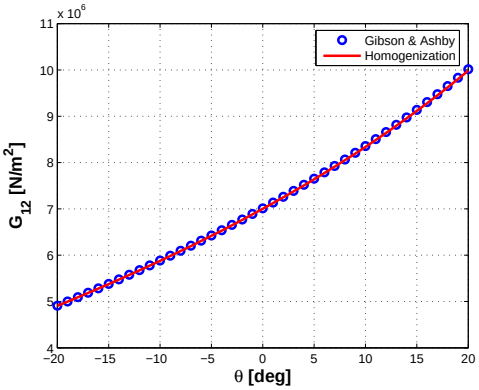

(c) Shear modulus G_{12}

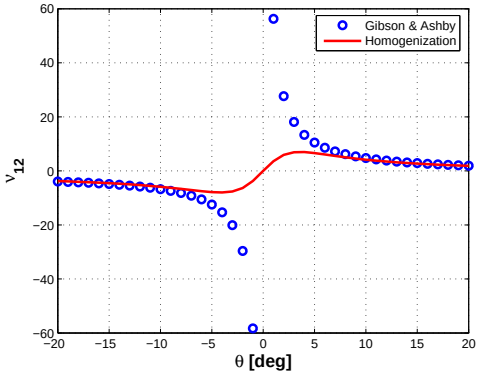

(d) Poisson's ratio ν_{12}

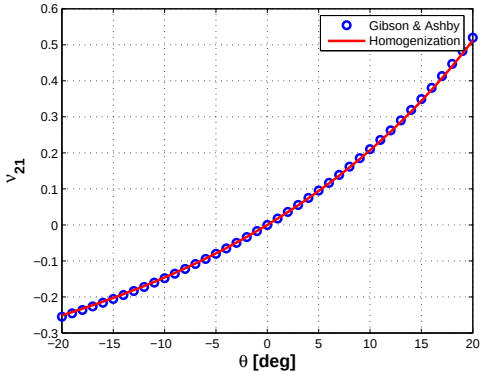

(e) Poisson's ratio ν_{21}

Figure 42: Comparison of homogenized quantities with reference values for different configurations

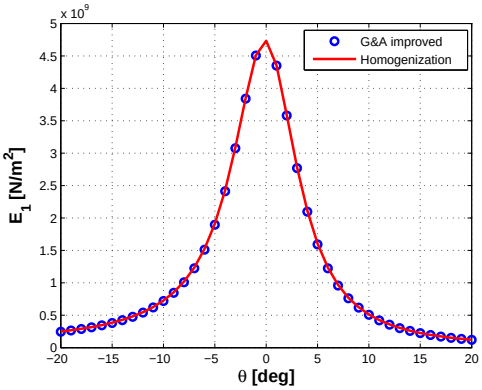

(a) Young's modulus E_1

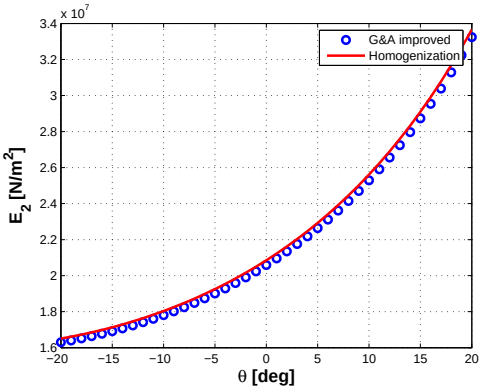

(b) Young's modulus E_2

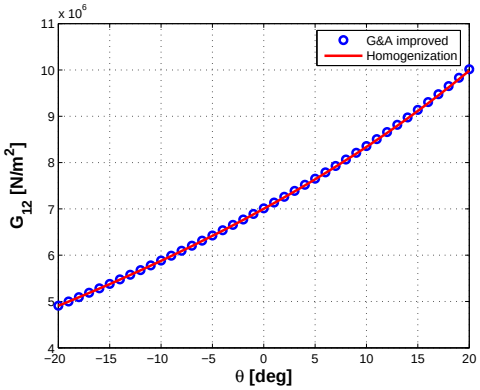

(c) Shear modulus G_{12}

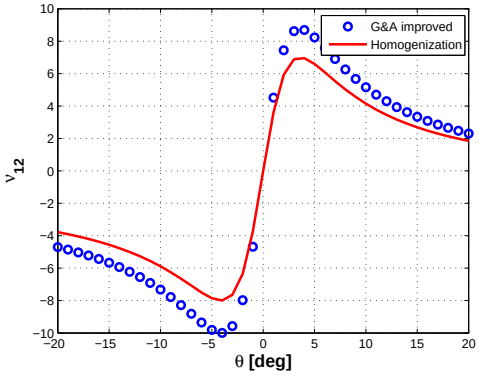

(d) Poisson's ratio ν_{12}

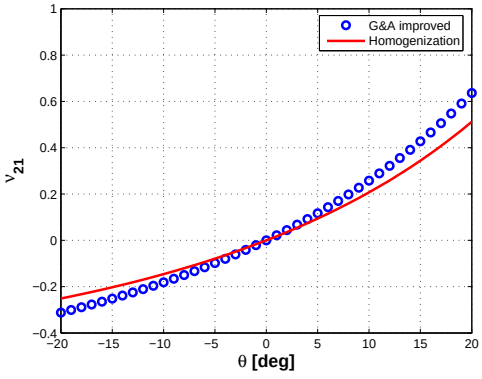

(e) Poisson's ratio ν_{21}

Figure 43: Comparison of homogenized quantities with refined reference values for different configurations

3.4.1 Bloch's Theorem

Wave propagation in systems of the kind depicted in fig. 39 is traditionally studied through the application of Bloch's theorem. The displacement $\mathbf{w}$ of a point P of the reference unit cell corresponding to a wave propagating at frequency ω can be expressed as:

$$\mathbf{w}(\mathbf{r}_P) = \mathbf{w}_{P_0} e^{i\omega t - \mathbf{k}\cdot\mathbf{r}_P} \tag{126}$$

where $\mathbf{w}_{P_0}$ is the wave amplitude, and $\mathbf{k}$ is the wave vector. According to Bloch's theorem, the displacement of the point corresponding to P in the cell at location $\boldsymbol{\rho}_p(n_1, n_2)$ can be written in terms of the displacement of the reference unit cell as follows:

$$\begin{aligned} \mathbf{w}(\boldsymbol{\rho}_P) &= \mathbf{w}(\mathbf{r}_P) e^{\mathbf{k}\cdot(\boldsymbol{\rho}_P - \mathbf{r}_P)} \\ &= \mathbf{w}(\mathbf{r}_P) e^{n_1 k_1 + n_2 k_2} \end{aligned} \tag{127}$$

where $k_i = \mathbf{k}\cdot\mathbf{e}_i$ with $i = 1, 2$. Bloch's theorem states that the proportionate change in wave amplitude occurring from cell to cell does not depend on the cell location within the periodic system. Accordingly, the wave propagation characteristics of a periodic assembly of the kind considered in this work can be fully identified through the analysis of the reference unit cell. In eq. (127), $k_i = \delta_i + i\epsilon_i$ $(i = 1, 2)$ is a complex number, whose real part δ_i defines the amplitude attenuation as a wave propagates from one cell to the next, while the imaginary part ϵ_i defines the change of phase across each cell. For this reason, it is often called *phase constant*. In the analysis of wave propagation without amplitude attenuation, δ_i is typically set to 0, while the phase constants ϵ_1, ϵ_2 are varied to investigate their dependency upon frequency. The space defined by the lattice vector basis $\mathcal{E} = (\mathbf{e}_1, \mathbf{e}_2)$ is denoted as the *direct lattice*. Given a direct lattice space, one may define a reciprocal lattice space, which is described by a basis $\mathcal{B} = (\mathbf{b}_1, \mathbf{b}_2)$, whose basis vectors are given by:

$$\mathbf{b}_i \cdot \mathbf{e}_j = \delta_{ij} \tag{128}$$

where δ_{ij} is the Kronecker delta. The reciprocal lattice vectors for the hexagonal lattices under consideration are given by:

$$\begin{aligned} \mathbf{b}_1 &= \frac{1}{2L\cos\theta}\mathbf{i}_1 + \frac{1}{2\left(H + L\sin\theta\right)}\mathbf{i}_2 \\ \mathbf{b}_1 &= \frac{1}{2L\cos\theta}\mathbf{i}_1 + \frac{1}{2\left(H + L\sin\theta\right)}\mathbf{i}_2 \end{aligned} \tag{129}$$

$$\tag{130}$$

In the reciprocal lattice, the wave vector $\mathbf{k} = 2\pi\boldsymbol{\lambda}$ can be expressed as:

$$\mathbf{k} = k_1\mathbf{b}_1 + k_2\mathbf{b}_2 \tag{131}$$

so that, according to the definition of reciprocal lattice given in eq. (128):

$$\mathbf{k}\cdot\mathbf{e}_1 = k_1 \tag{132}$$

While the direct lattice defines the spatial periodicity of the considered domain, the reciprocal lattice describes the periodicity of the frequency/wavenumber relation. This can be easily demonstrated by replacing $\boldsymbol{\lambda}$, where $\mathbf{k} = 2\pi\boldsymbol{\lambda}$, with $\boldsymbol{\lambda}' = \boldsymbol{\lambda} + m_1\mathbf{b}_1 + m_2\mathbf{b}_2$ in eq. (127), with m_1, m_2 integers. This gives:

$$\boldsymbol{w}(\boldsymbol{\rho}_p) = \boldsymbol{w}(\boldsymbol{r}_p)e^{n_1k_1' + n_2k_2'}$$

where

$$k_i' = 2\pi\boldsymbol{\lambda}'\cdot\boldsymbol{e}_i = k_i + 2\pi m_i, \quad i = 1, 2 \tag{133}$$

which shows that the wavenumber in a two-dimensional lattice is a periodic function of the wave vector $2\pi\lambda$ in the reciprocal lattice. Hence, full representation of the dependency of the wave vector upon the wave propagation frequency is obtained by investigating its variation over a single period. In a two-dimensional lattice, the period corresponds to a region in the reciprocal lattice whose area equals the area of the reciprocal lattice's unit cell. The procedure for the identification of the area corresponding to the period, also known as *First Brillouin Zone*, is described in [10]. Examples of first Brillouin zones for a regular hexagonal lattice and for a re-entrant lattice are presented in the following section.

3.4.2 Dispersion relations

The behavior of the unit cell of the periodic domain can be conveniently described through a discretized equation of motion and by defining the cell's interaction with its neighbors (fig. 44). The unit cell is modeled as an assembly of rigidly connected beams. Application

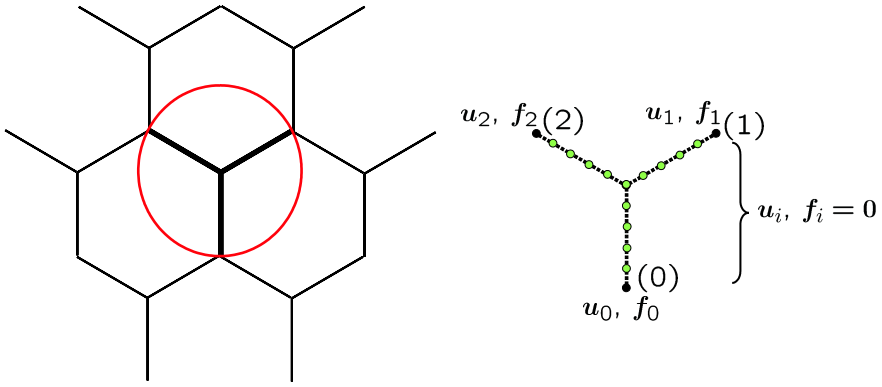

Figure 44: Unit cell degrees of freedom and interaction with neighboring cells

of standard Finite Element procedure yields the unit cell's equation of motion, which can be expressed as:

$$\Big(\mathbf{K} - \omega^2 \mathbf{M}\Big)\boldsymbol{u} = \mathbf{f} \tag{134}$$

where ω is the frequency of wave propagation, $\mathbf{K}$ and $\mathbf{M}$ are the assembled mass and stiffness matrices for the cell, while $\mathbf{u}$, $\mathbf{f}$ are respectively the vectors containing generalized nodal displacements and forces of interaction of the cell with its neighbors (see fig. 44):

$$\begin{aligned} \mathbf{u} &= \{\ \mathbf{u}_0 \quad \mathbf{u}_1 \quad \mathbf{u}_2 \quad \mathbf{u}_i\ \}^T \\ \boldsymbol{f} &= \{\ \mathbf{f}_0 \quad \mathbf{f}_1 \quad \mathbf{f}_2 \quad 0\ \}^T \end{aligned} \tag{135}$$

In eq. (127) the subscripts $0, 1, 2$ follow the notation described in fig. 44, while subscript i denotes the degrees of freedom of nodes that are internal to the cell. Eq. (135) is also based on the assumption that no external forces are applied and that only internal interaction forces with neighboring cells appear in the cell's equation of motion. The absence of forces on the internal nodes facilitates the condensation of the internal degrees of freedom, which yields a significant reduction in the size of the problem.

The application of Bloch's theorem yields the following eigenvalue problem:

$$\left[\mathbf{K}_r(k_1,k_2) - \omega^2 \mathbf{M}_r(k_1,k_2)\right] \mathbf{u}_r = \mathbf{0} \tag{136}$$

where $\mathbf{K}_r(k_1,k_2),\ \mathbf{M}_r(k_1,k_2)$ are reduced stiffness and mass matrices according to eq. [ref]. The solution of eq. (136) defines the dispersion characteristics of the lattice, which are found by imposing two of the three unknowns k_1, k_2, ω, and solving for the third. Typically, wave motion without attenuation is investigated. For this reason, k_1, k_2 are generally imposed as imaginary numbers $k_1 = i\epsilon_1, \quad k_2 = i\epsilon_2$ which vary within the first Brillouin zone. The solution of the eigenvalue problem yields the frequency of wave propagation corresponding to the assigned pair k_1, k_2. The complete solution obtained for varying k_1, k_2 is a surface denoted as *phase constant surface* or *dispersion surface*, which can be expressed as:

$$\omega = \omega(k_1,k_2) \tag{137}$$

The number of surfaces obtained corresponds to the dimension of the eigenvalue problem in eq. (136). Each surface describes the wavenumber/frequency relation for each wave mode characterizing wave propagation in the considered medium. The computational cost of the evaluation of the dispersion diagrams can be significantly reduced by exploiting the symmetry of the first Brillouin zone, which is related to the symmetry of the unit cell. As a result, smaller regions of variation for the phase constants can be identified. Such regions are denote as *Irreducible Brillouin zones*. In addition, information regarding propagation in specific directions, or on the presence of frequency gaps between consecutive phase constant surfaces can be obtained by letting the wave vector vary only along the contour of the irreducible zone. Examples of irreducible zones and various possible representations of the dispersion diagrams are presented in what follows.

The contours of the first two branches of the dispersion surfaces for hexagonal lattices with $\alpha = 1$, $\beta = 1/15$ and varying internal angles (specifically $\theta = 30^o, 10^o, 0, -10^o$) are shown respectively in fig.s 45 and 46. The dispersion surfaces, plotted with respect to k_1, k_2, clearly show the periodicity of the dispersion relations, which is highlighted by superimposing the boundaries of the first Brillouin zone to the contour lines. Some marked

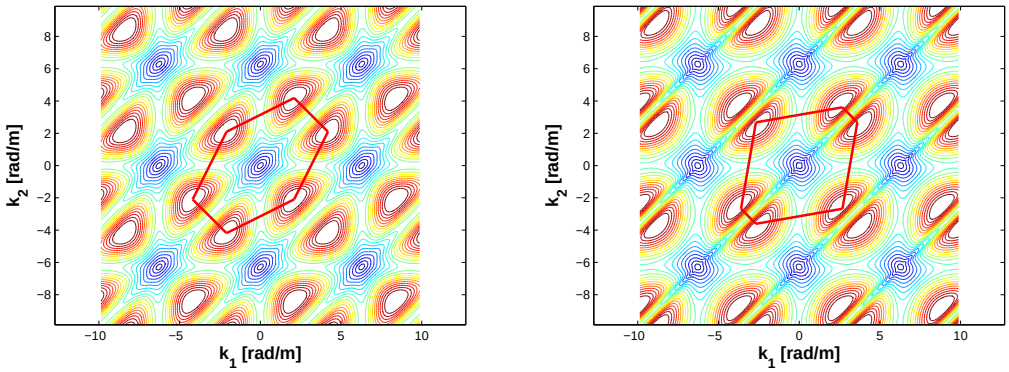

(a) $\theta = 30^o$

(b) $\theta = 10^o$

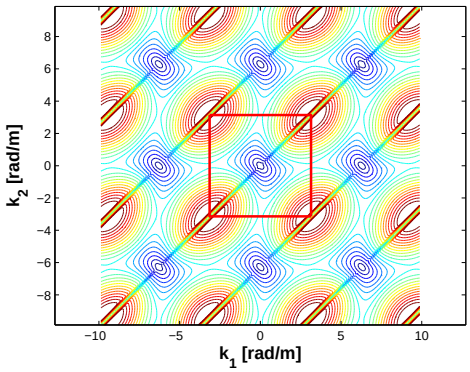

(c) $\theta = 0^o$

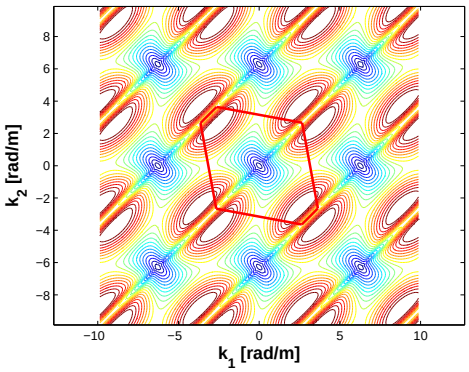

(d) $\theta = -10^o$

Figure 45: Dispersion surfaces for various lattice configurations: 1^{st} mode

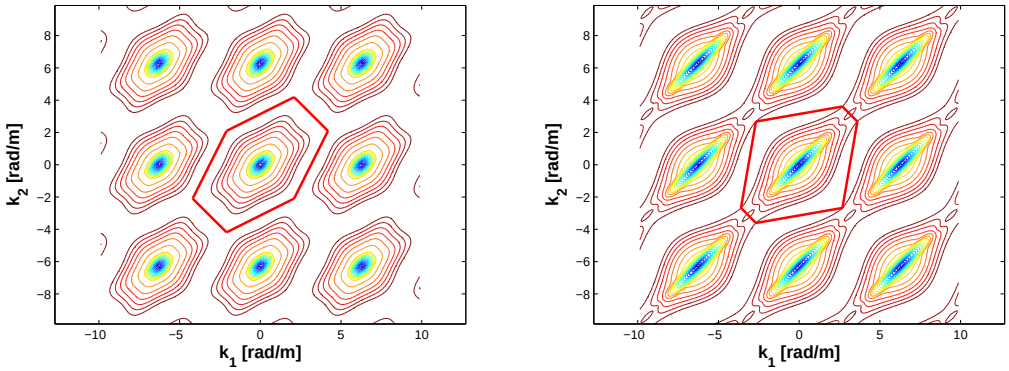

(a) $\theta = 30^o$

(b) $\theta = 10^o$

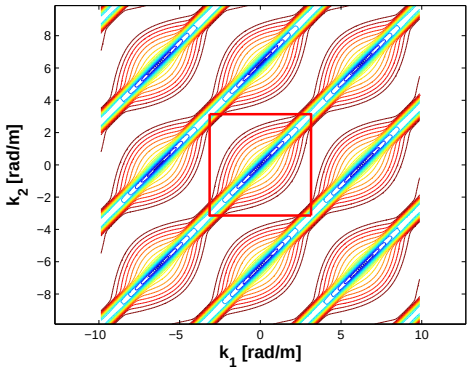

(c) $\theta = 0^o$

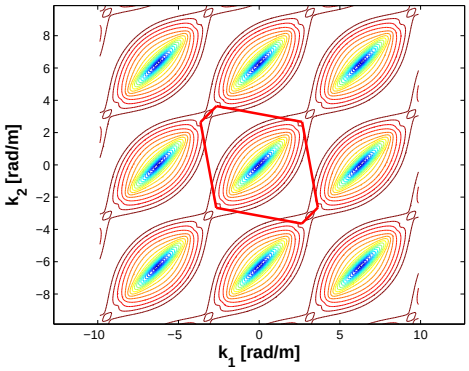

(d) $\theta = -10^o$

Figure 46: Dispersion surfaces for various lattice configurations: 2^{nd} mode

differences between the lattices with different internal angles can be observed, which suggest differences in their wave propagation characteristics. Such differences can be better observed by considering the contour plots of the dispersion surfaces plotted over a smaller range of the wave vectors. Also, representation in terms of the components of the wave vector in the physical space allows easier interpretation of the results. Such components are denoted as ξ_1, ξ_2. Figure 47 shows contours of the first mode of the dispersion relations

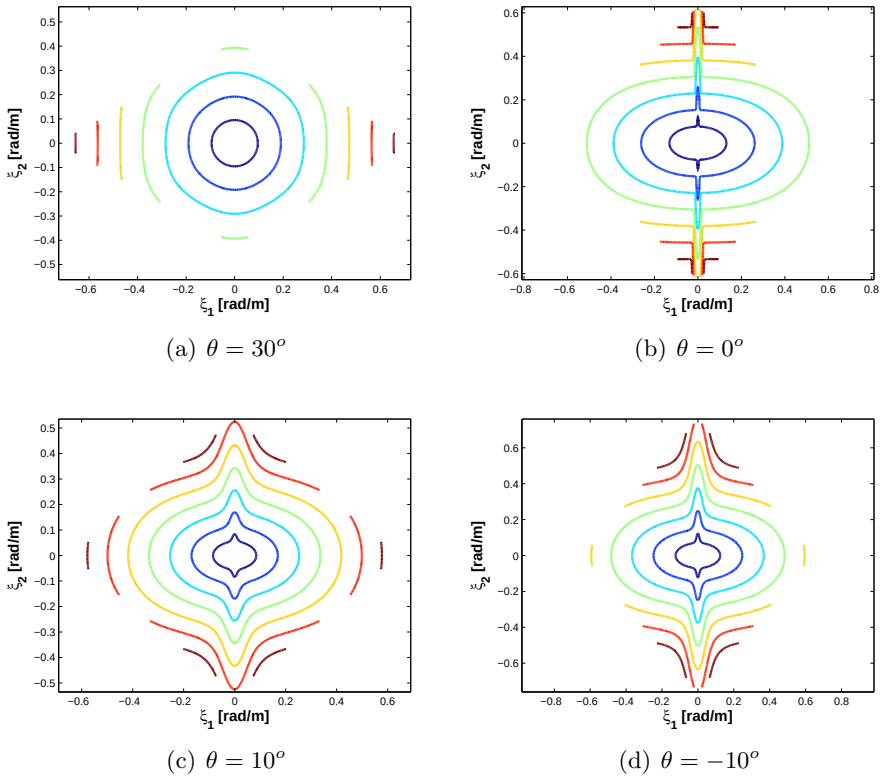

(a) $\theta = 30^o$ (b) $\theta = 0^o$

(c) $\theta = 10^o$ (d) $\theta = -10^o$

Figure 47: Detail of low frequency of the 1^{st} mode of the dispersion surfaces for various lattice configurations.

corresponding to the low frequency/long wavelength behavior of the lattice. The circular contours for the regular hexagonal lattice ($\theta = 30^o$) suggest its isotropic behavior within the corresponding frequency range, while non regular hexagonal geometries feature lobed isofrequency contours which indicate anisotropy even at low frequencies. Negative internal angles seem to produce a more accentuated lobe if compared with same values of positive internal angle. In addition, the lobe becomes very narrow for $\theta = 0^o$. Such differences

between the dispersion characteristics of the various lattices can be also highlighted by the analysis of the wave velocities, which is presented in the following sections.

3.4.3 Band structure

A convenient and compact representation of the dispersion relations for the considered two-dimensional domains is obtained by varying the wave vector along the contour of the first Brillouin zone. For practical purposes, the symmetry of the First Zone can be exploited to

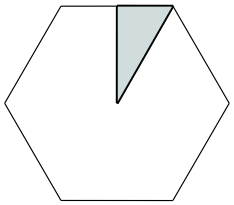

Figure 48: First Brillouin Zone for a regular hexagonal lattice.

limit the variation of the wave vector along the irreducible zone, which can be defined as the smallest area allowing full representation of the $\omega = \omega(k_1, k_2)$ variation. The resulting rep-

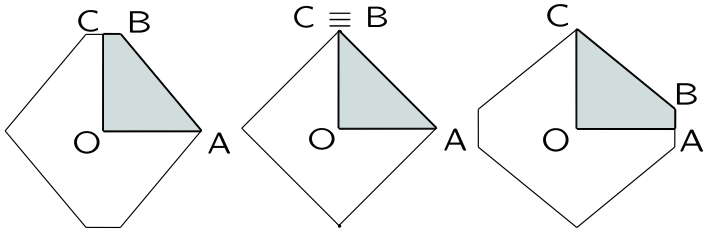

(a) $\theta > 0$ (b) $\theta = 0$ (c) $\theta < 0$

Figure 49: Variation of First Brillouin Zone with internal angle.

resentation clearly shows the mode structure for the domain, and the presence of interesting wave phenomena such as for example mode veering and bandgaps [80]. The results shown in fig.s 45 and 46 show that the shape of the first Brillouin zone changes with the value of the internal angle. In particular, a marked difference occurs between lattices with positive and negative internal angles, with the case for $\theta = 0$ showing a peculiar quadrilateral shape, as opposed to the hexagonal areas characterizing all the other lattices. The irreducible zone and associated contour also change with the internal angle, and it is in general larger than

the one that can be selected in lattices with regular hexagonal geometry [80] (see fig. 48). The first Brillouin zone for lattices with positive and negative internal angles are shown in fig. 49, where the contours of the irreducible zones considered for the subsequent analysis are also highlighted as shaded areas. The Brillouin zones are here represented in the physical wavenumber space ξ_1, ξ_2.

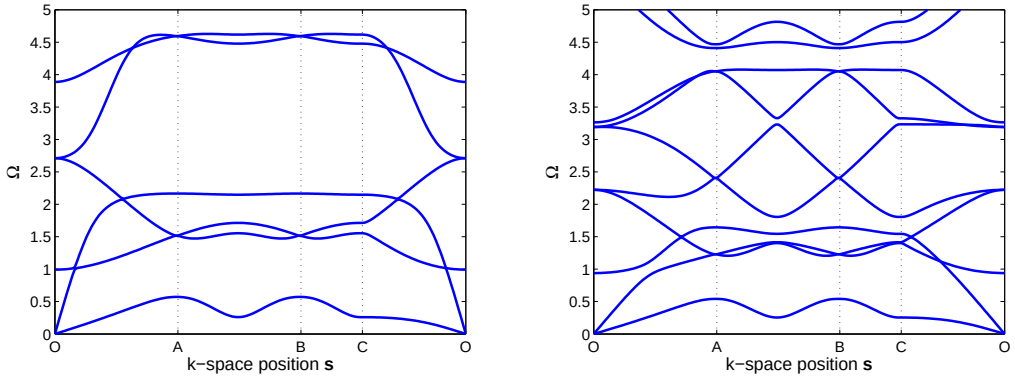

(a) $\beta = 1/15$ (b) $\beta = 1/5$

Figure 50: Band structure for lattices with $\theta = 30^o$ and $\alpha = 1$.

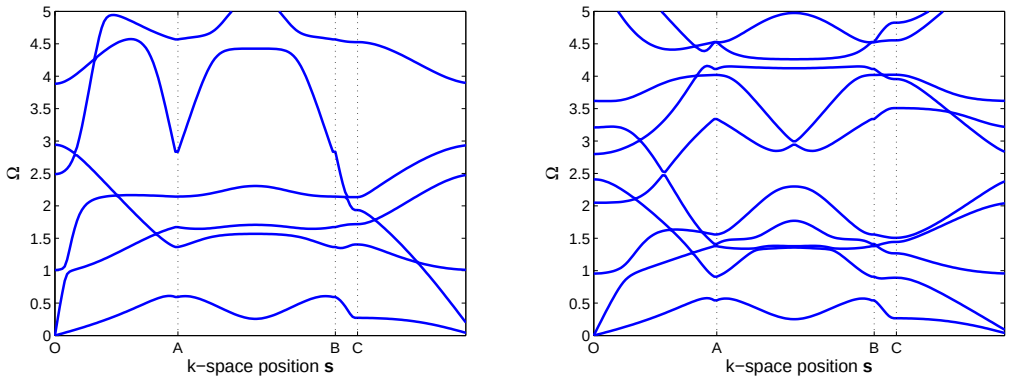

(a) $\beta = 1/15$ (b) $\beta = 1/5$

Figure 51: Band structure for lattices with $\theta = 10^o$ and $\alpha = 1$.

Examples of band structure for several lattice configurations are shown in fig.s 50 through 52, where the frequency axis is normalized with respect to the flexural resonance of a simply supported lattice beam of length L, so that:

$$\Omega = \omega \frac{L^2}{\pi^2} \sqrt{\frac{\rho h}{EI}} \tag{138}$$

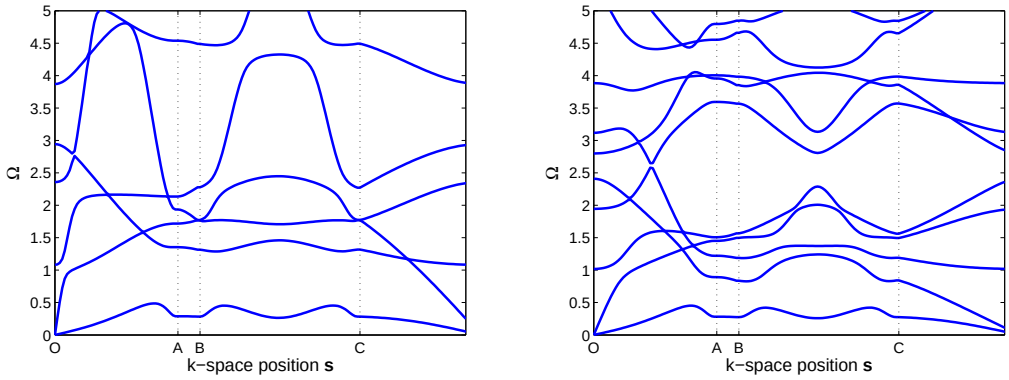

(a) $\beta = 1/15$ (b) $\beta = 1/5$

Figure 52: Band structure for lattices with $\theta = -10^o$ and $\alpha = 1$.

with ω denoting the frequency corresponding to the assigned wavenumber, E, ρ, I the material and inertia properties of the lattice beams and t the considered wall thickness shown in fig. 40. Figure 50 shows how the dispersion characteristics of a regular hexagonal lattice are influenced by the slenderness ration $\beta = t/L$. In the considered frequency range, the lattice with $\beta = 1/15$ features a band gap for $\Omega > 5$, and the presence of veering of the branches at several locations. Veering consists in two branches coming infinitely close without crossing or touching, and it is a common phenomenon found in the solution of eigenvalue problems containing weakly coupled systems [69, 65]. Changing the slenderness ratio of the lattices causes a general increase in the modal density in the considered range of frequencies, and a significant alteration of the band structure. However, it is interesting to observe how the lower branch remains virtually unaffected. The veering found between the $O \rightarrow A$ segment of the diagram for $\beta = 1/15$ disappears with the higher value of β as the two branches clearly separate. Similar observations can be made from the comparison of the band structures of lattices with $\theta = 10^o$ and $\theta = -10^o$, respectively shown in fig.s 51 and 52. In both cases, there is a noticeable absence of bandgaps, with the exception of a small gap at approximately $\Omega = 4.25$ for $\theta = 10, \beta = 1/5$, and a general asymmetry of the diagrams which sets them apart from the ones of the regular hexagonal lattice.

The band structure can be used to check the error introduced by the condensation of the internal degrees freedom as explained above in the chapter. The band structure with and

without condensation is shown in fig. 53, where the hexagonal lattice with $\theta = 30^o$ is used as reference example. Figure 53.a highlights some of the limitations of the condensation process: first, since the unit cell analysis is now conducted in terms of the degrees of freedom of the sole bottom node of the cell, only the first three propagation modes can be recovered; second, the agreement with the exact analysis is limited to the first and part of the second mode. However, in the low-frequency range, where the homogenization is expected to be accurate, the agreement is acceptable, as shown in fig. 53.b and the error introduced by the static condensation is expected to be negligible.

3.4.4 Phase velocities for the lattice

The dispersion surfaces can be used to estimate the variation of the phase velocity in terms of frequency and direction of wave propagation. The phase velocity in a direction defined by the wave vector:

$$\mathbf{k} = k_1\mathbf{b}_1 + k_2\mathbf{b}_2 \tag{139}$$

$$\mathbf{k} = \xi_1\mathbf{i}_1 + \xi_2\mathbf{i}_2 \tag{140}$$

and at a given frequency ω can be expressed as:

$$\mathbf{c}_{ph} = \frac{\omega}{k}\mathbf{u} \tag{141}$$

where $k = |\mathbf{k}|$ and $\mathbf{u}$ is a unit vector in the direction of the wave vector $\mathbf{u} = \frac{\mathbf{k}}{k}$. The evaluation of the phase velocity is performed by selecting the wave numbers corresponding to the dispersion surfaces at the desired frequency value. The angular range spanned by the corresponding set of wavenumbers is then computed to obtain the variation of the phase velocity in terms of the direction of wave propagation. For a non-dispersive, homogeneous medium, this operation yields a circle whose radius is independent of frequency. The same information is commonly presented in the form of slowness curves, which correspond to the inverse of the phase velocity. For the following examples, however, it was chosen to directly represent variations in terms of direction of wave propagation and frequency. Such variations can also be directly observed from the simulation of wave propagation within the cellular domain. The evaluation of phase velocities allows determining the dispersive

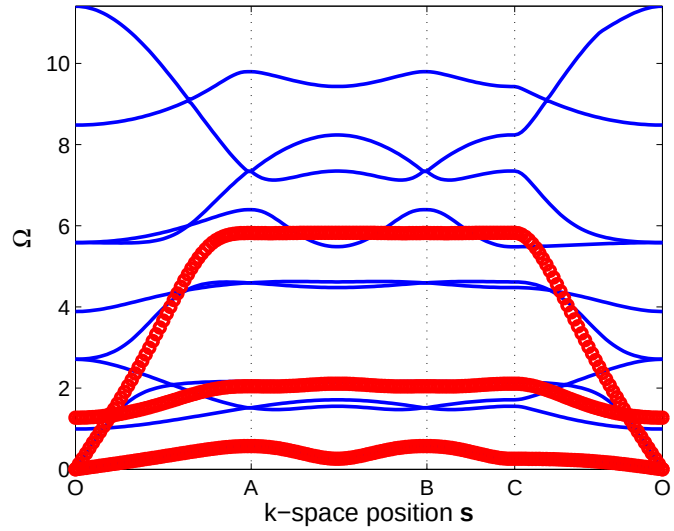

(a) Band structure

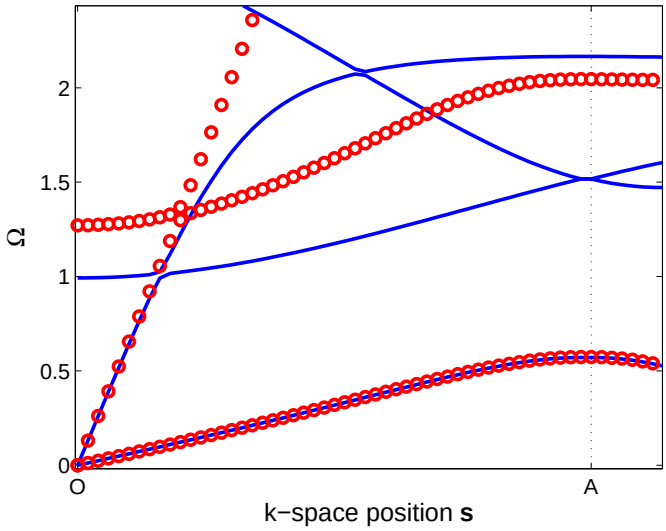

(b) Low-frequency region of agreement

Figure 53: Comparison between dispersion relations curves with and without static condensation (without condensation: solid line, with condensation: 'o')

behavior of the lattice, highlighted by the frequency dependency of the phase velocity, and the anisotropy of the domain in the wave propagation plane.

The phase velocities for various lattice configurations are computed according to the procedure described in the previous sections. Such evaluations highlight the non-isotropic behavior of the lattices, as well as their dispersive characteristics. In what follows, results are presented for phase velocities corresponding to the first two branches of the dispersion diagrams of the lattice. For convenience, and in analogy with the behavior of a homogeneous solid, the modes corresponding to the lowest two branches are here respectively denoted as shear (S-mode) and longitudinal (P-mode). The angular variation of the S-mode velocity and of the P-mode velocity is shown respectively in fig.s 54, 55. Figure 54 compares the velocity variations for the shear mode for three values of the internal angle ($\theta = 30^o, 10^o, -10^o$) and $\alpha = 1, \beta = 1/15$ at increasing values of frequency. The regular hexagonal honeycomb behaves as an isotropic solid at low frequencies, as indicated by the corresponding circular velocity curve. It is interesting to observe also that the low-frequency behavior of the lattice appears as non-dispersive as the velocity curves at different frequencies overlap almost exactly. The non-isotropic behavior of the lattice appears evident from the curve at $\Omega = 0.2$ which reproduces the six-fold, hexagonal symmetry of the lattice. The anisotropic behavior of the non-regular hexagonal lattices can be clearly observed from the variation of the phase velocity shown in fig. 54.b,c, which also highlight the presence of a frequency range where the phase velocity is not dependent on frequency. Similar considerations can be made from the analysis of the phase velocity curves for the longitudinal mode (fig. 55), which appears to show a non-dispersive behavior over a broader frequency range, as indicated also by the linear variation of the corresponding branch shown in the band structure diagrams. The anisotropic characteristics of the non-regular hexagonal lattices is also markedly visible, with a clear difference between the velocities along the horizontal and vertical direction. A summary of the these conclusions is provided in fig. 56, which shows the variation with frequency of the velocities along the vertical and horizontal directions (x, y). Figure 56.a compares the variation of the shear mode, with the ordinate axis being normalized with respect to the velocity of the hexagonal lattice, here denoted as $C_{S_{30}}$. The plot clear shows

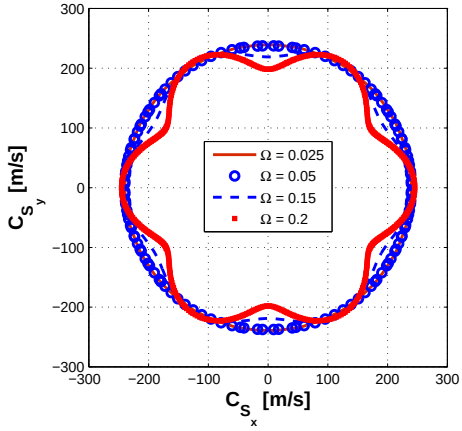

(a) $\theta = 30^o$

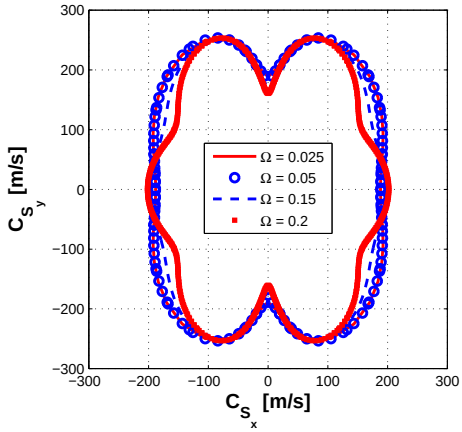

(b) $\theta = 10^o$

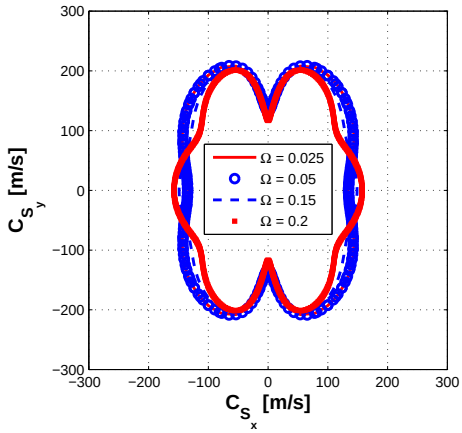

(c) $\theta = -10^o$

Figure 54: Phase velocity for shear like mode in various lattices.

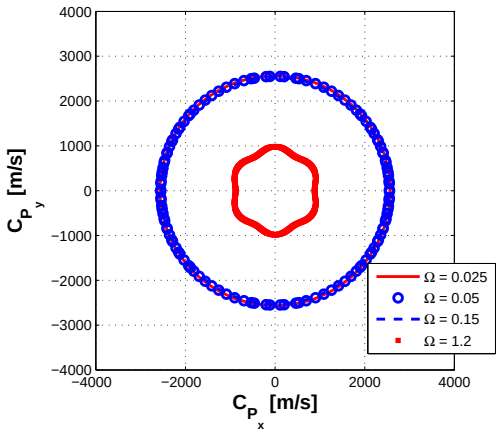

(a) $\theta = 30^o$

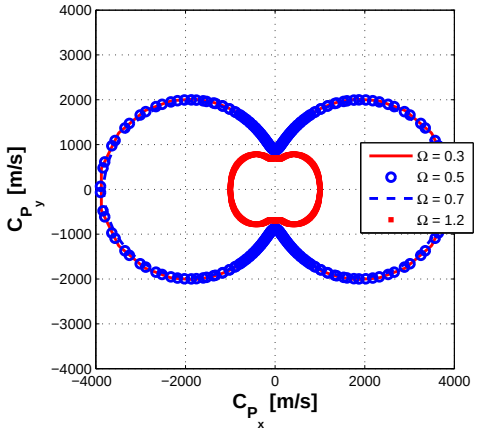

(b) $\theta = 10^o$

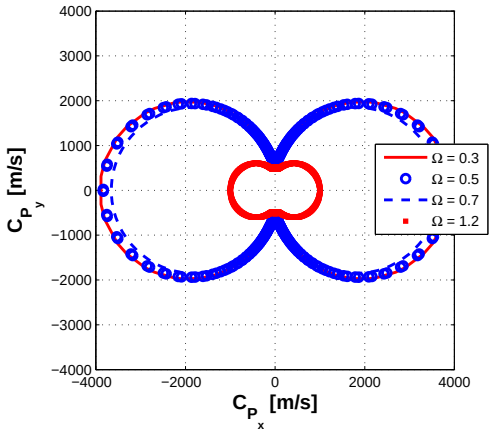

(c) $\theta = -10^o$

Figure 55: Phase velocity for longitudinal mode in various lattices.

how the velocity in the x and y directions respectively increase and decrease with frequency, and how they coincide in the low frequency range, where isotropic behavior is observed. Not only is the velocity of the shear mode lower in non-regular hexagonal lattices as compared to the one of the regular lattice, but also a considerable difference in phase velocity is observed between positive and negative angles. Moreover, the direction of propagation along y seems to show a more accentuated dispersive behavior than the one along x. The variation of the P-mode versus frequency (fig. 56.b) shows that the velocities in both directions remain constant over a large frequency range, and that at low frequencies they coincide with the case of the regular lattice.

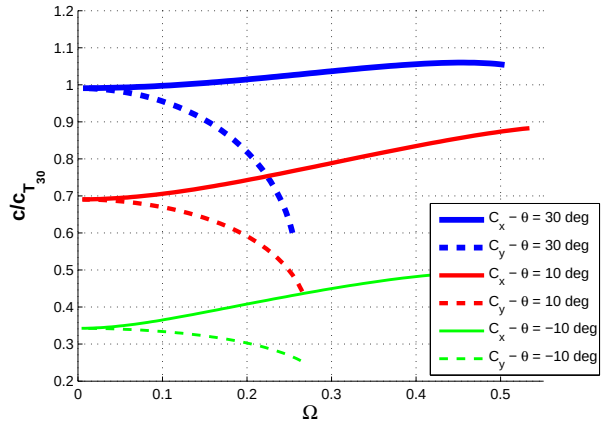

(a) S-Mode

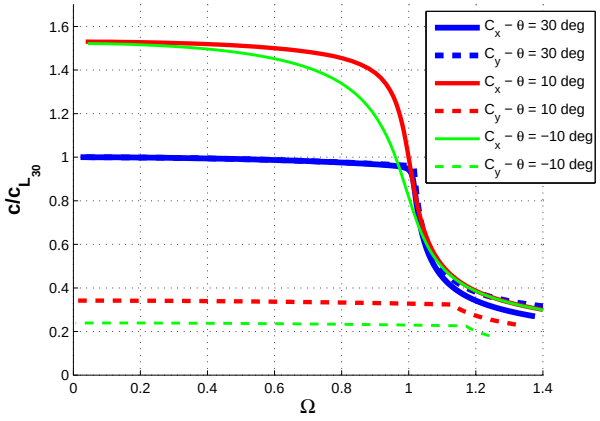

(b) P-Mode

Figure 56: Variation of components of phase velocity versus frequency.

3.4.5 Comparison with analysis from homogenized media

Approximate wave velocities can be obtained for hexagonal lattices following the same procedure presented above for the square lattice example. The parametric dependence of c_{ph} upon the direction of wave propagation γ is shown in fig. 57 for the regular hexagonal configuration ($\theta = 30^o$, $\alpha = 1$) as solid lines. The curves obtained with an exact analysis conducted on the unit cell are superimposed showing a perfect agreement of the homogenized quantities with the reference values. Inspection of fig. 57 suggests that the calculated wave speeds do not depend upon γ for either mode of propagation. The absence of directionality confirms the notion of isotropy for this class of lattices.

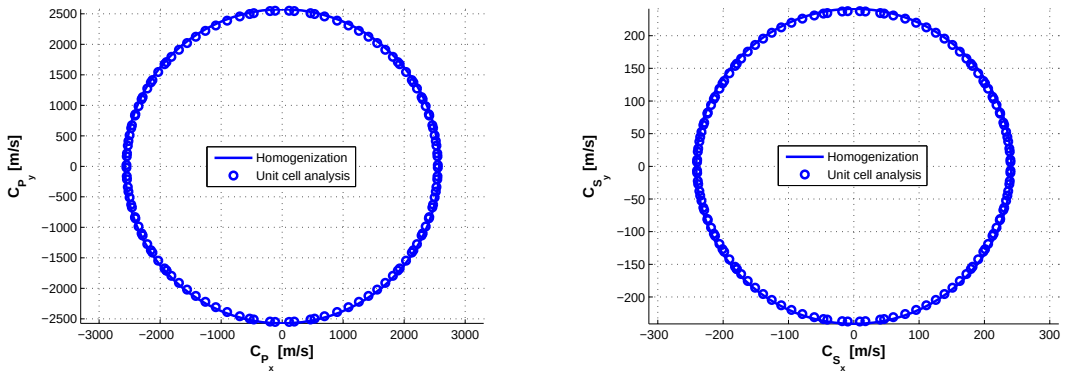

(a) P-mode (b) S-mode

Figure 57: Comparison between homogenized and exact wave velocities for $\theta = 30^o$

Let us now use the general wave equations of eq. (113) to explore the directionality of honeycombs with different configurations angles in the low-frequency regime. For the sake of consistency with the exact analysis previously exposed, let us focus our attention on the cases with $\theta = 30^o$ (fig. 58.a), $\theta = 10^o$ (fig. 58.b), $\theta = 0\,\text{deg}$ (fig. 58.c) and $\theta = -10^o$ (fig. 58.d). The generality of eq. (113), where the differences between the configurations are accounted for in the assembly of matrices $A \ldots F$, allows exploring all the configurations within a common framework. The calculated wave speeds for the considered values of θ are plotted in fig. 59. Figure 59 offers some insight in the different properties of this class of honeycombs like anisotropy and directionality. Figure 59.a is of particular interest because it shows behaviors that can be easily explained in light of simple geometric considerations

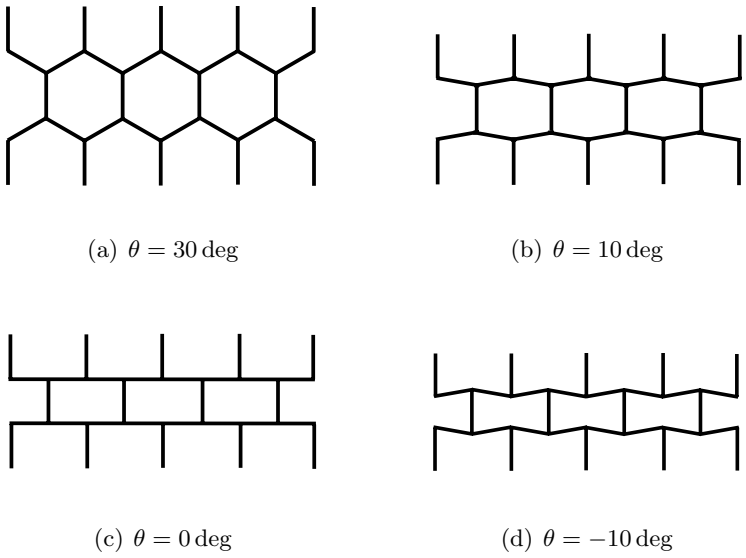

(a) $\theta = 30\,\text{deg}$ (b) $\theta = 10\,\text{deg}$

(c) $\theta = 0\,\text{deg}$ (d) $\theta = -10\,\text{deg}$

Figure 58: Different configurations for hexagonal honeycombs

made on the schematics of fig. 58. The behavior of the $\theta = 30^o$ lattice has already been discussed. Figure 59.a confirms that $\theta = 30^o$ is the only configuration for which isotropic non-directional behavior is observed. In all other cases the behavior of the lattice is strongly directional and the directionality increases as θ moves away from 30^o. The most directional behavior and the maximum value of c_{P_x} is encountered for $\theta = 0^o$, which corresponds to the case where the honeycomb degenerates into the lattice of fig. 58.c. This result can be explained in virtue of the presence of long uninterrupted beams aligned along the x directions that act like straight wave guides for pressure waves propagating along the horizontal direction. At the same time, the $\theta = 0^o$ configuration is such that pressure waves moving along the vertical direction can propagate unperturbed along short beam elements alternated by horizontal beams where the waves need to convert into shear waves in order to propagate. This phenomenon is captured by the diamond curve in fig. 59 that features in fact a drop in the pressure wave speed for $\gamma = \pm 90^o$. As a last note, the $\theta = 10^o$ and $\theta = -10^o$ lattices feature the same maximum value of c_{P_x}, as a consequence of having inclined beams sharing the same projection along x (fig. 60).

The variation of the shear wave with γ for the considered lattices is shown in fig. 59.b and is consistent with the phase constant surfaces presented at the beginning of this Chapter.

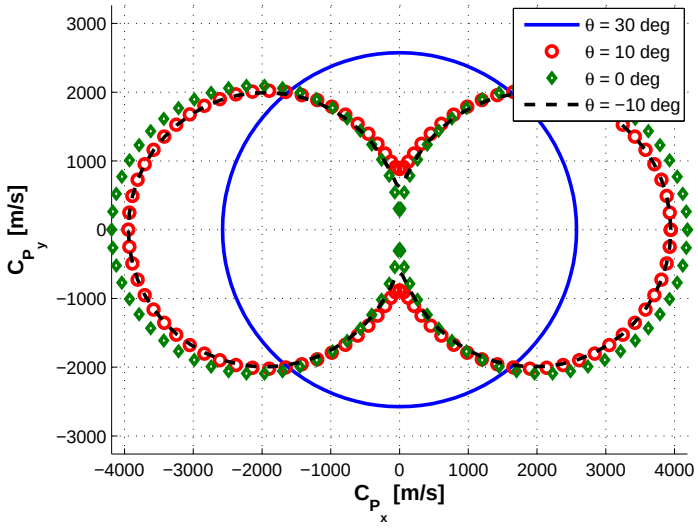

(a) P-mode

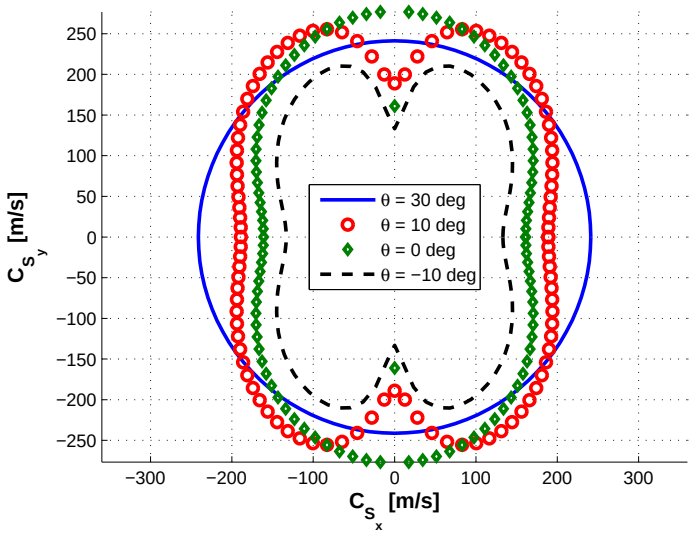

(b) S-mode

Figure 59: Wave velocities for different configurations

However considerations about the physical explanations of these curves are not as easy to draw as for the pressure wave.

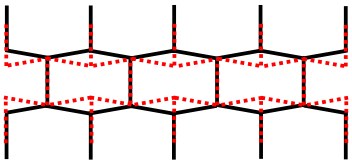

Figure 60: Comparison between classical hexagonal lattice ($\theta = 10^o$) and re-entrant lattice ($\theta = -10^o$)

CHAPTER IV

MULTI-CELL ANALYSIS

4.1 Introduction

In chapter II and III, homogenization has been introduced as a technique to investigate the dynamic behavior of structures composed of the assembly of repetitive cells. The objective of this technique is to obtain a continuum representation of periodic domains, while preserving information about the properties and geometry of their microscopic components. It has been shown that homogenization represents a reliable analysis tool capable of serving two purposes: reducing the computational cost and offering insights into various elasto-dynamic phenomena. Special focus has been placed on wave propagation analysis, and in particular on the approximation of dispersion relations. It is worth observing that, while modal and harmonic analyses of periodic structures in general require large calculations, since they usually involve a finite-element discretization of the whole structure under consideration, obtaining dispersion relations is a much less expensive task, since it is entirely conducted on the single repetitive element. Therefore, the need to approximate dispersion relations using homogenization techniques does not generate from concerns about the computational cost of the task. It has more to do with the insight that approximate dispersion relations offer about the approximation technique itself. Comparing dispersion relations obtained through homogenization with the exact ones provides a metric of the accuracy of the approximation technique. Chapter II shows how dispersion relations constitute the basic framework for the derivation of approximate PDEs for the homogenized structure. The solution of these PDEs is expected to give a reliable answer only at those frequencies at which good agreement is exhibited by the dispersion relations plot. In chapters I, II and III, it has been stated that homogenization works in the long-wavelength limit, i.e. for low values of the wavenumber; homogenization is therefore capable of providing dispersion relations curves that approximate the exact ones for $\boldsymbol{\xi} \longrightarrow 0$.

An interesting extension of the multi-scale approach of chapter II is achieved through a multi-cell analysis, based on the extension of the unit cell-based homogenization to a larger portion of the structure corresponding to two or more neighboring cells. This approach has been suggested and implemented for various lumped parameters systems by Vasiliev and coworkers [85, 86]. The multi-cell analysis generates multiple approximate frequency-wavenumber curves and aims to extend the area of agreement between exact and approximate solutions to other regions of the frequency domain, thus allowing a good approximation of the dynamic behavior of a structure over a broader range of frequency/wavelengths.

The objective of the work presented in this chapter is to extend the formulation to periodic structural assemblies of engineering interest such as trusses and frames, where the single elements within the periodic pattern are classical continuous structural components. The development of a general matrix-based procedure applicable to various structural configurations constitutes an original contribution of this work.

4.2 Concept

4.2.1 Motivations and objectives

The objective of this chapter is to expand the previous approach to extend the good approximation to another important region of the wavenumber domain, the high wavenumber/short wavelength limit. In virtue of the connection between the dispersion relations and the continuum model, obtaining multiple regions of agreement in the frequency domain automatically translates into the possibility of generating approximate solutions over a wider frequency spectrum. There is a second advantage deriving from this idea: being able to reconstruct the short wavelength limit allows understanding the behavior of the structures at high frequencies and potentially investigate the behavior of the structure in the proximity of a bandgap.

The main idea of the multi-cell technique is to perform the analysis of the periodic medium by considering a macro-cell made of two (or more) contiguous unit cells as the irreducible unit of the system (fig. 61). This approach is formalized in the following section, while it is here applied to the simple 1D spring-mass system of fig. 62 for illustration

purposes.

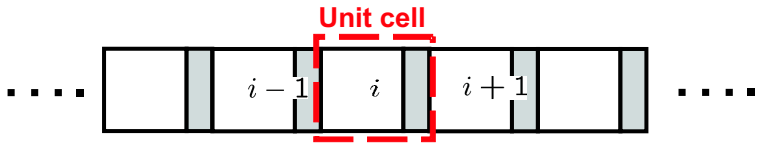

(a) Single cell approach

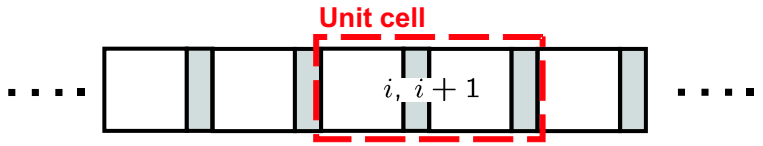

(b) Two cell approach

Figure 61: Single cell and multi-cell (two cells) approach to the analysis of a generic 1D periodic medium

4.2.2 Application to a one-dimensional spring-mass system

Based on the developments described in [86], the long wavelength approximation of the equation of motion of the domain can be described in terms of the macro-cell degrees of freedom $\{u_0,\ u_1\}^T$ to obtain an expression of the kind:

(a)

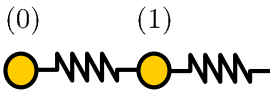

(b)

Figure 62: Periodic spring mass system and considered macro-cell.

$$\begin{bmatrix} 2-\omega^2 & \xi^2-2 \\ \xi^2-2 & 2-\omega^2 \end{bmatrix} \begin{Bmatrix} u_0 \\ u_1 \end{Bmatrix} = \mathbf{0} \tag{142}$$

where ω and ξ respectively denote frequency and wavenumber and spring stiffness constants and concentrated masses are set equal to 1. Setting the determinant of the matrix in

eq. (142) equal to 0 yields two roots representing two approximate branches of the dispersion relation:

$$\omega^2 = \xi^2, \quad \omega^2 = 4 - \xi^2 \tag{143}$$

Figure 63 shows how the two branches approximate the exact dispersion relation in the neighborhood of $\xi \longrightarrow 0$ and $\xi \longrightarrow \pi$, which respectively are the boundaries of the first Brioullin zone of the domain, and define the long and short wavelength behavior of the assembly. The increase in the number of particles in a unit cell from one to two corresponds to the reduction of the first Brillouin zone by half and to the folding of the dispersion relations around the $\xi = \pi/2$ line. For reference, the value $\xi = \pi$ corresponds to a wavelength $\lambda = 2d$, with d denoting the spatial period of the domain. Some physical insight into this

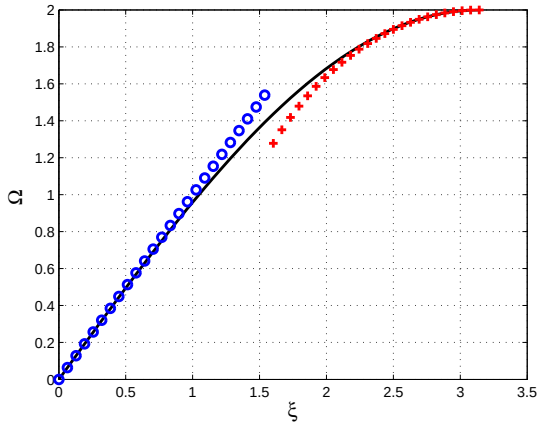

Figure 63: Comparison between exact (solid line) and apprixmate dispersion relations (1^{st} branch 'o', 2^{nd} branch '+') for the spring mass system.

result can be gained by considering the following change of coordinates:

$$\begin{aligned} u_a &= \frac{u_0 + u_1}{2} \\ u_d &= \frac{u_1 - u_0}{2} \end{aligned} \tag{144}$$

where u_a and u_d respectively define the macro-cell's average displacement and an intra-cell deviatoric displacement. It can be observed that, in this case, the change of coordinates decouples the two equations in eq. (142). The eigenvectors corresponding to the two branches

of the dispersion relations define the wave modes of the domain, which are given by:

$$\left\{ \begin{array}{c} u_a \\ u_d \end{array} \right\}_I = \left\{ \begin{array}{c} 1 \\ 0 \end{array} \right\}, \quad \left\{ \begin{array}{c} u_a \\ u_d \end{array} \right\}_{II} = \left\{ \begin{array}{c} 0 \\ 1 \end{array} \right\} \tag{145}$$

Equation (145) shows how the mode associated with the first branch describes waves whose amplitude changes very slowly along the length of the domain, so that the displacement of particles belonging to the same cell is approximately equal. In contrast, the second mode is only characterized by intra-cell displacements, with zero average displacement of the cell. Hence the second branch describes to the limit a wave whose average amplitude over the macro-cell is zero. Alternatively, one can express the same wave modes in the original set of coordinates to obtain:

$$\left\{ \begin{array}{c} u_0 \\ u_1 \end{array} \right\}_I = \left\{ \begin{array}{c} 1 \\ 1 \end{array} \right\}, \quad \left\{ \begin{array}{c} u_0 \\ u_1 \end{array} \right\}_{II} = \left\{ \begin{array}{c} -1 \\ 1 \end{array} \right\} \tag{146}$$

which demonstrate that the modes respectively represent in-phase and out-of-phase motion of neighboring particles.

4.3 Multi-cell Analysis of 1D Periodic Structures

4.3.1 Two-cell analysis

Let us consider a macro-cell consisting of two neighboring unit cells as depicted schematically in Fig. 64. The formulation of the problem follows the same procedure introduced for the

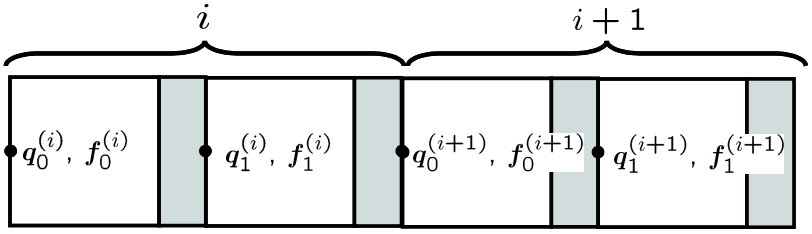

Figure 64: Macro cell for two-field approximation

single cell analysis. Specifically, the interaction of the macro-cell i with the subsequent cell $i+1$ can again be described in the general form:

$$(\mathbf{K} - \omega^2 \mathbf{M}) \ \mathbf{q} = \mathbf{f} \tag{147}$$

where now $\mathbf{K}$ and $\mathbf{M}$ are the mass and stiffness matrices for the assembly including macro-cells i and $i+1$, while the vector of the generalized nodal displacements $\mathbf{q} = \{\mathbf{q}_L,\ \ \mathbf{q}_R\}^T$ and forces $\mathbf{f} = \{\mathbf{f}_L,\ \ \mathbf{f}_R\}^T$ are now given by:

$$\begin{aligned} \mathbf{q}_L &= \{\mathbf{q}_0^{(i)},\quad \mathbf{q}_1^{(i)}\}^T \\ \mathbf{q}_R &= \{\mathbf{q}_0^{(i+1)},\ \mathbf{q}_1^{(i+1)}\}^T \end{aligned} \tag{148}$$

The same procedure presented for the single cell analysis can be followed with only some minor modifications. First of all, matrices dimensions need to be updated to account for the larger number of degrees of freedom. In addition, the periodicity condition to be imposed between boundary degrees of freedom now reads:

$$\mathbf{q}_R = e^{-2i\xi}\ \mathbf{q}_L \tag{149}$$

Accordingly, the reduction matrix $\mathbf{W}$ introduced in eq. (150) becomes:

$$\mathbf{W} = \begin{bmatrix} \mathbf{I}_{2n} \\ e^{-i2\xi}\mathbf{I}_{2n} \end{bmatrix} \tag{150}$$

and the reduced mass and stiffness matrices are given by:

$$\mathbf{K}_r = \mathbf{K}_{LL} + e^{i2\xi}\ \mathbf{K}_{LR} + e^{-i2\xi}\ \mathbf{K}_{RL} + \mathbf{K}_{RR} \tag{151}$$

$$\mathbf{M}_r = \mathbf{M}_{LL} + e^{i2\xi}\ \mathbf{M}_{LR} + e^{-i2\xi}\ \mathbf{M}_{RL} + \mathbf{M}_{RR} \tag{152}$$

with the dimensions of the matrices partitions properly updated.

The physical interpretation of this approach described for the single degree of freedom system can be extended to a generic periodic domain. The coordinate transformation yielding averaged and deviatoric degrees of freedom, respectively denoted as $\mathbf{q}_a$ and $\mathbf{q}_d$, can be expressed as follows:

$$\begin{aligned} \mathbf{q}_a = \frac{1}{2}\Big(\mathbf{q}_L + \mathbf{q}_I\Big) &= \frac{1}{2}\,[\,\mathbf{I}\quad \mathbf{I}\,]\left\{\begin{array}{c}\mathbf{q}_0\\ \\ \mathbf{q}_1\end{array}\right\} \\ \mathbf{q}_d = \frac{1}{2}\Big(\mathbf{q}_I - \mathbf{q}_L\Big) &= \frac{1}{2}\,[\,-\mathbf{I}\quad \mathbf{I}\,]\left\{\begin{array}{c}\mathbf{q}_0\\ \\ \mathbf{q}_1\end{array}\right\} \end{aligned} \tag{153}$$

where the notation is simplified to read $\mathbf{I} = \mathbf{I}_n$, $\mathbf{q}_0^{(i)} = \mathbf{q}_0$, and $\mathbf{q}_1^{(i)} = \mathbf{q}_1$. The two equations in (153) can be recast in matrix form as:

$$\mathbf{q}^* = \mathbf{A} \left\{ \begin{array}{c} \mathbf{q}_0 \\ \\ \mathbf{q}_1 \end{array} \right\} \tag{154}$$

where $\mathbf{q}^* = \{\mathbf{q}_a,\ \mathbf{q}_d\}^T$ and $\mathbf{A}$ is the transformation matrix defined as:

$$\mathbf{A} = \frac{1}{2} \left[\begin{array}{cc} \mathbf{I} & \mathbf{I} \\ \\ -\mathbf{I} & \mathbf{I} \end{array} \right] \tag{155}$$

Elasto-dynamic equations in terms of the new set of degrees of freedom can be obtained through the following transformed stiffness and mass matrices:

$$\begin{aligned} \mathbf{K}_r^* &= \mathbf{A}\mathbf{K}_r\mathbf{A}^{-1} \\ \mathbf{M}_r^* &= \mathbf{A}\mathbf{M}_r\mathbf{A}^{-1} \end{aligned} \tag{156}$$

As discussed in the case of the spring mass system, the new sets of degrees of freedom $\mathbf{q}_a$ and $\mathbf{q}_d$ respectively describe long wavelength perturbation patterns and intra-cell oscillations. Equivalent continuum equations governing the two types of motion can be obtained through scaling and Taylor series expansion of the transformed symbol:

$$\mathbf{\Gamma}_r^*(\xi) = [\mathbf{K}_r^*(\xi) - \omega^2 \mathbf{M}_r^*(\xi)] \tag{157}$$

The dispersion relation resulting from the expansion for $\epsilon \to 0$ simultaneously approximates the long wavelength and the short wavelength behavior of the structure corresponding to wavelengths $\lambda \to 2d$, where d is the spatial period of the domain. This is based on the observation that increasing the unit cell to include two irreducible units corresponds to reducing the extent of the First Brioullin region by half, and folding the resulting dispersion relations about the $\xi = \pi/2$ line. It is interesting to note that typically, as opposed to the case of the single degree of freedom system, the procedure yields a coupled set of equations, which suggests that the long wavelength behavior is affected by the behavior and by the properties of the unit cell. In other words, the coupling between averaged and deviatoric degrees of freedom corresponds to a coupling between different scales in the problem.

4.3.2 Four-cell analysis

Based on the approach outlined for the two-cell analysis we can extend the technique to a macro-cell including a higher number of unit cells. For example one may consider a macro-cell consisting of four elementary unit cells, and modify the procedure presented in the previous section to account for the larger dimensions of the unit cell. The propagation condition between boundary degrees of freedom can be updated to read

$$\mathbf{q}_R = e^{-i4\xi}\, \mathbf{q}_L \tag{158}$$

A structural difference arises in the construction of the transformation matrix $\mathbf{A}$ that converts the nodal values into a new set of coordinates. The average, the semi-difference of the average and of the semi-difference of the nodal quantities [86] are chosen for the reduction of the elasto-dynamic equations, resulting in a nested procedure. Like in the previous case, we can define a new vector of degrees of freedom

$$\mathbf{q}^* = \mathbf{A}\, \mathbf{q}_r \tag{159}$$

where $\mathbf{A}$ is now defined as:

$$\mathbf{A} = \mathbf{A}_2\, \mathbf{A}_1 \tag{160}$$

with

$$\mathbf{A}_1 = \begin{bmatrix} \frac{1}{2}\mathbf{I} & \frac{1}{2}\mathbf{I} & \mathbf{0} & \mathbf{0} \\ -\frac{1}{2}\mathbf{I} & \frac{1}{2}\mathbf{I} & \mathbf{0} & \mathbf{0} \\ \mathbf{0} & \mathbf{0} & \frac{1}{2}\mathbf{I} & \frac{1}{2}\mathbf{I} \\ \mathbf{0} & \mathbf{0} & \frac{1}{2}\mathbf{I} & \frac{1}{2}\mathbf{I} \end{bmatrix} \tag{161}$$

and

$$\mathbf{A}_2 = \begin{bmatrix} \frac{1}{2}\mathbf{I} & \mathbf{0} & \frac{1}{2}\mathbf{I} & \mathbf{0} \\ -\frac{1}{2}\mathbf{I} & \mathbf{0} & \frac{1}{2}\mathbf{I} & \mathbf{0} \\ \mathbf{0} & \frac{1}{2}\mathbf{I} & \mathbf{0} & \frac{1}{2}\mathbf{I} \\ \mathbf{0} & \frac{1}{2}\mathbf{I} & \mathbf{0} & \frac{1}{2}\mathbf{I} \end{bmatrix} \tag{162}$$

The comparison of the two and four-cell analyses can suggest a repetitive pattern, according to which one theoretically could extend the procedure to any number n of unit cells. The

resulting n-cell symbol will yield n branches of the dispersion relations which will approximate the exact ones over a $1/n$ portion of the first Brioullin zone, with symmetric folding of the dispersion relations occurring at lines spaced of an interval ξ/n.

4.4 Examples

4.4.1 One-dimensional truss structure

A first interesting test for the analysis presented above is the 1-D truss of fig. 65. Young's modulus, density and cross sectional area of the bar elements are indicated in fig. 65 as well as characteristic geometric and material properties. It is assumed that the truss undergoes

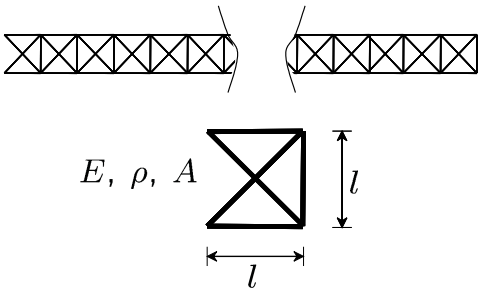

Figure 65: One-dimensional truss lattice with highlighted elementary unit cell

exclusively axial motion. To enforce this, the nodes of the truss are constrained to move along the longitudinal direction x only. Upon reduction, the behavior of each cell is described by the two degrees of freedom shown in fig. 66. Therefore the dispersion relations feature two branches corresponding to two wave modes of longitudinal propagation along the truss (see fig. 67).

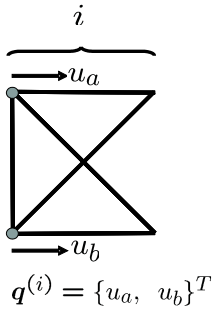

Figure 66: Unit cell and degrees of freedom for the 1D truss

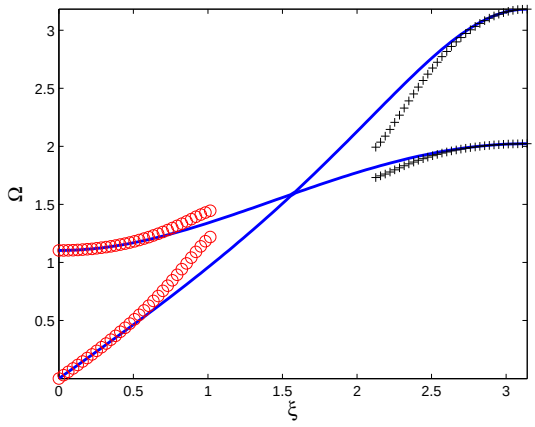

Figure 67: Exact and two-cell approximation of the dispersion relations of the 1D truss (exact: solid line, 1^{st} branch approximation 'o', 2^{nd} branch approximation '+').

Applying the two-cell analysis and solving the approximate characteristic equation yields four roots corresponding to two sets of approximate curves. Two of them approximate the exact curves for $\xi \to 0$, the others, if mirrored about the $\xi = \pi/2$ axis, approximate the exact solution for $\xi \to \pi$. Exact and approximate two-cell dispersion relations are plotted in fig. 67. In the plots, the frequency axis is normalized with respect to the properties of the truss elements, according to the following definition:

$$\Omega = \omega l \sqrt{\frac{\rho}{E}} \tag{163}$$

The approximate curves are obtained truncating the Taylor's series expansion of the determinant of the symbol up to the $\mathcal{O}(\epsilon^3)$ term. An advantage of the technique is that even with a low order of Taylor series expansion, one can obtain good approximations over a large range for ξ, which particularly includes the neighborhood of π. With the homogenization approach presented in Chapter II involving simple Taylor series expansion of the scaled symbol, that region of the plot could have been successfully approximated only by including a much higher number of terms in the Taylor series. The downside of the technique is its weakness in the central region of the first Brillouin zone, where none of the approximating branches manage to approximate the exact curves. Such shortcoming may be overcome by increasing the order of the Taylor series. By doing that, the approximate curves progressively converge to the exact ones, as shown in fig. 68. The peculiar result of a

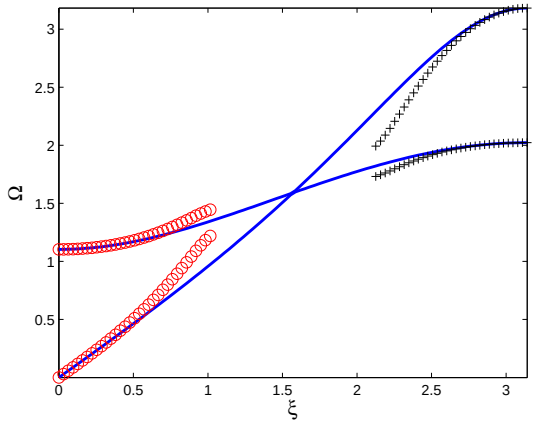

(a) $\mathcal{O}(\epsilon^3)$

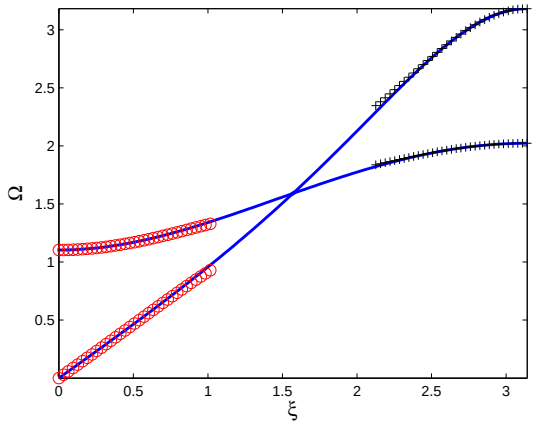

(b) $\mathcal{O}(\epsilon^5)$

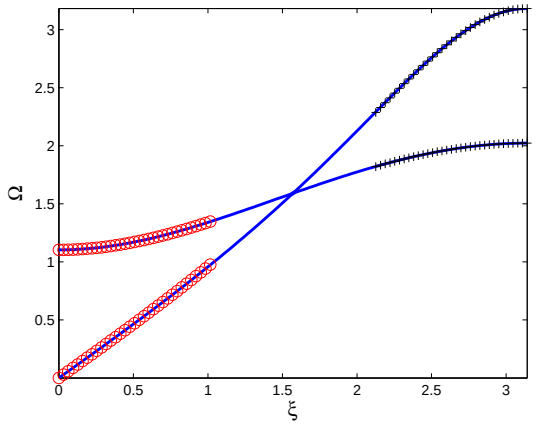

(c) $\mathcal{O}(\epsilon^7)$

Figure 68: Two-cell approximation of the truss dispersion relations for increasing Taylor series order (exact: solid line, 1^{st} branch approximation 'o', 2^{nd} branch approximation '+').

multi-cell approach consists in extending the region of agreement while containing the order of the expansion. This results in less complicated expressions for the dispersion relations which can be converted into low order partial differential equations (PDEs) governing the behavior of the equivalent continuum [27] even in the short wavelength limit. The derivation of equivalent PDEs for periodic lattices over different frequency ranges constitutes in fact the ultimate goal of the multi-cell analysis as investigated here. Approximate dispersion relations are again used as a metric for the validity of the approximation.

A four-cell approximation can also be obtained through the procedure described in Section 4.3.2. The resulting approximate characteristic equation yields eight roots, which correspond to four sets of approximate curves. Two of them approximate the exact curves for $\xi \to 0$, two others, if mirrored about the $\xi = \pi/2$ axis, approximate the exact solution for $\xi \to \pi$, the other four work in the neighborhood of $\xi \to \pi/2$. Exact and approximate four-cell dispersion relations obtained for increasing Taylor series orders are plotted in fig. 69. The main achievement of the four-cell analysis, compared to the two-cell one, is to provide approximate values of the dispersion relations in the central region of the frequency/wavenumber domain.

4.4.2 One-dimensional frame

A second application of the multi-cell approach is the frame structure of fig. 70. From a geometric standpoint, the structure is not different from the truss of Section 4.4.1. However, the elements are rigidly connected and are therefore modeled as beams undergoing axial as well as flexural deformation in the plane of the structure. The behavior of each node is described by three degrees of freedom, which correspond to six degrees of freedom per cell. The possibility of thick short beam elements is addressed by adopting a Timoshenko beam formulation in the FE assembly of the unit cell, defined in terms of beam slenderness ratio Φ.

The exact dispersion relations for the frame are shown in fig. 71 as solid lines. In the same plots, the approximate curves obtained from the two-field analysis are plotted, showing a good level of approximation at the boundaries of the wavenumber domain. Again,

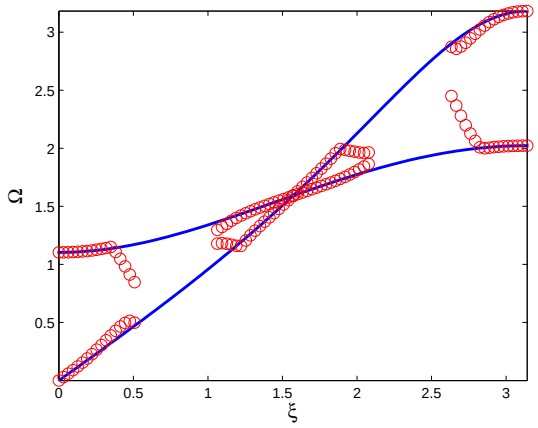

(a) $\mathcal{O}(\epsilon^3)$

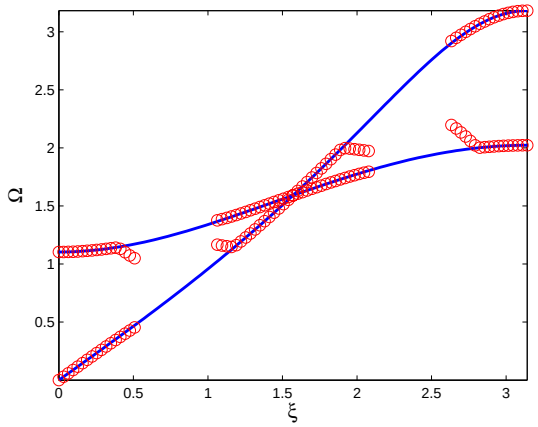

(b) $\mathcal{O}(\epsilon^5)$

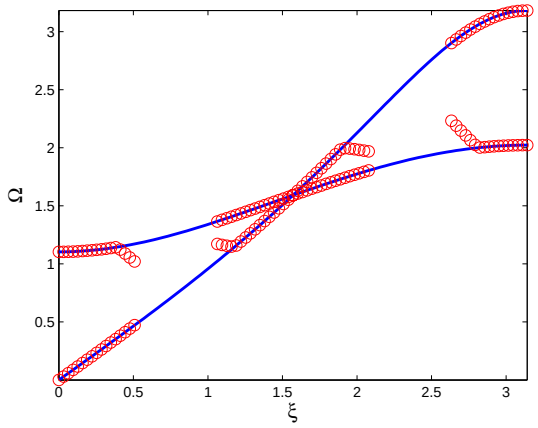

(c) $\mathcal{O}(\epsilon^7)$

Figure 69: Four-cell approximation of the truss dispersion relations for increasing Taylor series order (exact: solid line, approximated 'o').

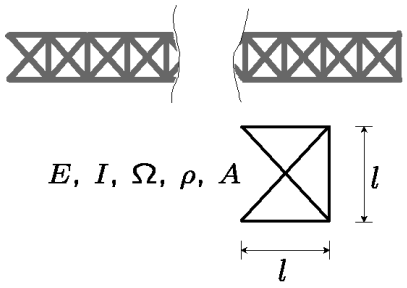

Figure 70: Unit cell and properties of the 1D frame.

increasing the order of the Taylor series expansion generally produces an improvement in agreement with the exact solution. The central region of the curves remains outside the area of good agreement, regardless of how many terms are retained in the Taylor's series. Moreover, for some values of ξ, the approximate curves simply detach from the exact ones with sharp discontinuities in slope. The mathematical and physical reasons behind this phenomenon are currently under investigation.

Figure 72 shows the results of a four-field analysis performed on the frame structure. Considerations about the improving accuracy similar to those drawn for the case of the truss can be easily made by inspection of the plots. The same issues observed for the previous case are visible in the neighborhood of $\xi = \pi/2$. In addition to that, one of the curves fails to approximate the solution for $\xi \to 0$. It is believed that the mismatch between the curves observed before is to be considered responsible for this additional phenomenon.

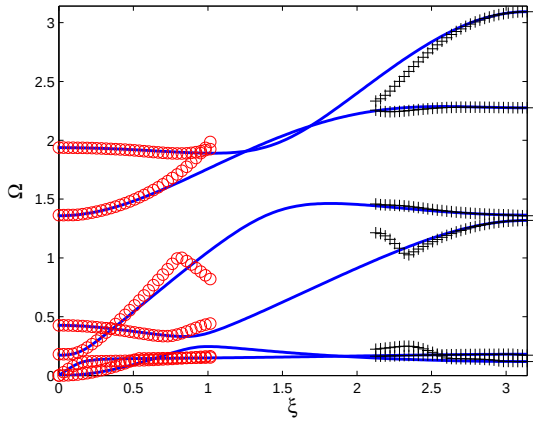

(a) $\mathcal{O}(\epsilon^3)$

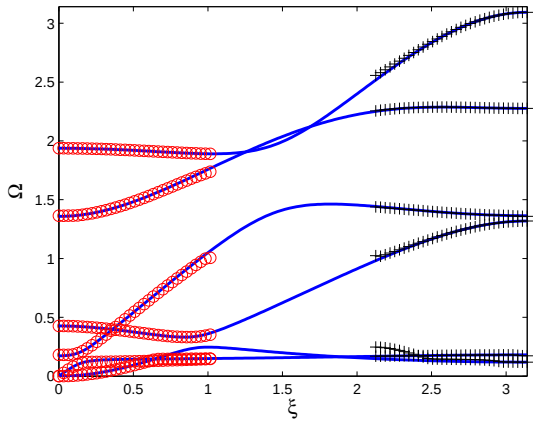

(b) $\mathcal{O}(\epsilon^5)$

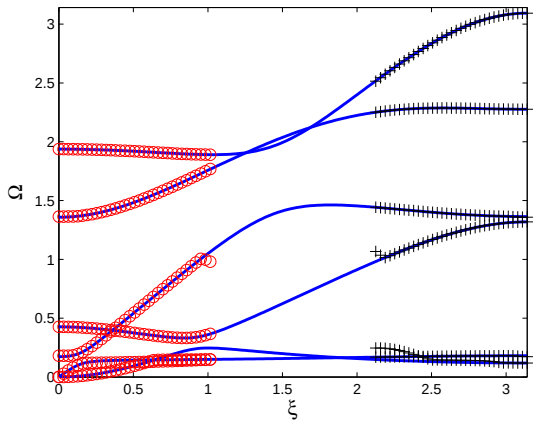

(c) $\mathcal{O}(\epsilon^7)$

Figure 71: Two-cell approximation of the frame dispersion relations for increasing Taylor series order (exact: solid line, 1^{st} branch approximation 'o', 2^{nd} branch approximation '+').

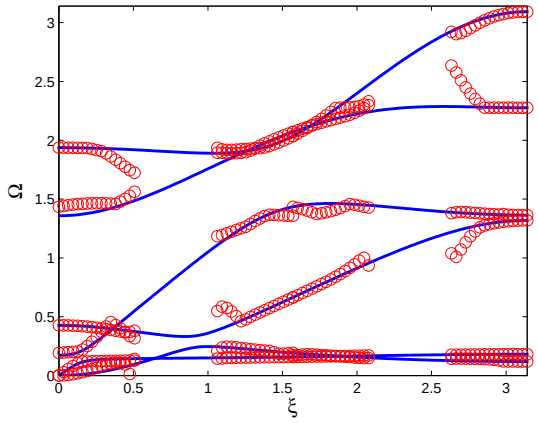

(a) $\mathcal{O}(\epsilon^3)$

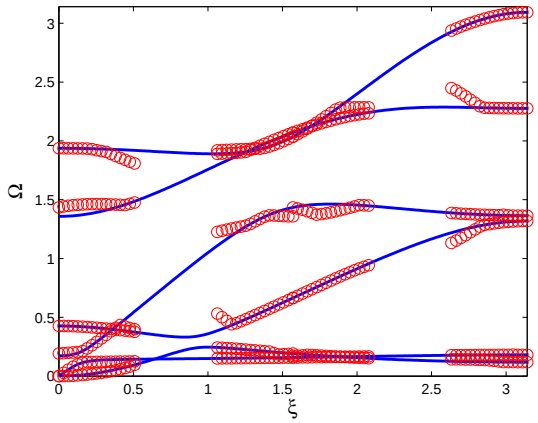

(b) $\mathcal{O}(\epsilon^5)$

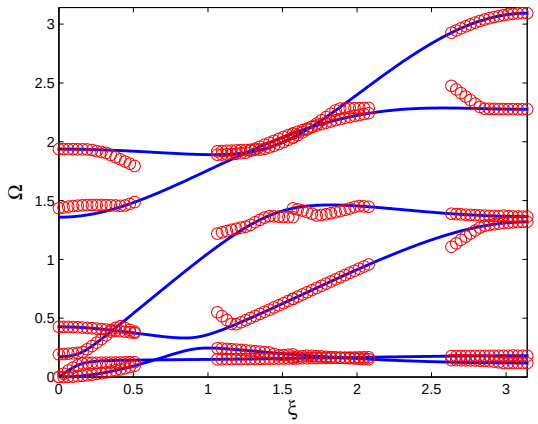

(c) $\mathcal{O}(\epsilon^7)$

Figure 72: Four-cell approximation of the frame dispersion relations for increasing Taylor series order (exact: solid line, approximated 'o').

4.5 Multi-cell Estimation of the Harmonic Response

The procedure described above can be applied to formulate a "super-element", which predicts the response of the periodic assembly, without the need for a detailed FE model. This process introduces an approximation which depends on the order of truncation in the expansion in terms of the multi-scale parameter ϵ. The solution of the resulting continuum equation is however only possible if a sufficient number of boundary conditions can be formulated. This introduces limitations on the order of approximation that can be achieved, as refining the order of the series corresponds to increasing the order of the continuum equation. Such limitations motivate the application of the multi-cell technique to extend the range of approximation to a broader frequency range.

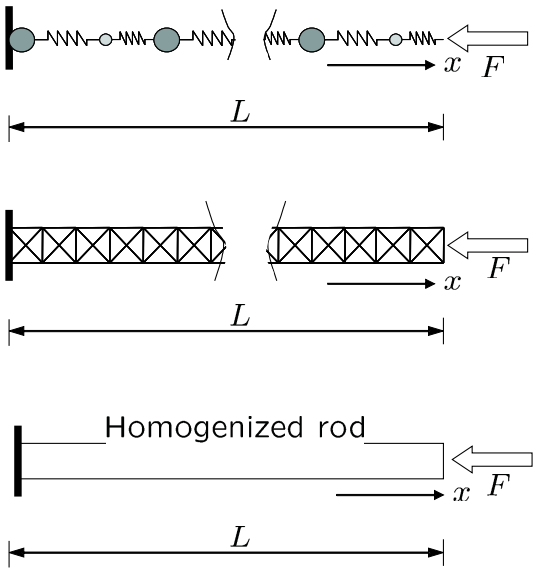

Figure 73: Considered 1D periodic structures and homogenized continuous rod

It is assumed that all the considered structures are fixed at one end and excited at the opposite end by a longitudinal harmonic force. A schematic of the considered configurations is shown in fig. 73, which also highlights the concept of an equivalent uniform rod approximating the considered periodic domains. We investigate spring-mass and truss systems that are constrained to undergo displacements along a longitudinal coordinate. This allows imposing a maximum of two conditions on either the boundary displacements or on their

rate, so that the governing PDEs must be of 2^{nd} order in space.

In the case of the spring mass system, the two expressions in eq. (143) can be used to derive continuum differential equations by means of the inverse discrete Fourier transform, according to the technique detailed in Chapter II, which corresponds to the following substitution in eq. (142):

$$i\xi \rightarrow \frac{\partial}{\partial x}, \;\; \xi^2 \rightarrow -\frac{\partial^2}{\partial x^2}, \tag{164}$$

The process, in conjunction with the two-cell representation and the associated coordinate change of eq. (153), yields the following two equations of motion in terms of u_a, u_d:

$$\begin{aligned} \frac{d^2 u_a}{dx^2} + \omega^2 u_a = 0 \\ \frac{d^2 u_d}{dx^2} + (4 - \omega^2) u_d = 0 \end{aligned} \tag{165}$$

which respectively define the behavior of the periodic spring mass domain in the long and short wavelength regimes.

A solution for both of eq.s (165) can be expressed as:

$$u(x) = c_1 e^{i\xi_1 x} + c_2 e^{i\xi_2 x} \tag{166}$$

where c_1, c_2 are integration constants, while ξ_1, ξ_2 are obtained from the solution of the approximate dispersion relations. It is worth observing that the long wavelength approximation based on the single-cell analysis for this domain would yield a unique equation coinciding with the first of eq.s (165), which has the form of a classical wave equation. Another interesting observation can be made regarding the solution u_d, whose associated wavenumbers become real for $\omega > 2$, which is the value of frequency defining the lower boundary of the stop-band for the system. Hence, the two cell representation provides equivalent continuum equations which still capture relevant characteristics, such as the stop band, of the original periodic assembly. The harmonic response of a finite spring mass assembly containing 25 cells is plotted in Fig. 74, where a comparison between exact and approximate response is presented. The plots show how solution of the continuum equation approximates well the exact response, obtained from the matrix formulation of the original problem, at low values of frequency and at frequencies close to the upper boundary of the

first Brioullin zone. The agreement in this high frequency range can be observed from the detail of the response shown in Fig. 74.b.

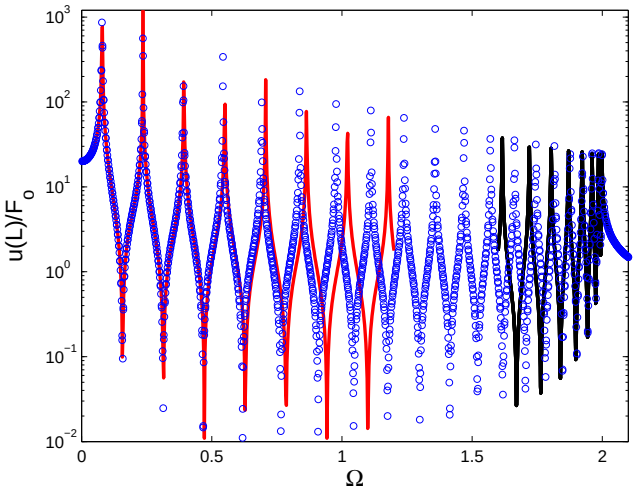

(a)

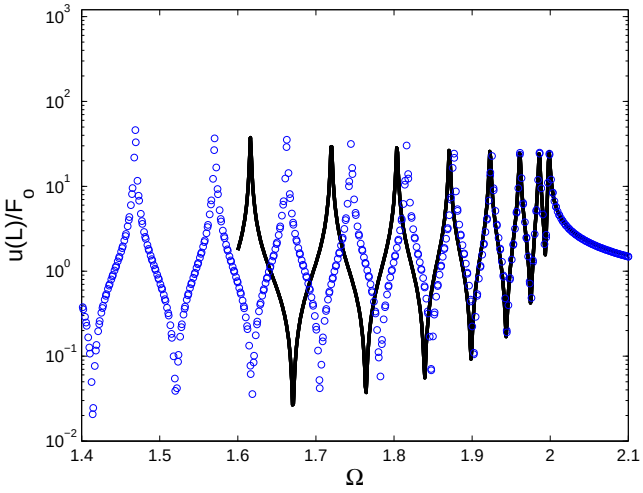

(b)

Figure 74: Comparison between exact and approximate harmonic response for the spring mass system(exact 'o', approximate solid lines).

The harmonic response of the truss shown in Fig. 75 is also estimated through the two cell approach. The considered truss contains 30 unit cells, and its exact response is evaluated through a standard FE model which considers each bar as a single element. The continuum equation resulting from the two cell analysis and subsequent Taylor series expansion, is a

second order PDE with a 4 component displacement unknown. Assuming harmonic motion at frequency ω, the equation can be generally expressed as:

$$\boldsymbol{A}(\omega)\boldsymbol{u}_{,xx}(x) + \boldsymbol{B}(\omega)\boldsymbol{u}(x) = \boldsymbol{0} \tag{167}$$

where $\boldsymbol{A}, \boldsymbol{B}$ are frequency dependent matrix coefficients, which are also functions of the properties and of the geometry of the unit cell. Also, $\boldsymbol{u}(x) = \{\boldsymbol{u}_a(x),\ \boldsymbol{u}_d(x)\}^T$ is a vector that contains the continuum versions of average and deviatoric displacement vectors $\boldsymbol{q}_a, \boldsymbol{q}_d$. The comparison between exact and approximate response is shown in Fig. 75.a, while Fig. 75.b shows the detailed comparison in the high frequency range. It is worth observing that the approximate responses are obtained from the analytical solution of eq. (167), which is found analytically, while the exact solution requires the formulation of a potentially large problem. The proposed technique can therefore lead to substantial reductions in computational time if the dynamic response of large periodic systems needs to be evaluated over the frequency ranges highlighted in this work.

4.6 Conclusions

This chapter presents a multi-cell technique for the analysis of 1D periodic structures. The technique studies wave propagation by considering enlarged versions of the unit cell of the domain. The combination of the multi-cell analysis with a Fourier-based homogenization technique allows the approximation of the dispersion relations both in the low and high frequency regimes. This potentially provides insights in unique characteristics, such as presence of bandgaps, of the periodic structure. Examples on simple spring mass systems, trusses and frames show the potentials of the technique, which can be extended to include the estimation of the harmonic response of finite periodic domains. This potential is demonstrated by two examples which show how continuum equations can be derived and solved to approximate the harmonic response of the structure over the above mentioned frequency ranges.

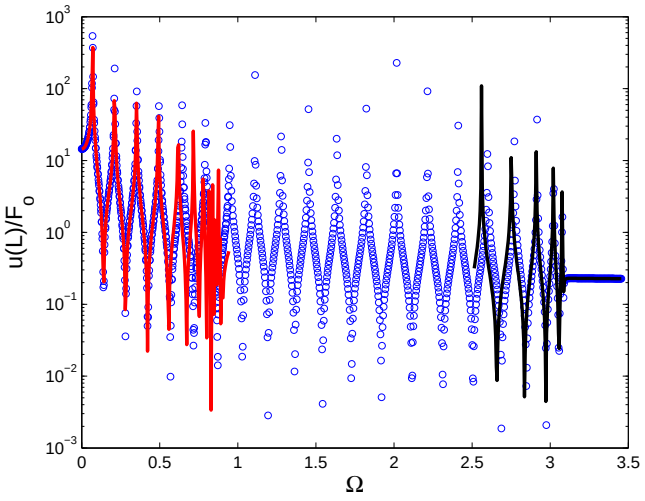

(a)

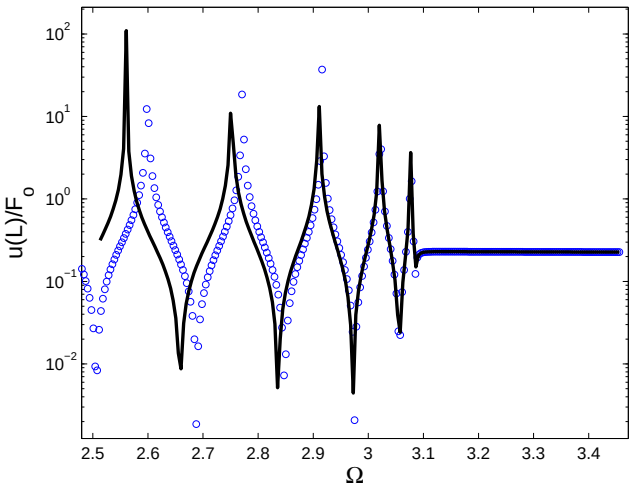

(b)

Figure 75: Comparison between exact and approximate harmonic response for the truss (exact 'o', approximate: solid lines).

CHAPTER V

BRIDGING MULTI-SCALE METHOD

5.1 Introduction

The periodicity of the medium under consideration is a necessary condition for applying the considered homogenization technique. In other words, we must be able to isolate a repetitive volume element (RVE) and describe the structure of interest as a repetition in space of that element. A major limitation to the applicability of the homogenization approach arises when a structure features one or more discontinuities within its domain. Discontinuities can have different nature. They might be due to localized damages, abrupt changes in the geometric or material properties between neighboring regions of the medium, stiff inclusions, cracks, plastic hinges etc. Whatever their nature might be, they always represent an interruption of the regularity of the periodic pattern. Localized damages like cracks or stiff inclusions are of particular interest since they represent points of structural weakness. The investigation of such critical discontinuities is often the object of studies and simulations in support of damage detection techniques. Wave propagation-based techniques are based on the common knowledge that mechanical waves generally propagate unperturbed through undamaged regions of a solid, while they are reflected by localized damages or abrupt changes in the mechanical properties of the medium. The numerical analysis of waves interacting with damages is very useful in order to simulate behaviors of damaged and undamaged structures to be compared with experimental measurements in support of their interpretation and of the development of detection algorithms.

One possible way to integrate homogenization with a detailed description of non-periodic regions within the domain is through the so-called *bridging multi-scale* method [38, 39, 88, 68]. According to this approach, the domain of interest is discretized with a coarse mesh which captures the macroscopic behavior of the structure. In addition, a refined mesh is superimposed to the coarse mesh over the region around the discontinuity (fig. 76). This

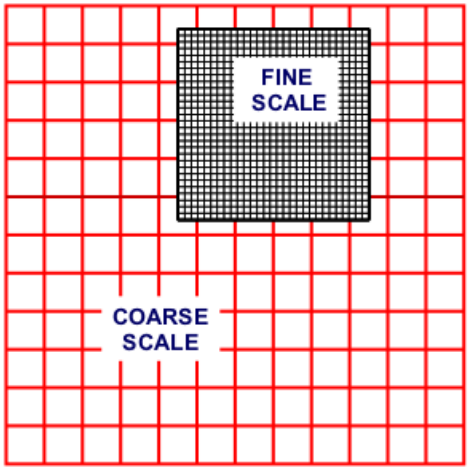

Figure 76: Schematic for the FE discretization with two meshes

operation is intended to reduce the overall size of the problem, while accurately capturing localized effects in the region of interest. The employment of multiple meshes, however, causes numerical problems documented, for example, in [68]. The co-existence of two scales in the model produces spurious reflected waves at the interface between the two meshes. These spurious waves are mainly due to the difference in size between neighboring elements belonging to different meshes (fig. 77). These reflected waves are purely numerical and can be easily confused with true reflected waves due to the actual physical configuration of the structure, thus interfering with proper damage simulation. The elimination of spurious waves can be achieved through the application of proper bridging relations between the two scales. Interaction forces at the interfaces known as impedance forces are added into the model to bridge the two scales and therefore to minimize spurious discontinuities. This method allows a coarse description of the global behavior of the structure while simultaneously obtaining local information regarding the interaction of the propagating wave with a small discontinuity in the domain.

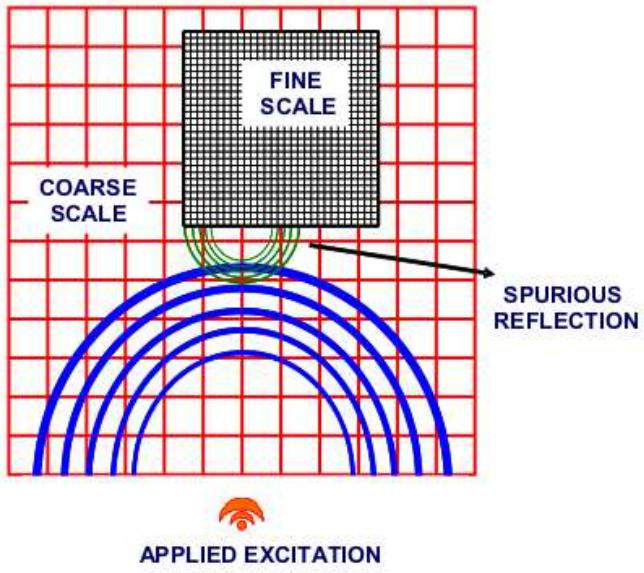

Figure 77: Schematic for the generation of spurious reflective waves at the scale interface

5.2 Theoretical Background

5.2.1 Bridging matrices

Let us consider an elastic domain discretized by a coarse-scale FE and a fine-scale FE mesh as depicted in fig. 78. The underlying assumption is that the resolution of the fine mesh is high enough to capture the localized phenomena under investigation and that of the coarse mesh is such that the computation over the whole domain is possible at a reasonable cost. Parameters n_c and n_f define the number of degrees of freedom in the coarse and in the fine mesh, respectively. Let the displacement vector $\mathbf{u}$ describing the behavior of the domain be expressed as:

$$\mathbf{u} = \mathbf{N}\,\mathbf{d} + \mathbf{Q}\,\mathbf{q} \tag{168}$$

where $\mathbf{q}$ and $\mathbf{d}$ represent the fine-scale solution and the coarse-scale solution, respectively. The operator $\mathbf{N}$ of size $n_f \times n_c$ interpolates the coarse-scale solution at the nodal positions of the fine-scale mesh. On the other hand, $\mathbf{Q}$ is a square matrix of size $n_f \times n_f$ whose purpose is to subtract the information about the displacement shared between the scales. The following notation is introduced:

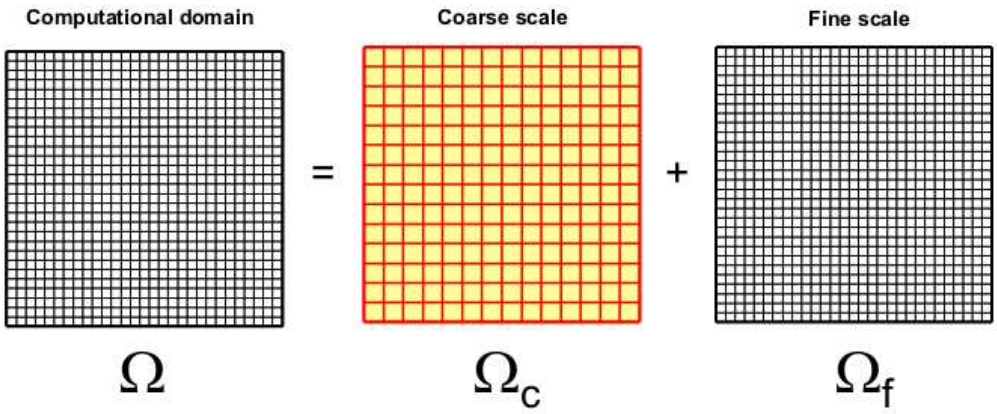

Figure 78: Interpretation of the scales in the model

$$\begin{aligned} \bar{\mathbf{u}} &= \mathbf{N}\,\mathbf{d} \\ \mathbf{u}' &= \mathbf{Q}\,\mathbf{q} \end{aligned} \tag{169}$$

with $\mathbf{u}'$ being usually referred to as the "enrichment" part of the solution. According to eq. (169), eq. (168) can be shortly rearranged as

$$\mathbf{u} = \bar{\mathbf{u}} + \mathbf{u}' \tag{170}$$

As stated above, $\mathbf{N}$ interpolates the displacements of the coarse scale on the nodes belonging to the mesh of the fine scale. If $\bar{\mathbf{u}}_i$ represents the interpolation of the coarse-scale FE solution $\mathbf{d}_j$ at a fine-scale nodal location $\mathbf{x}_i$ through the coarse-scale shape function $\mathbf{N}_j(\mathbf{x}_i)$, the following stands:

$$\bar{\mathbf{u}}_i = \sum_{I=1}^{n_c} \mathbf{N}_j(\mathbf{x}_i)\,\mathbf{I}_{nD}\mathbf{d}_j \tag{171}$$

where $\mathbf{I}_{nD}$ is the identity matrix of order n_D. Isolating the contributions from the different shape functions, $\mathbf{N}$ can be expanded to read:

$$\mathbf{N} = \begin{bmatrix} \mathbf{N}_1(\mathbf{x}_1)\mathbf{I}_{nD} & \mathbf{N}_2(\mathbf{x}_1)\mathbf{I}_{nD} & \dots & \mathbf{N}_{nc}(\mathbf{x}_1)\mathbf{I}_{nD} \\ \mathbf{N}_1(\mathbf{x}_2)\mathbf{I}_{nD} & \mathbf{N}_2(\mathbf{x}_2)\mathbf{I}_{nD} & \dots & \mathbf{N}_{nc}(\mathbf{x}_2)\mathbf{I}_{nD} \\ \vdots & \vdots & \ddots & \vdots \\ \mathbf{N}_1(\mathbf{x}_{nf})\mathbf{I}_{nD} & \mathbf{N}_2(\mathbf{x}_{nf})\mathbf{I}_{nD} & \dots & \mathbf{N}_{nc}(\mathbf{x}_{nf})\mathbf{I}_{nD} \end{bmatrix} \tag{172}$$

A full derivation for matrix $\mathbf{Q}$ is reported in details by Liu et al. [38] and is summarized in Appendix C.

5.2.2 Multi-scale equations of motion

One possible way to derive equations of motion for the domain of fig. 78 is through Lagrange's equations. The kinetic and potential energies of the system are:

$$\begin{aligned} T &= \frac{1}{2}\,\dot{\mathbf{u}}^T\mathbf{M}_f\dot{\mathbf{u}} \\ U &= \frac{1}{2}\,\mathbf{u}^T\mathbf{K}_f\mathbf{u} \end{aligned} \tag{173}$$

where $\mathbf{K}_f$ is the stiffness matrix of the fine scale, whereas $\mathbf{M}_f$ is the lumped mass matrix of the fine scale. The lumped mass matrix can be easily derived from the consistent mass matrix of the fine scale by means of the row sum technique [5]. Substituting eq. (168) into eq. (173), the expressions for T and U become

$$\begin{aligned} T &= \frac{1}{2}\,\left(\dot{\mathbf{d}}^T\mathbf{N}^T\mathbf{M}_f\mathbf{N}\dot{\mathbf{d}} + \dot{\mathbf{d}}^T\mathbf{N}^T\mathbf{M}_f\mathbf{Q}\dot{\mathbf{q}} + \dot{\mathbf{q}}^T\mathbf{Q}^T\mathbf{M}_f\mathbf{N}\dot{\mathbf{d}} + \dot{\mathbf{q}}^T\mathbf{Q}^T\mathbf{M}_f\mathbf{Q}\dot{\mathbf{d}}\right) \\ U &= \frac{1}{2}\,\left(\mathbf{d}^T\mathbf{N}^T\mathbf{K}_f\mathbf{N}\mathbf{d} + \mathbf{d}^T\mathbf{N}^T\mathbf{K}_f\mathbf{Q}\mathbf{q} + \mathbf{q}^T\mathbf{Q}^T\mathbf{K}_f\mathbf{N}\mathbf{d} + \mathbf{q}^T\mathbf{Q}^T\mathbf{K}_f\mathbf{Q}\mathbf{d}\right) \end{aligned} \tag{174}$$

where the coupling between the scales through the bridging matrices is clearly visible. Substituting eq. (174) into the general form of Lagrange's equations for a conservative system

$$\frac{d}{dt}\left(\frac{\partial L}{\partial \dot{\mathbf{u}}}\right) - \frac{\partial L}{\partial \mathbf{u}} = \mathbf{f}^E \tag{175}$$

where $\mathbf{f}^E$ is the array of the generalized forces and where the Lagrangian L is defined as

$$L = T - U \tag{176}$$

The resulting equations of motion are:

$$\mathbf{M}_f\ \ddot{\mathbf{q}} = -\mathbf{K}_f\left(\mathbf{N}\mathbf{d} + \mathbf{Q}\mathbf{q}\right) + \mathbf{f}^E \tag{177}$$

$$\mathbf{M}\ \ddot{\mathbf{d}} = \mathbf{N}^T\left[-\mathbf{K}_f\left(\mathbf{N}\mathbf{d} + \mathbf{Q}\mathbf{q}\right) + \mathbf{f}^E\right] \tag{178}$$

where the consistent mass matrix $\mathbf{M}$ for the coarse-scale mesh is defined as

$$\mathbf{M} = \mathbf{N}^T\mathbf{M}_f\mathbf{N} \tag{179}$$

and the following identities have been used [38]

$$\begin{aligned} \mathbf{Q}^T\mathbf{M}_f\mathbf{Q} &= \mathbf{Q}^T\mathbf{M}_f \\ \mathbf{Q}^T\mathbf{M}_f\mathbf{N} &= \mathbf{N}^T\mathbf{M}_f\mathbf{Q} \\ \mathbf{Q}^T\mathbf{K}_f\mathbf{N} &= \mathbf{N}^T\mathbf{K}_f\mathbf{Q} \end{aligned} \tag{180}$$

By making use again of eq. (168), the equations of motion can be recast in the following compact form:

$$\mathbf{M}_f\ddot{\mathbf{q}} = -\mathbf{K}_f\mathbf{u} + \mathbf{f}^E \tag{181}$$

$$\mathbf{M}\ddot{\mathbf{d}} = -\mathbf{N}^T\left[\mathbf{K}_f\mathbf{u} + \mathbf{f}^E\right] \tag{182}$$

The two equations of motion are coupled, as $\mathbf{u}$ carries information from both scales. A time dependent solution of these equations can be obtained with a two-scale time integration scheme. At the n^{th} time step along the coarse-scale time domain a coarse-scale solution is calculated from eq. (182). The coarse-scale solution is then used in eq. (181) which is integrated on a fine-scale time domain from the n^{th} to the $(n+1)^{th}$ coarse-scale step.

5.2.3 Partition of the equations of motion and reduction of the degrees of freedom

The procedure highlighted in the previous paragraph offers a formal representation of the dynamics of a structure projected onto two meshes. Equations (181) and (182) also offer some insight on the relationship between elastic and inertial operators that are developed within different discretization schemes. However, as presented above, the technique reduces to a pure academic exercise, since the same result could be achieved by simply calculating the motion in the two scales independently. The advantage offered by the bridging scales technique becomes evident in the case of a problem like the one of fig. 79, where the main interest is the local behavior of a small region within the entire domain. In this context, the domain is partitioned into two regions $\Omega_f^{(a)}$ and $\Omega_f^{(b)}$, with $\Omega_f^{(a)}$ representing the portion of the domain where a detailed description of the phenomenon under consideration is needed, while $\Omega_f^{(b)}$ is the remaining part of the structure. The fine-scale simulation is to be performed over Ω_f only as if this were a completely independent elastic domain. A set of forces needs

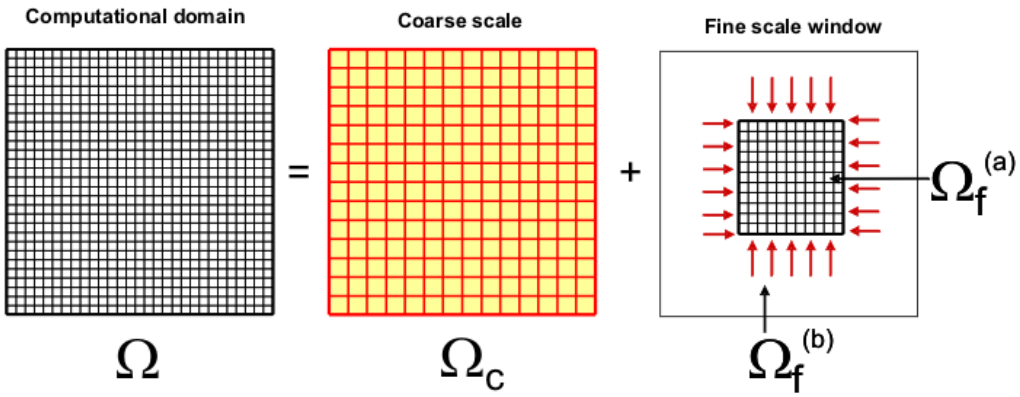

Figure 79: Bridging model for a non-trivial situation

to be applied along the boundaries of $\Omega_f^{(a)}$ to account for the elastic interactions with the neighboring portion of the domain. The partition of the elastic domain corresponds to the following partition of the array of fine-scale degrees of freedom:

$$\mathbf{q} = [\mathbf{q}_a \;\; \mathbf{q}_b]^T \tag{183}$$

where $\mathbf{q}_a$ represents the degrees of freedom that we intend to retain in the fine-scale calculations and $\mathbf{q}_b$ contains the degrees of freedom to be eliminated in order to effectively reduce the fine-scale analysis to the sole internal window. The array of coarse-scale nodal degrees of freedom $\mathbf{d}$ can be also decomposed as

$$\mathbf{d} = [\mathbf{d}_a \;\; \mathbf{d}_b]^T \tag{184}$$

Accordingly, a partition of the fine-scale stiffness matrix and lumped mass matrix is introduced as

$$\mathbf{K}_f = \begin{bmatrix} \mathbf{K}_f^{aa} & \mathbf{K}_f^{ab} \\ \mathbf{K}_f^{ba} & \mathbf{K}_f^{bb} \end{bmatrix} \tag{185}$$

$$\mathbf{M}_f = \begin{bmatrix} \mathbf{M}_f^{aa} & \mathbf{0} \\ \mathbf{0} & \mathbf{M}_f^{bb} \end{bmatrix} \tag{186}$$

where $\mathbf{M}_f^{aa}$ and $\mathbf{M}_f^{bb}$ are diagonal matrices. By means of the partitioned quantities of eq.s (183), (184), (185) and (186), the equation of motion for the fine scale can be expanded

as

$$\mathbf{M}_f^{(aa)}\ \ddot{\mathbf{q}}_a = -\mathbf{K}_f^{(aa)}\ \mathbf{q}_a - \mathbf{K}_f^{(ab)}\bar{\mathbf{u}}_b - \mathbf{K}_f^{(ab)}\mathbf{u'}_b + \mathbf{f}^E \tag{187}$$

The following quantity can be introduced to express the interface forces acting along the contour of the fine-scale region

$$\mathbf{f}^I = -\mathbf{K}_f^{(ab)}\mathbf{u'}_b \tag{188}$$

where $\mathbf{u}'_b$ is the enrichment part of the nodal values outside the fine-scale window. Equation (187) can then be recast as

$$\mathbf{M}_A^{(aa)}\ \ddot{\mathbf{q}}_a = -\mathbf{K}_f^{(aa)}\ \mathbf{q}_a - \mathbf{K}_f^{(ab)}\bar{\mathbf{u}}_b + \mathbf{f}^I + \mathbf{f}^E \tag{189}$$

Equation (189) also offers some insight on the mechanism through which the coupling between the scales is achieved. It is in fact clearly visible that the quantity $\mathbf{d}$ containing contributions from the coarse scale is included in the fine-scale equation through the interpolation matrix $\mathbf{N}$. The expression of eq. (189) and therefore of the system of eq.s (181) and (182) requires the calculation of $\mathbf{u}'_b$ in terms of $\mathbf{q}_a$. As $\mathbf{K}_f^{(ab)}$ has non-zero entries only in the rows corresponding to the nodes on the interfaces between $\Omega_f^{(a)}$ and $\Omega_f^{(b)}$, only the displacements $\mathbf{u}'_b$ adjacent to the nodes on the interface contribute to eq. (189). The following paragraph describes the technique to express $\mathbf{u}'_b$ in terms of $\mathbf{q}_a$.

5.2.4 Transforms into the wavenumber space and the Laplace space

Let us consider, for reference, a two-dimensional regular mesh with four-node quadrilateral elements as depicted in fig. 80. The spatial location of the nodes within the mesh is expressed through the integer pair (n, m). In this example we are considering the vertical interface corresponding to $n = 0$ and the nodes to be eliminated are located to the right of this line. Similar considerations can be made for other interfaces with minor differences in the procedure. For this analysis, focus is placed on on the enrichment part $\mathbf{u}'_{n,m}$ only. Let us denote $\mathbf{u}'_{0,m}$ and $\mathbf{u}'_{1,m}$ the enrichment component of the generalized displacements of nodes along the interface and those immediately outside the interface respectively. Our objective is to express the enrichment terms $\mathbf{u}'_{1,m}$ in terms of those of the interface $\mathbf{u}'_{0,m}$. Let us write the equations of motion for the single finite element the (n, m) node belongs to. Denoting

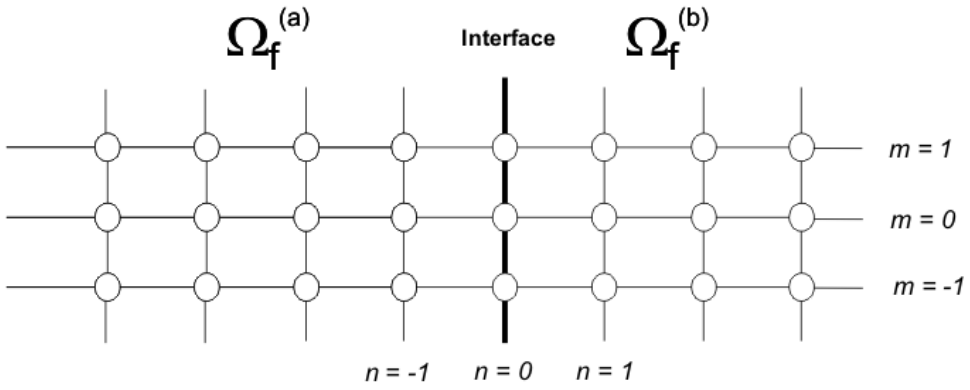

Figure 80: Schematic for nodes elimination technique at the interface

as $\mathbf{K}_f^{(e)}$ and $\mathbf{M}_f^{(e)}$ the elemental stiffness and lumped mass matrices of the element, the equation of motion for node (n, m) can be expressed as

$$\mathbf{m}_f \ \ddot{\mathbf{u}}'_{n,m}(t) = -\sum_{m'=m-1}^{m+1} \sum_{n'=n-1}^{n+1} \mathbf{K}_{n-n',m-m'} \mathbf{u}'_{n',m'}(t) + \mathbf{f}^c_{n,m}(t) \tag{190}$$

where $\mathbf{m}_f$ is the diagonal block inside $\mathbf{M}_f^{(e)}$ relative to the (n, m) node and $\mathbf{f}^c_{n,m}(t)$ is the external force acting on that node. The two-dimensional discrete Fourier transform (DFT) of a function f is defined as:

$$\hat{f}(\xi_1, \xi_2) = \mathcal{F}_{n,m \longrightarrow \xi_1,\xi_2}(f_{n,m}) = \sum_{n=-\frac{N}{2}+1}^{\frac{N}{2}} \sum_{m=-\frac{M}{2}+1}^{\frac{M}{2}} f_{n,m} e^{-i(n\xi_1 + m\xi_2)} \tag{191}$$

where $f_{n,m}$ is the value of f evaluated at node (n, m), N and M are the total number of nodes in the domain along directions x and y respectively and ξ_1 and $\xi_2 \in [-\pi, \pi]$ are the components of the wave vector along those directions defined by

$$\xi_1 = \frac{2\pi p}{N} \ , \ \xi_2 = \frac{2\pi q}{M} \tag{192}$$

with p and q being two integers. Likewise, the inverse two-dimensional discrete Fourier transform (IDFT) can be written as

$$f_{n,m} = \mathcal{F}^{-1}_{\xi_1,\xi_2 \longrightarrow n,m}(\hat{f}(\xi_1, \xi_2)) = \frac{1}{NM} \sum_{p=-\frac{N}{2}+1}^{\frac{N}{2}} \sum_{q=-\frac{M}{2}+1}^{\frac{M}{2}} \hat{f}(\xi_1, \xi_2) e^{i(n\xi_1 + m\xi_2)} \tag{193}$$

Taking the DFT of eq. (190) yields

$$\mathbf{m}_A \ \ddot{\hat{\mathbf{u}}}'(\xi_1, \xi_2, t) = -\hat{\mathbf{K}}(\xi_1, \xi_2)\hat{\mathbf{u}}'(\xi_1, \xi_2, t) + \hat{\mathbf{f}}_0(\xi_2, t) \tag{194}$$

where $\hat{\mathbf{K}}$ is the stiffness matrix expressed in the Fourier domain whose derivation was detailed in Chapter II. Equation (194) is also transformed into the Laplace domain to obtain

$$\ddot{\hat{\mathbf{U}}}'(\xi_1, \xi_2, s) = \hat{\mathbf{G}}(\xi_1, \xi_2, s)\mathbf{m_A}^{-1}\hat{\mathbf{F}}_0(\xi_2, s) \tag{195}$$

where the assumption of zero nodal displacements and zero nodal velocities at $t = 0$ is made. The quantity $\hat{\mathbf{G}}(\xi_1, \xi_2, s)$ in eq. (195) assumes the expression

$$\hat{\mathbf{G}}(\xi_1, \xi_2, s) = \left[s^2\mathbf{I} + \mathbf{m_A}^{-1}\hat{\mathbf{K}}^e(\xi_1, \xi_2)\right]^{-1} \tag{196}$$

Recalling the terminology introduced in Chapter II, the quantity $\hat{\mathbf{G}}(\xi_1, \xi_2, s)$ in eq. (196) can be interpreted as the symbol of the structure in the Fourier domain. The following analysis involves the mathematical manipulations aiming at bringing the result of eq. (195) back into the physical space-time domain. First, the inverse Fourier transform along the x direction of eq. (195) is taken and evaluated both for a node at the interface ($n = 0$) and for the node immediately to its right ($n = 1$). The two quantities are then related to each other to obtain:

$$\hat{\mathbf{U}}_1'(\xi_2, s) = \tilde{\mathbf{G}}_1(\xi_2, s)\tilde{\mathbf{G}}_0^{-1}(\xi_2, s)\hat{\mathbf{U}}_0'(\xi_2, s) \tag{197}$$

where the notation $\tilde{()}$ denotes quantities that have been inverse-transformed. Taking the inverse Laplace transform of the quantity $\tilde{\mathbf{G}}_1(\xi_2, s)\tilde{\mathbf{G}}_0^{-1}(\xi_2, s)$ yields

$$\tilde{\boldsymbol{\theta}}(\xi_2, t) = \mathcal{L}^{-1}\left[\tilde{\mathbf{G}}_1(\xi_2, s)\tilde{\mathbf{G}}_0^{-1}(\xi_2, s)\right] \tag{198}$$

Likewise, the inverse Laplace transform of $\hat{\mathbf{U}}'(\xi_2, s)$ from eq. (197) in terms of $\tilde{\boldsymbol{\theta}}(\xi_2, t)$ is given through the convolution integral

$$\tilde{\mathbf{u}}_1'(q, t) = \int_0^t \tilde{\theta}(\xi_2, t - \tau)\tilde{\mathbf{u}}_0'(\xi_2, \tau)d\tau \tag{199}$$

A second application of the inverse discrete Fourier transform along the y direction to $\tilde{\boldsymbol{\theta}}(\xi_2, t)$ yields

$$\boldsymbol{\theta}_m(t) = \mathcal{F}_{q\longrightarrow m}^{-1}\tilde{\boldsymbol{\theta}}(\xi_2, t) \tag{200}$$

Finally, the variation with time of the enrichment of the displacement for the eliminated node at $(n = 1, \forall m)$ gives

$$\mathbf{u'}_{1,m}(t) = \sum_{m'=m-\frac{M}{2}+1}^{m+\frac{M}{2}} \int_0^t \boldsymbol{\theta}_{m-m'}(t-\tau)\mathbf{u'}_{0,m'}(\tau)d\tau \tag{201}$$

The quantity $\boldsymbol{\theta}_m(t)$ is called the *time history kernel function* of the problem. Calculating $\boldsymbol{\theta}_m(t)$ is often a non-trivial task as it requires taking the Laplace Transform in eq. (198), which represents a challenging mathematical operation. Only in a limited number of situations it is possible to perform the inverse transform of eq. (198) analytically. More often it becomes necessary to perform it numerically. Among the methods available for this purpose, the method of Weeks [90, 91] has been identified as effective in terms of accuracy and speed. In conclusion, it is fair to say that the calculation of the time kernel history of a structure represents the pivotal operation of the bridging multi-scale technique. The last step required in the procedure is replacing, under the assumptions stated above, $\mathbf{u'}_b$ with $\mathbf{u'}_{1,m}(t)$ and plugging it into eq. (188) to obtain the complete final form of the fine-scale equation of motion

$$\mathbf{M}_A^{(aa)}\ \ddot{\mathbf{q}}_a = -\mathbf{K}_f^{(aa)}\ \mathbf{q}_a - \mathbf{K}_f^{(ab)}\mathbf{N}\mathbf{d} + \sum_{m'=m-\frac{M}{2}+1}^{m+\frac{M}{2}} \int_0^t \boldsymbol{\theta}_{m-m'}(t-\tau)\mathbf{u'}_{0,m'}(\tau)d\tau + \mathbf{f}^E \tag{202}$$

The iterative procedure for the coupled integration over the coarse and fine-scale meshes is illustrated in the flow-chart of fig. 81, where the fine-scale update is now calculated according to eq. (202), while the coarse scale is still handled by eq. (182).

Sections containing sample applications of the bridging multi-scale technique follow. Their purpose is to show how the technique can be implemented in simple cases and to highlight some of the advantages that the procedure offers.

5.3 Application to a One-dimensional Rod

5.3.1 Definition of the problem

The first example considers the propagation of axial waves through the one-dimensional (1D) system of fig. 82. The system is a rod whose inertial and stiffness properties are represented by concentrated parameters k and m of an equivalent spring-mass model. For

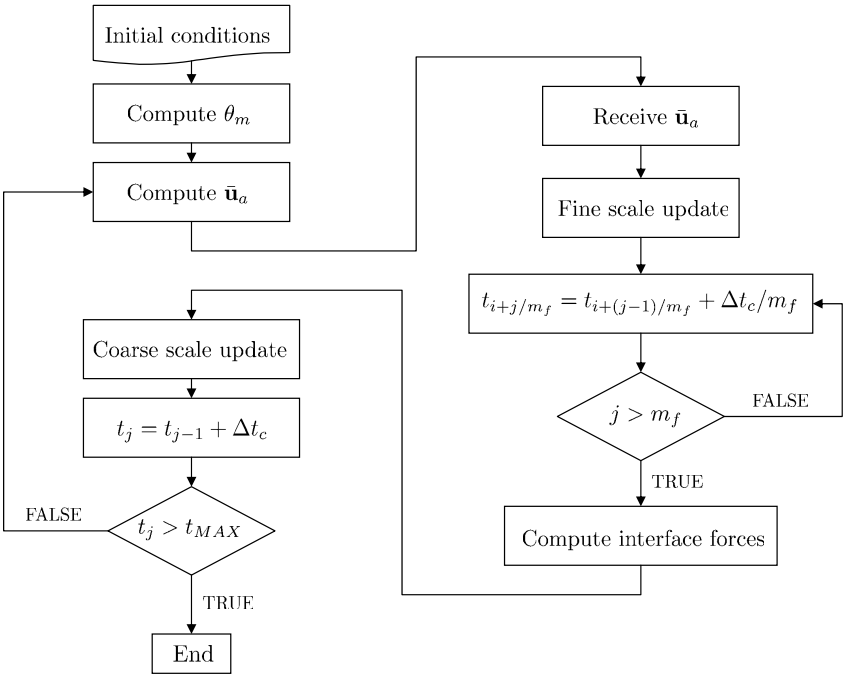

Figure 81: Flow-chart of the double scale time marching scheme

simplicity, free-free boundary conditions are imposed at the ends of the structure. Two

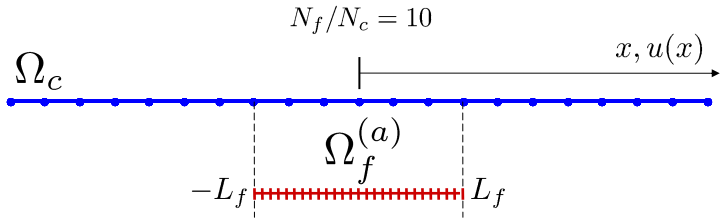

Figure 82: Schematic for one-dimensional case

meshes are considered on the domain. The coarse-scale mesh is defined over the entire length of the rod, while the fine-scale mesh is limited over the central portion of the rod for $x \in [-L_f \; L_f]$. The two meshes are selected such that

$$\frac{N_f}{N_c} = 10 \tag{203}$$

where N_c and N_f are the number of coarse-scale elements and fine-scale elements in the whole structure domain, respectively. An initial disturbance is applied in the form of a

Gaussian distribution of axial displacements about $x = 0$ (see fig. 83):

$$u(x, t = 0) = u_0 e^{-\left(\frac{x - L_f}{\sigma}\right)^2} \tag{204}$$

where u_0 is the amplitude of the imposed displacement and σ the standard deviation of the Gaussian distribution. According to classical wave propagation theory, the disturbance is

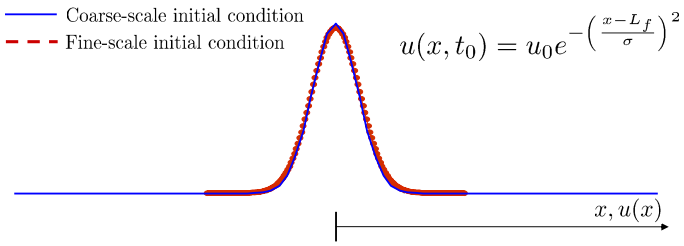

Figure 83: Initial condition expressed in the two scales

expected to travel towards the ends of the structure, be reflected at the free ends and travel back towards the source without altering its shape. In this case, the time kernel history function θ can be obtained analytically [89] as:

$$\hat{G}(\xi, s) = \frac{1}{s^2 + \frac{2k}{m}(1 - \cos\xi)} \tag{205}$$

where eq. (205) corresponds to eq. (196) for a one-dimensional domain. The time history kernel function for the system is then found as:

$$\theta(t) = \mathcal{L}^{-1}\left[\frac{\tilde{G}_1(s)}{\tilde{G}_0(s)}\right] = \frac{2}{t} J_2(2\omega_n t) \tag{206}$$

where J_2 is the second-order Bessel function and

$$\omega_n = \sqrt{\frac{k}{m}} \tag{207}$$

The kernel history for this system features a transient phase during which it oscillates about the 0 value and its amplitude decays with time. After about $5 \div 10$ time units the kernel is almost completely damped out [88] (see fig. 84) .

5.3.2 Numerical results

The time integration for the rod problem is carried out over a simulation interval corresponding to the time needed for the wave to travel half the length of the bar twice. A second

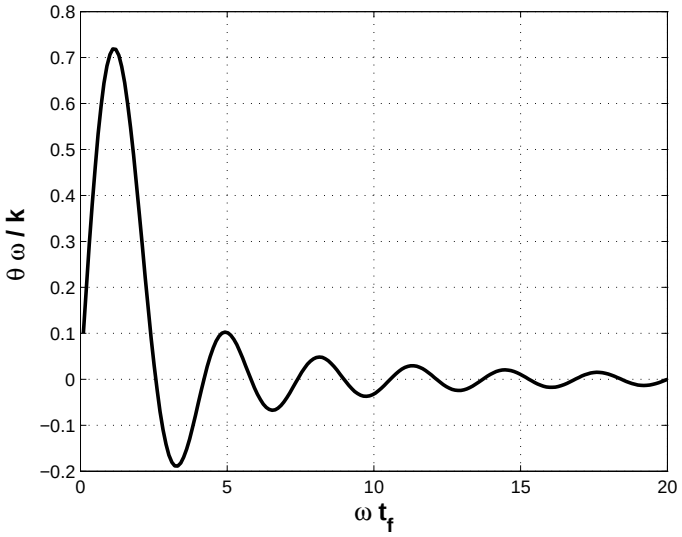

Figure 84: Time history kernel versus normalized fine-scale time

order Newmark scheme is selected as the time marching scheme for the integration. The considered rod is $1m$ long, made of aluminum ($E = 7.1e10\,N/m^2$, $\rho = 2700\,kg/m^3$). The initial disturbance is selected such that $\sigma = 0.1$ and $L_f = 0.375m$. Figures 85.a and 85.b show the calculated wavefield versus time and space. Figure 85.a shows the coarse-scale representation of the wave travelling over the entire domain. As time marches, the applied disturbance moves towards the external regions of the domain and is reflected. Within the accuracy limits of the numerical model, the plot also shows the expected non-dispersive behavior. When the wave travels across the interface, no spurious traces due to the abrupt change in mesh size are detected. Figure 85.b, on the other hand, shows the same wave projected onto the fine scale mesh in the region of the domain where the fine scale is defined. As expected, no reflection waves are observed at the interface: both the outgoing and the incoming waves travel unperturbed through the interfaces without changes in direction or amplitude.

One way to quantify the accuracy of the bridging multi-scale technique consists in comparing the results with those obtained applying a non-uniform mesh over the whole elastic domain. In such a scenario, the only compatibility between the scales that is enforced is the continuity of displacements between two neighboring elements belonging to different scales

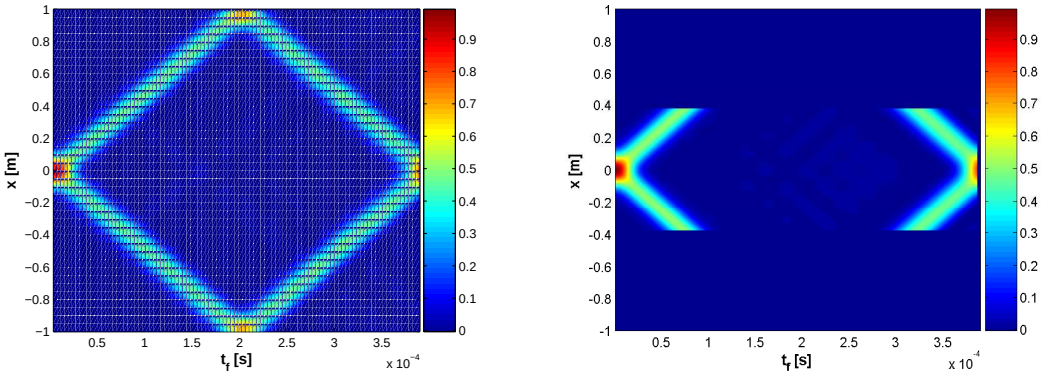

(a) Coarse-scale simulation (b) Fine-scale simulation

Figure 85: Axial wave propagation in a rod

at the shared node. The results of both methods must then be compared with a reference solution, for instance the one obtained through a full refined discretization of the whole structure. The total mechanical energy of the fine-scale region E_{T_f} is selected as a metric for the comparison and is calculated based on the following expression:

$$E_{T_f} = \frac{1}{2}\dot{\mathbf{q}}_a{}^T \mathbf{M}_A^{aa} \dot{\mathbf{q}}_a + \frac{1}{2}\mathbf{q}_a^T \mathbf{K}_f^{aa} \mathbf{q}_a + \mathbf{f}^I{}^T \mathbf{q}_a \tag{208}$$

where $\mathbf{f}^I$ are the interface forces. In fig. 86, the total mechanical energy normalized by its value at $t = 0$ (E_n) is plotted against the first half of the fine-scale interval for the mesh layouts. It can be observed that, without a proper bridging of the scales, some spurious energy is left inside the system when the wave propagates through the interface. This residue energy is associated with the energy carried by spurious reflective waves that are generated at the interface when the proper impedance force is not accounted for in the model. On the contrary, the energy curve for the bridging multi-scale model matches the reference one obtained with a detailed FE analysis.

5.4 Homogenized Bi-material Rod with Imperfections

5.4.1 Definition of the problem

The structure depicted in fig. 87 consists of a periodic sequence of unit cells with two materials. A first order approximation of the dynamic behavior of the rod can be obtained

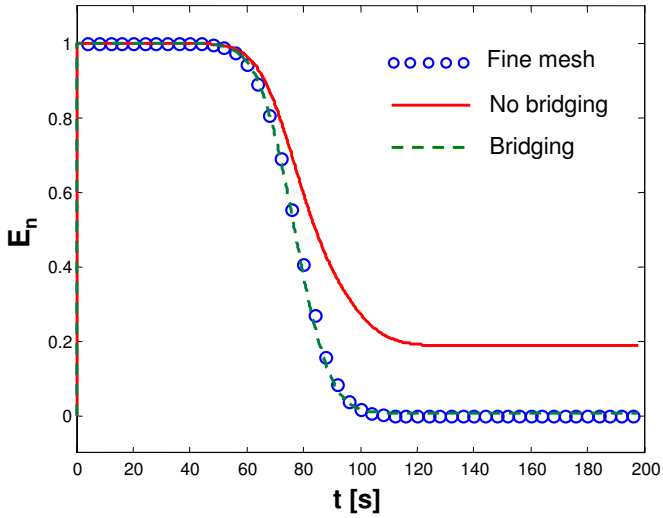

Figure 86: Analysis of the variation of the total mechanical energy of the fine-scale window by means of different models

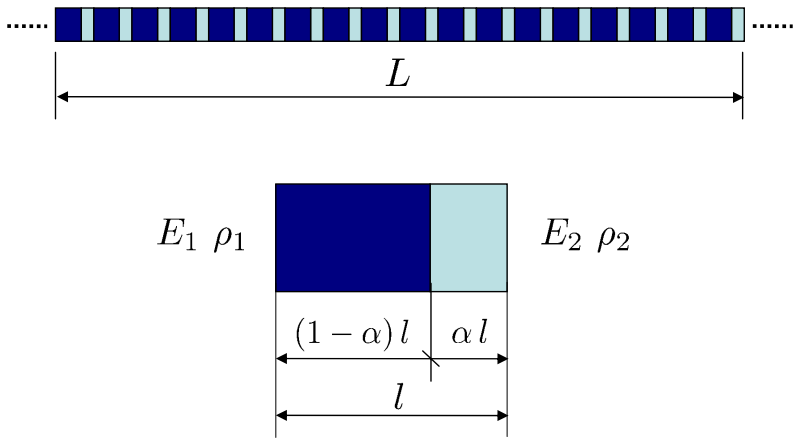

Figure 87: One-dimensional periodic domain

by considering equivalent properties defined by the following rule of mixtures (Chapter II):

$$\begin{aligned} \rho_H A &= (m_1 + m_2) \\ E_H A &= \frac{k_1 k_2}{k_1 + k_2} \end{aligned} \tag{209}$$

where

$$\begin{aligned} k_1 = \tfrac{E_1 A}{\alpha}, \qquad k_2 = \tfrac{E_2 A}{(1-\alpha)} \\ m_1 = \rho_1 A \alpha, \quad m_2 = \rho_2 A (1-\alpha) \end{aligned} \tag{210}$$

The definition of the FE meshes used for this problem is shown schematically in fig. 88. A detailed fine-scale mesh is applied to the central region of the rod and accounts for the alternation of material phases over one cell of the structure. The discontinuity is modelled by reducing the Young's modulus associated with one layer in the bi-material pattern ($E_{def} = 0.025E$). This representation can be regarded as a crude modelization of a crack or soft inclusion. As shown in the schematic of fig. 88.a, the position of the fine-scale window is chosen such that the defect falls within the region where a detailed description of the medium is available. For this example, the discontinuity is introduced at $x = 0.22$. Alongside the detailed problem, an equivalent rod featuring the derived homogeneous properties E_H and ρ_H is discretized with a lower number of bar elements. The model also features a localized

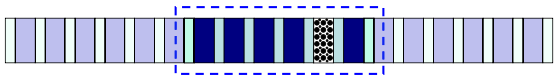

(a) Fine-scale region

(b) Coarse-scale discretization

Figure 88: Definition of coarse and fine meshes for a bi-material rod

discontinuity, as schematically shown in fig. 88.a.

5.4.2 Simulation results

Figures 89.a and 89.b show the propagating wave plotted versus time and space as calculated from the coupled multi-scale analysis. The presence of the material discontinuity is highlighted by the generation of a reflected wave due to the abrupt change in the impedance

of the materials across the inclusion. It can be noticed how the imperfection is responsible for a time shift in the incident propagating wave but does not affect the speed at which the wave propagates past the discontinuity. The same reflection pattern is featured by the returning wave when it hits the imperfection. The absence of spurious reflections at the interfaces between the meshes allows a straightforward interpretation of the wavefield.

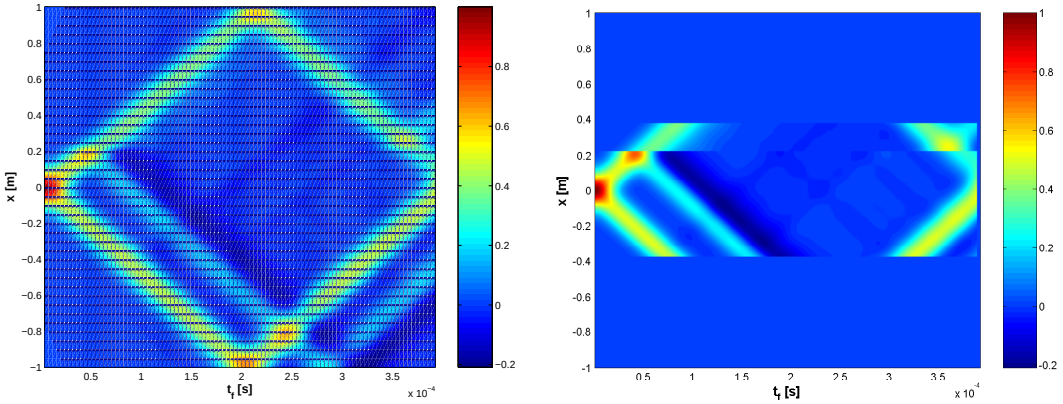

(a) Coarse-scale simulation (b) Fine-scale simulation

Figure 89: Wave propagation in a homogenized rod with localized defect

Two considerations can be made out of the inspection of fig.s 89.a and 89.b to underline the effectiveness of the bridging scales method. First, the plots provide two representations of the same propagating wave with different levels of accuracy. The coarse scale simulation provides a global description of the wave motion in the rod and detects the presence of the damage and therefore the existence of a defect, but fails at offering a high-resolution representation of the generation of the reflection in the neighborhood of the discontinuity. On the contrary, the fine-scale simulation provides an accurate local representation from which details of the reflection generation mechanism can be inferred. Secondly, and most importantly, the size of the damaged area is in most cases (including the example of fig.s 89.a and 89.b) smaller than the size of a single finite element in the coarse scale. Therefore the coarse scale does not model the defect and considers instead the homogeneous properties of eq. (209) applied throughout the rod length.

A slight variation on the previous example is shown in fig.s 90.a and 90.b. In this

case, the region of the rod with reduced stiffness extends over a larger portion of the domain, and can be seen as due the presence of a porous region. This configuration results in a more complex wavefield. Like in the previous example, the low-impedance region

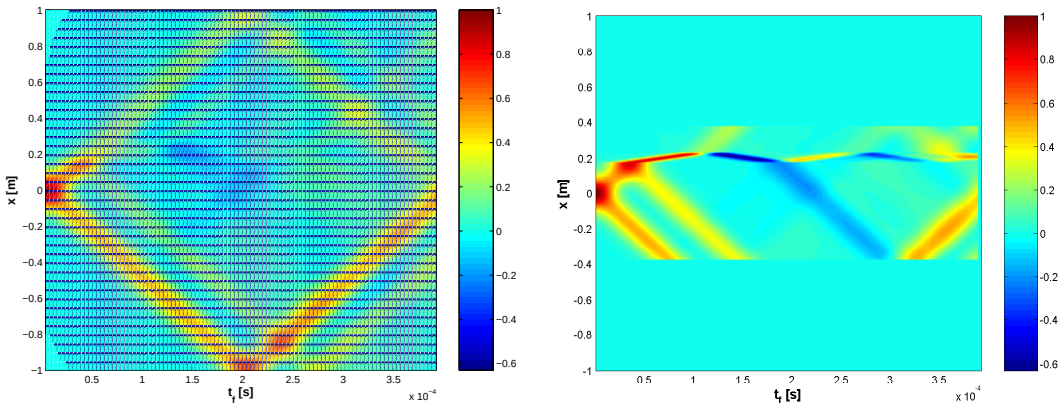

(a) Coarse-scale simulation (b) Fine-scale simulation

Figure 90: Wave propagation in a homogenized rod with wide damaged region

reflects the incoming wave. In addition, the refracted wave propagates in the damaged region at a lower speed due to the lower stiffness of the material. When the wave leaves the damaged area, a second change in the material impedance occurs, the wave regains its original speed, and another reflection is observed at the damage boundary. A chain of internal reflections can also be observed, which produces a standing wave confined to the discontinuity region. While these additional phenomena are standard features due to the increased complexity of the domain, they allow additional considerations about the method. Unlike the previous example, the succession of consecutive reflections inside the damaged area is here accurately shown only in the fine scale representation, while it is barely visible in the coarse scale. This is due to the fact that the internal reflections span over a small region which is discretized with an insufficient number of coarse elements. A more complicated reflection pattern accentuates the difference in performance between the scales. This example tests the capabilities of the bridging scales method, since it involves many more crossings of the scale interfaces. The inspection of fig. 90.b, however, shows that the interface forces are still very effective and no spurious reflections are generated.

5.4.3 Effects of impedance mismatch

It is interesting to note that in this case the fine scale matrices are assembled using the actual material properties of the elements, while the coarse scale considers equivalent or homogenized properties. This results in a certain degree of incompatibility between the two models that is as negligible as the technique used for the homogenization is refined. The mutual transfer of information from one scale to the other generates a contamination of the results that grows with the mismatch between the actual and the homogenized properties of the structure. The impedance mismatch between the materials dominates the validity of the homogenization process and therefore the compatibility between the homogenized model and the original structure. Figure 91 shows the results of simulations for bi-material layouts with increasing mismatch between the properties of the two phases. The total mechanical energy of the fine-scale region is again chosen as the metric for the accuracy of the method and compared with the same quantity calculated with a detailed fine-mesh simulation performed over the elastic domain. The results of this comparison are shown in fig. 91. The energy curves feature considerable agreement during the early stages of the simulation, when the fine-scale integration is carried out from a given initial disturbance applied directly to the fine scale. The reconstruction of the wave returning inside the fine-scale window relies instead on values imported from the coarse scale simulation. These values are affected by errors due to the approximation associated with the averaging technique, therefore the shortcomings of the homogeneous model used for the coarse scale ultimately affect the refined analysis. As expected, the disagreement between the curves grows with the impedance mismatch.

5.4.4 Dependency upon the nature of the excitation

Let us consider different distributions of the initial applied disturbance $u(x, t = 0)$. The changes are made by controlling the parameter σ in the expression for u that represents the standard deviation of the Gaussian curve. Low values of σ correspond to short wavelength disturbances, as opposed to high values of σ which generate spatially smoother signals. The calculated time histories of the fine-scale energy E_{T_f} are shown in fig. 92 for increasing σ.

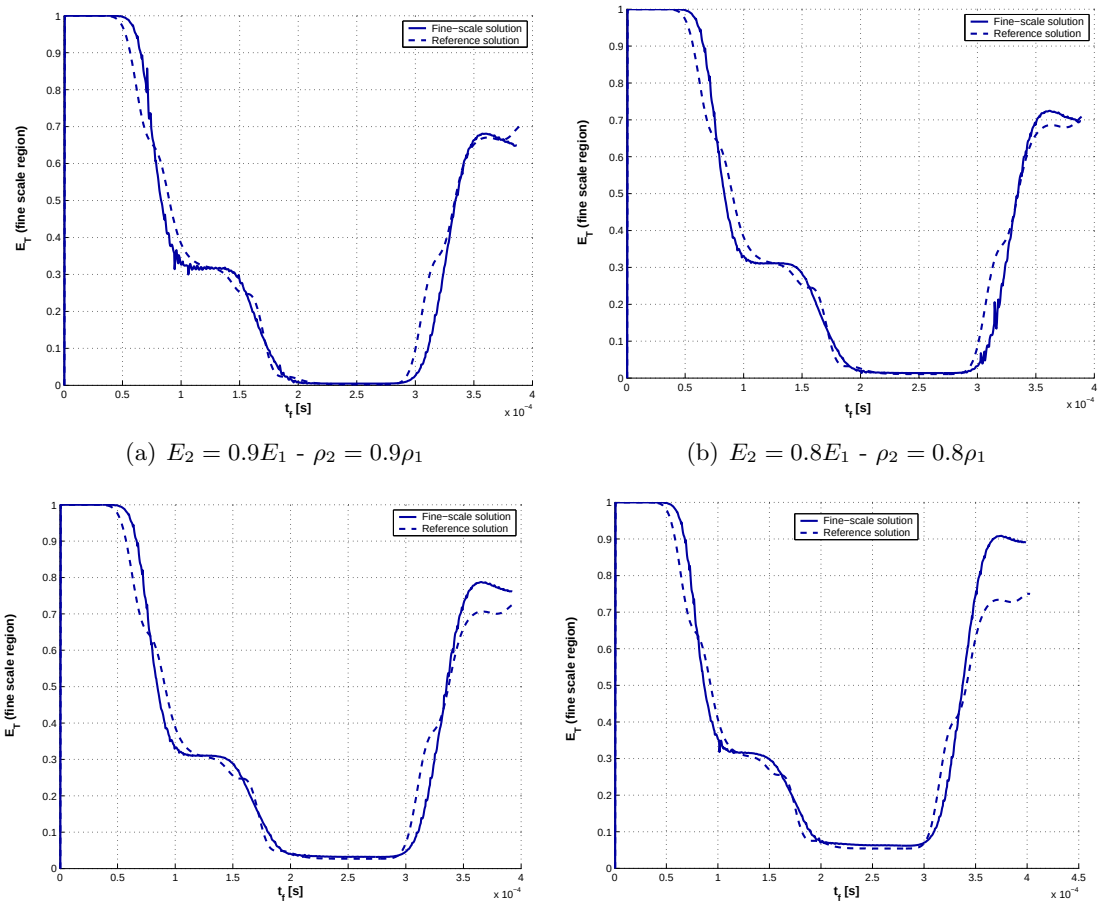

(a) $E_2 = 0.9E_1$ - $\rho_2 = 0.9\rho_1$

(b) $E_2 = 0.8E_1$ - $\rho_2 = 0.8\rho_1$

(c) $E_2 = 0.7E_1$ - $\rho_2 = 0.7\rho_1$

(d) $E_2 = 0.6E_1$ - $\rho_2 = 0.6\rho_1$

Figure 91: Longitudinal and shear velocities from the homogenized model

Inspection of fig. 92 shows a peculiar and somewhat counterintuitive trend in the agreement

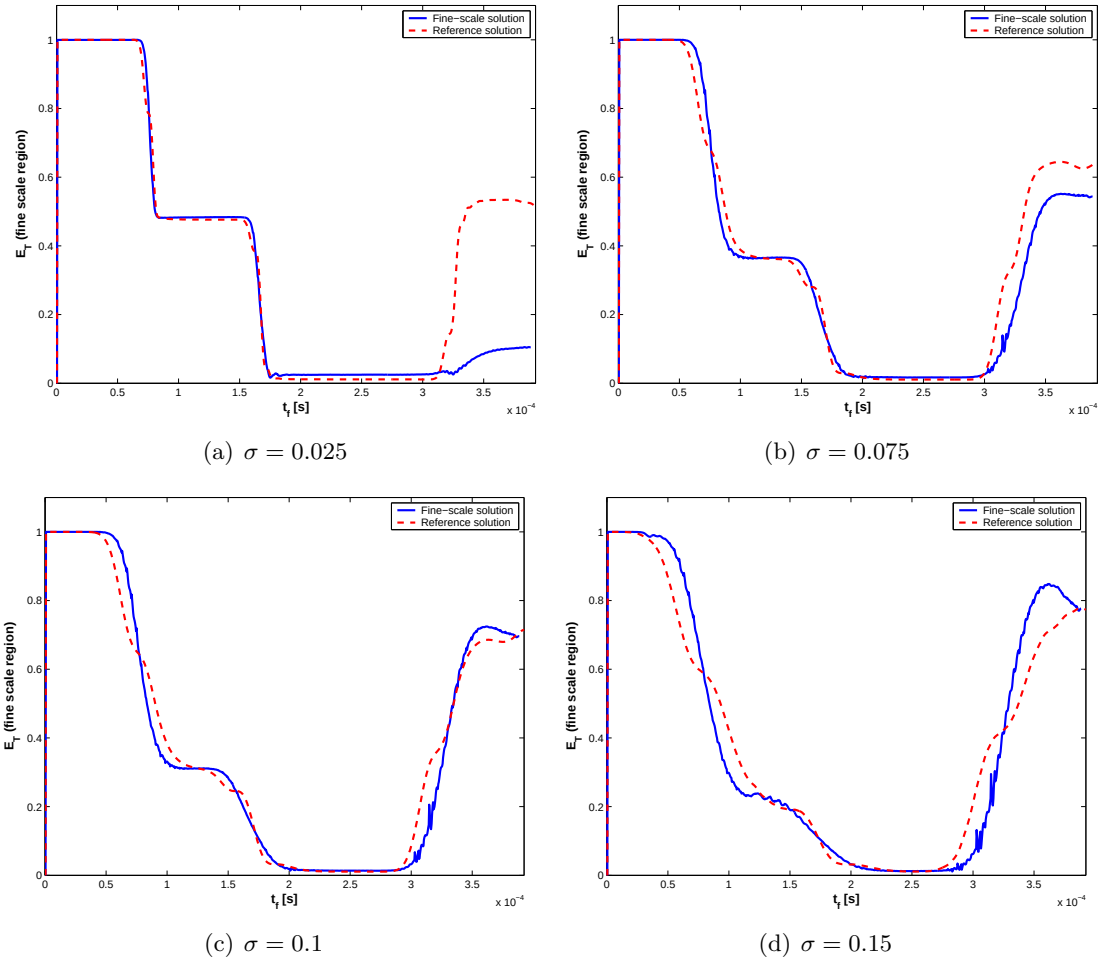

(a) $\sigma = 0.025$ (b) $\sigma = 0.075$

(c) $\sigma = 0.1$ (d) $\sigma = 0.15$

Figure 92: Total mechanical energy for the fine-scale region - BMS method vs. full simulation

with the reference solution. In the case of smooth disturbance (high σ), the agreement is good over the whole interval of simulation: the changes occurring because of the internal reflections due to the defects are properly captured and the residue energy level left in the fine scale window at the end of the simulation coincides with the reference value. In the case of a sharp disturbance (low σ), on the contrary, the agreement becomes very poor when it comes to the returning wave. For $\sigma = 0.025$, the residue energy is underestimated by almost 80% (fig. 92.a). The results of fig. 92 and the comparison with the previous set of results suggest the presence of an incompatibility enhanced by the shape of the excitation. The reasons for this behavior are to be found in the limited validity of the long wavelength

- short wavenumber homogenization used for the derivation of the equations of motion for the coarse scale. The homogenized model provides in fact a good approximation for the behavior of the bi-material rod only in the low frequency regime, according to the discussion of Chapter II. When a localized disturbance is applied to a structure, the structure responds exciting a spectrum of frequencies which is more or less broad according to the nature of the impulse. For example, a sharp impulse, like the one used to generate the results of fig. 92.a is expected to excite higher frequencies than the smooth one of fig. 92.c. Sharp

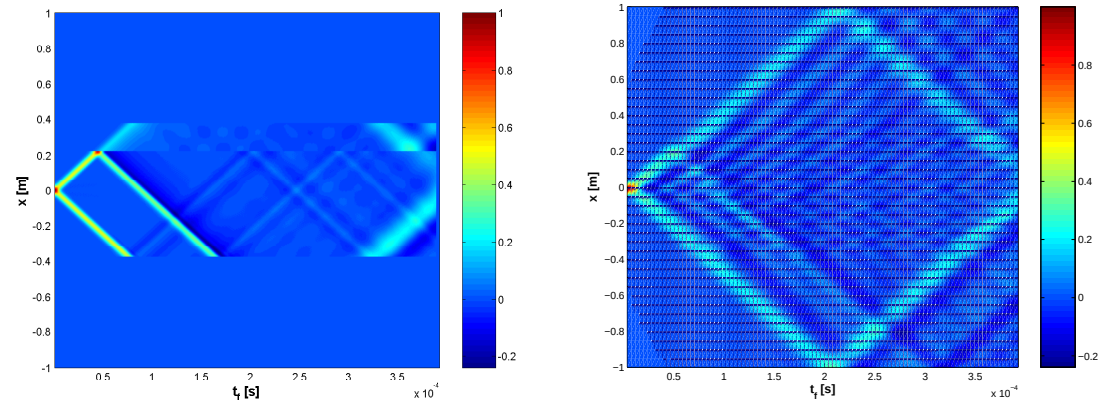

(a) Fine-scale solution - $\sigma = 0.025$

(b) Coarse-scale solution - $\sigma = 0.025$

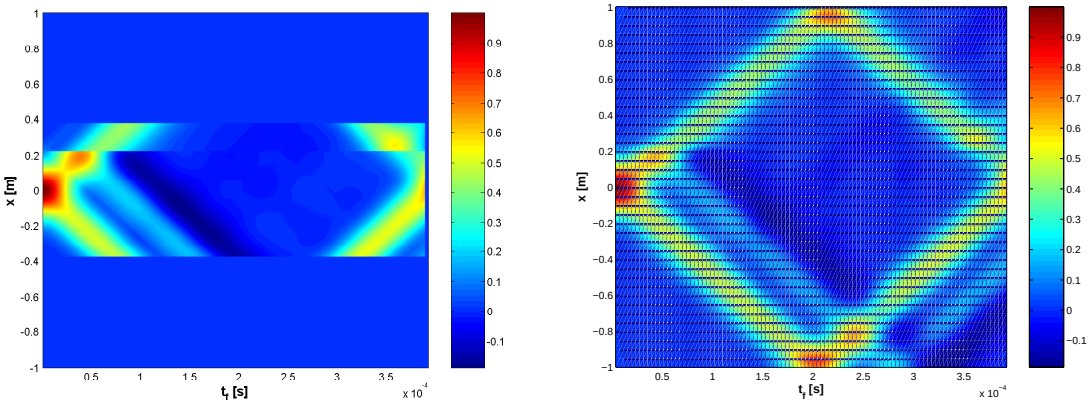

(c) Fine-scale solution - $\sigma = 0.15$

(d) Coarse-scale solution - $\sigma = 0.15$

Figure 93: Fine-scale and coarse-scale solutions for different applied excitations

excitations generate waves whose frequency content is less compatible with the range of applicability of the homogenized model. Ultimately sharp excitations induce a shortcoming in the performance of the coarse scale. This is consistent with the trend of fig. 92, but

Table 2: CPU Time performance of the BMS method on fine meshes of different size

N_f	Full simulation CPU time	Bridging scales CPU time	CPU time saved
400	$28.86\,s$	$25.69\,s$	$11.0\,\%$
450	$36.61\,s$	$27.81\,s$	$24.0\,\%$
500	$45.20\,s$	$29.97\,s$	$33.7\,\%$

still does not explain why it is the fine scale result to be ultimately so deeply affected by the shortcoming. A possible explanation can be argued by looking at fig. 93 where the calculated wave is shown respectively for the $\sigma = 0.025$ and $\sigma = 0.15$ cases. Figures 93.a and 93.c show that, when it comes to the incident wave, the fine scale provides an accurate representation of the wave field for both excitations. However, fig.s 93.b and 93.d reveal a much better performance of the coarse scale simulation in the $\sigma = 0.15$ scenario, in accordance with the argument made above. In the $\sigma = 0.025$ scenario the coarse scale energy deteriorates from the early stages of the integration (fig. 93.b), featuring a wavy behavior typical of the dispersive nature of the bi-material rod at higher frequencies. Finally, the coarse scale solution will eventually contribute the fine scale simulation of the returning wave. For $\sigma = 0.15$ the fine solution, being based on the good result of the coarse solution, is extremely accurate (fig. 93.c), while for $\sigma = 0.035$ the incompatibility of the coexisting representations is responsible for the blurry fine scale wave of fig. 93.a. All of these effects can also be associated with the interpolation procedure required to project the coarse-scale displacements onto the fine-scale mesh at the coarse-fine scale interface, which is carried out through the shape function matrix $\mathbf{N}$ introduced above.

5.4.5 Energy-based time integration scheme

The main motivation for numerical techniques such as the bridging scales method is a reduction in computational cost. The partition of the domain is beneficial since the fine-scale equation of motion involves smaller matrices, which is expected to have dramatic consequences on memory allocation. On the other side, the method has a few downsides that reduce its applicability to a limited number of scenarios. Notably, the interface force generation process involves at each time step a convolution integral calculated from the

initial instant of the simulation. By its own definition, this operation requires an amount of time that increases at each time step. For long simulations, the process can become time consuming and can cause the simulation time to exceed the time needed to conduct a fully detailed simulation involving a fine scale applied over the entire domain. This limitation becomes critical when the fine-scale window and the entire domain are comparable in size. As soon as the global dimension of the domain increases with respect to that of the fine-scale window, the methods begins to pay off. These considerations are summarized in Table 2, where the results of the rod problem are shown for different meshes. For this comparison, an increasing size of the global problem is achieved by varying the number of elements in the detailed fine discretization N_f. The numbers shown in Table 2 are relative to a simulation run in $Matlab^{®}$ on a PC Dell® Dimension 8250 with a $2.78\,GHz$ CPU, and $1.0\,GB$ RAM.

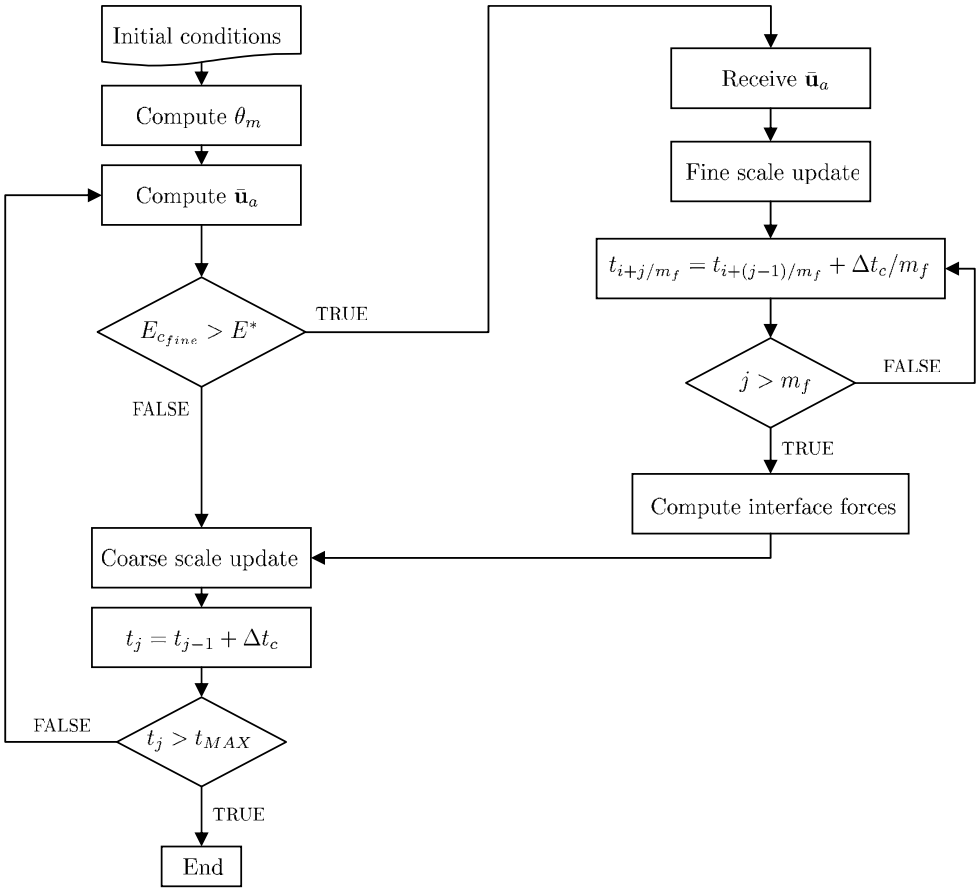

Figure 94: Flow-chart of the energy threshold procedure

Table 3: Effect of an energy threshold on the CPU Time

N_f	Full simulation CPU time	Energy threshold CPU time	CPU time saved
400	$28.86\,s$	$14.30\,s$	$50.5\,\%$
450	$36.61\,s$	$14.95\,s$	$52.2\,\%$
500	$45.20\,s$	$17.58\,s$	$61.1\,\%$

The speed of the method can be enhanced by letting the simulation run on the sole coarse-scale mesh unless the presence of a wave propagating within the fine-scale window is detected. This can be achieved automatically by monitoring the energy level inside the fine-scale window and use it as a threshold to trigger the update of the fine-scale solution. The coarse-scale total mechanical energy calculated on the fine-scale region is an ideal trigger for all phases of the simulation, since it is updated at each time step even when the wave is outside the fine-scale region. A threshold value E^* is selected such that, when $E_{c_{fine}} > E^*$, the algorithm interprets it as a wave travelling inside the fine-scale and the coupled integration is conducted. When the wave moves across the scale interface, the value of $E_{c_{fine}}$ drops below the threshold and only the coarse-scale integration is carried out. When the returning wave travelling back towards the source gets inside the region, the coupled integration is re-established. The procedure is detailed in fig. 94. The performance of the integration with the energy threshold is shown in Table 3 for the same set of simulations of Table 2. By comparison of the two sets of results, it is clear how the threshold on the energy manages to reduce the CPU time in all the considered cases.

5.5 Wave Propagation in a Thin Plate

5.5.1 Problem description

An additional example considers the propagation of plane waves in a free-free suqare plate (fig. 95.a). The plate is 50 cm long, 50 cm wide and 3.5 cm thick. The material is aluminum (Young's modulus $E = 7.1e10\,\frac{N}{m^2}$, density ρ=2.7e3 $\frac{Kg}{m^3}$ and Poisson's ratio $\nu = 0.3$). The system is initially perturbed by imposing a two-dimensional Gaussian distribution of the

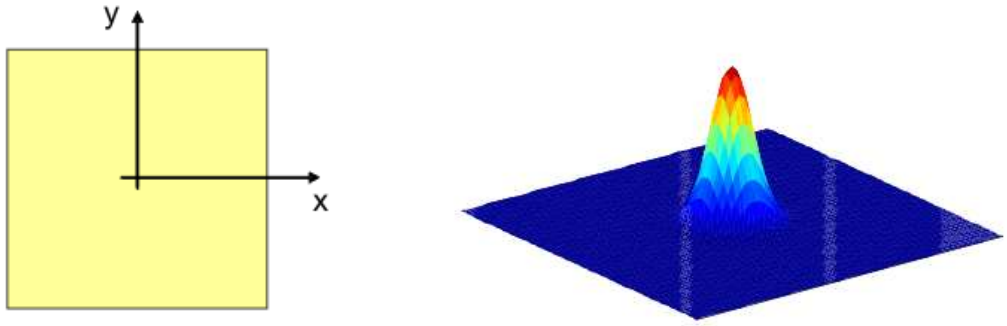

(a) Geometry (b) Initial disturbance

Figure 95: Schematic of a rectangular plate with applied Gaussian in-plane initial disturbance

displacement along the y coordinate (fig. 95.b) defined as:

$$u_y(x,y) = \begin{cases} K\frac{e^{-\left(\frac{d}{\sigma}\right)^2} - u_c}{1-u_c} & d \leq L_c \\ 0 & d > L_c \end{cases} \tag{211}$$

where d is a radial distance from the origin of the reference frame and u_c is a characteristic parameter of the Gaussian curve, respectively defined as:

$$\begin{aligned} d &= \sqrt{x^2 + y^2} \\ u_c &= e^{-\left(\frac{L_c}{\sigma}\right)^2} \end{aligned} \tag{212}$$

K and σ are two additional parameters defining the amplitude and the standard deviation of the Gaussian curve, respectively. A reference solution for this example is obtained through a detailed FE analysis conducted by applying a fine mesh over the entire plate domain. Rectangular 4-node bilinear finite elements are used to discretize the plate. Figure 96 shows a snapshot of the wavefield after $3 \cdot 10^{-5}\, s$ of simulation. By inspection, it is possible to recognize some characteristic features of in-plane wave motion. A pressure wave, for example, is clearly visible travelling along the direction of the disturbance. A shear wave, smaller in amplitude and lagging the pressure wave, can also be observed travelling mostly along the x direction.

Let us now consider the rectangular plate of fig. 95.a. and introduce two meshes: a coarse mesh applied over the entire square domain and a fine mesh confined to a smaller

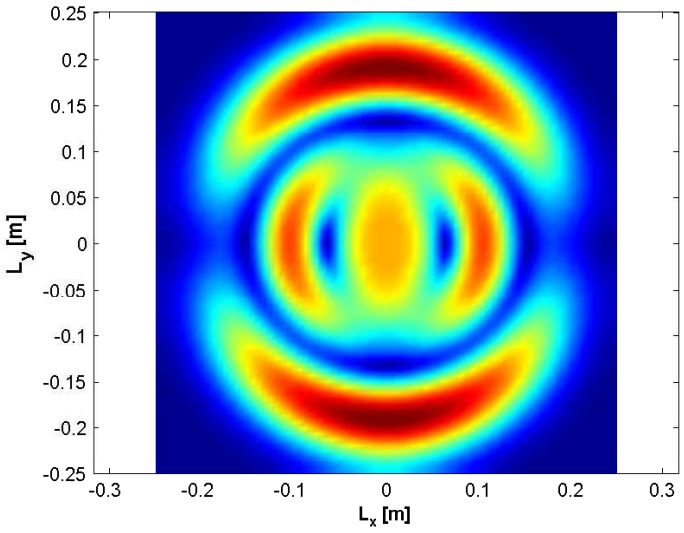

Figure 96: Snapshot of incident travelling wave

rectangular window of size $50 \times 10\,cm$ centered about $x = 0\,m, y = 0.15\,m$. The procedure for the calculation of the time history kernel function is detailed in [38]. Since the nodes in the mesh have two degrees of freedom, at each instant in time $\boldsymbol{\theta}(t)$ is a 2×2 matrix. For reference, fig.s 97.a and 97.b respectively show the behavior of θ_{11} and θ_{22} over the fine-scale simulation time domain for some values of m. Figure 98.a represents a coarse-scale description of the wave propagation over the entire rectangular domain, while fig. 98.b is the fine-scale description of the wavefield within the small rectangular window where the fine mesh is available. Two considerations can be made: first, the fine-scale analysis provides a more detailed representation of the phenomenon, therefore a detailed inspection of a region of the plate is available without solving the full fine-scale problem. Second, the bridging method takes care of the mismatch in mesh size and no spurious reflections are observed.

5.5.2 Effects of a stiff inclusion

In the plate of fig. 95.a a discontinuity is introduced to explore the capability of the method to detect its presence. The discontinuity is modelled as a strip of material with higher density and stiffness to simulate a stiff inclusion. The results of the simulation are shown in

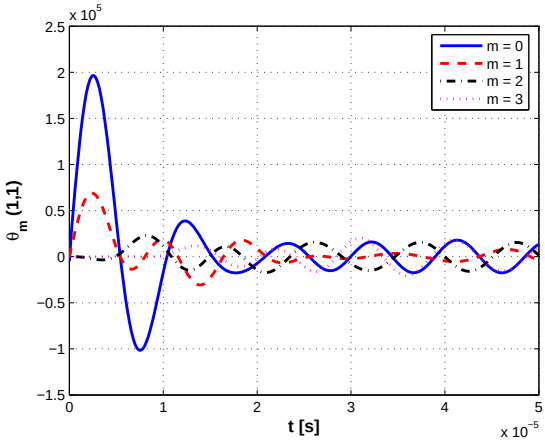

(a) $\theta(1,1)$

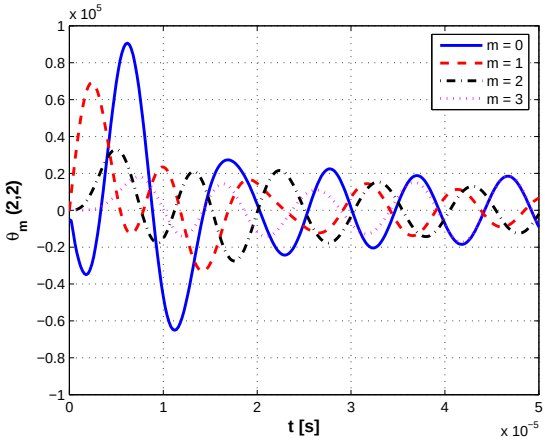

(b) $\theta(2,2)$

Figure 97: Behavior of $\boldsymbol{\theta}(t)$ for different m

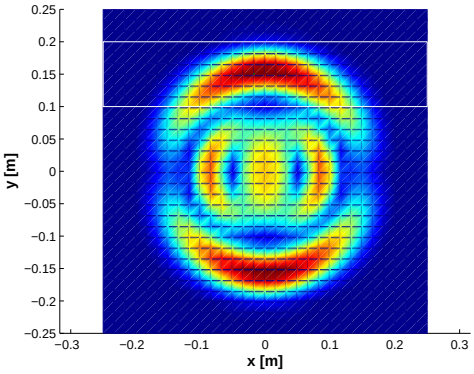

(a) Coarse-scale simulation

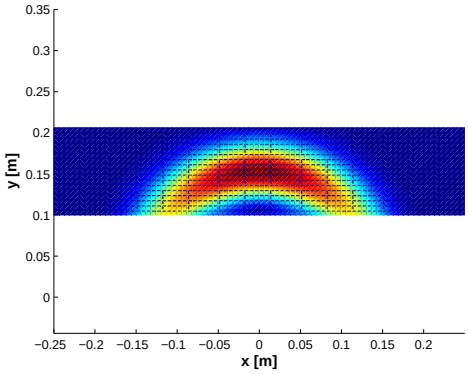

(b) Fine-scale simulation

Figure 98: Snapshot of incident travelling wave

fig. 99.a and fig. 99.b. As in the previous examples, the two scales provide two complementary yet compatible pieces of information about the wave motion. Figure 99.a provides a low-resolution picture of the complete wavefield including both the pressure and shear mode and allows visualization of the wave interaction with the plate boundaries. Figure 99.b

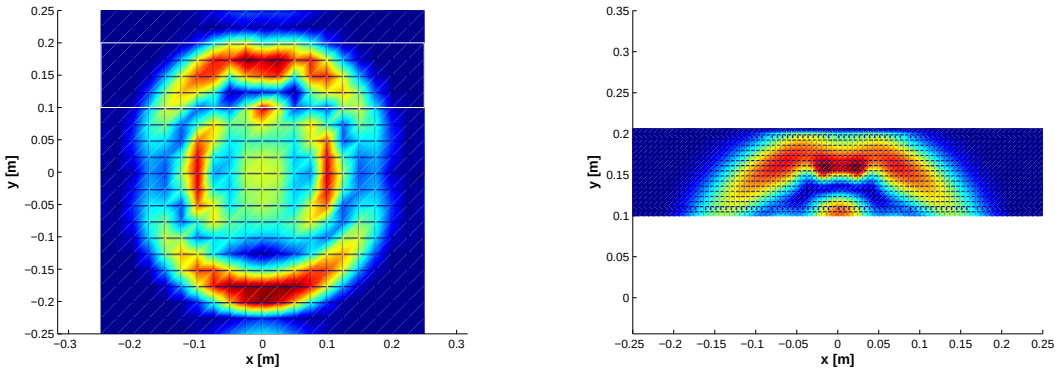

(a) Coarse-scale simulation

(b) Fine-scale simulation

Figure 99: Snapshot of incident travelling wave

clearly shows that the presence of the stiff inclusion is properly detected and provides a crisp picture of the reflection generation mechanism. The absence of spurious waves due to the scale interface, documented in fig. 98.a and 98.b. and the compatibility between the result in fig. 99.a with the one in fig. 99.b. suggest that the results are reliable. The fine-scale simulation provides an extremely precise representation of the wavefield and shows the extent of the defect.The accuracy of the bridging scales method is again quantified by the evolution of the total mechanical energy over the fine-scale region. The energy is normalized by its value at $t = 0$ and is plotted versus time in fig. 100.a and 100.b. for the damaged and undamaged cases, respectively. The plots show considerable agreement with the reference solution over a simulation interval corresponding to the time required by the pressure wave to reach the upper edge of the plate, be reflected and travel through the fine-scale region. Comparison of fig. 100.b with fig. 100.a also shows the presence of a defect: the returning wave is in fact associated with a slightly lower level of mechanical energy as a consequence of the localized reflection caused by the stiff inclusion.

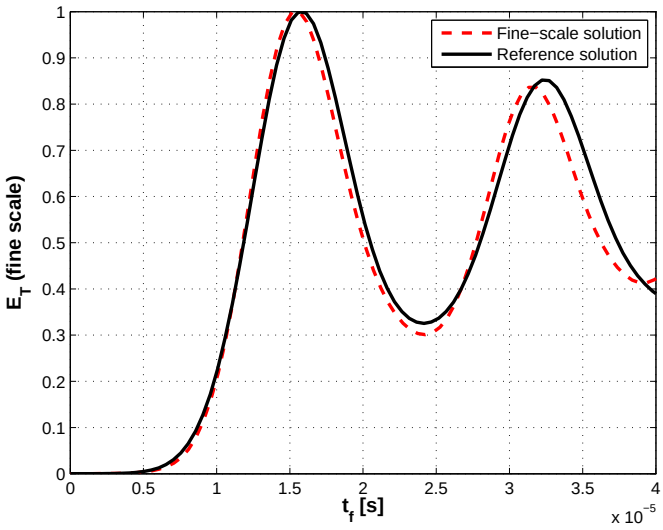

(a) Undamaged plate

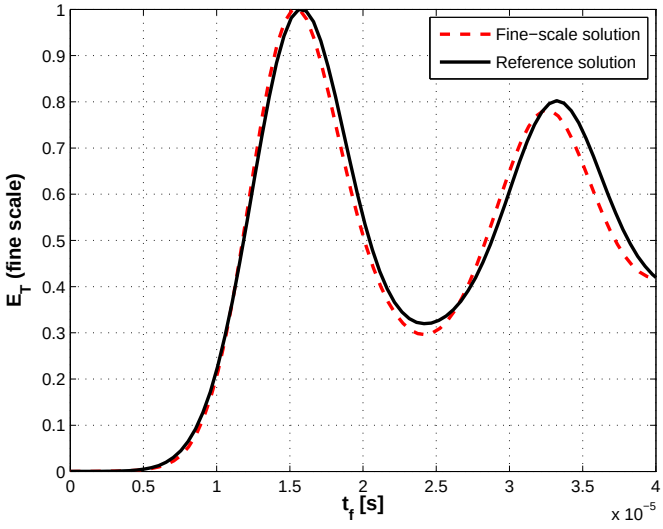

(b) Damaged plate

Figure 100: Energy-based accuracy test or bridging scales simulation

5.6 Conclusions

In this chapter the application of the bridging scales method to the analysis of wave propagation in solids is discussed. The bridging scales technique is adopted in an effort to make the simulation of wave motion affordable from a computational stand point without compromising on the quality of the results. The method is applied to one-dimensional as well as two-dimensional structures. In all cases the goal of reducing the computational size of the numerical model is achieved and the accuracy of the fine-scale solution is preserved with respect to a reference solution calculated by applying a detailed FE mesh over the entire domains. The capability of detecting discontinuities is also explored and shows interesting results in terms of reliability of the reflection phenomena visualized during the simulation.

The one-dimensional example of a bi-material rod is used to explore the application of the technique in conjunction with the homogenization method to the analysis of wave propagation in structures with multiple material phases. Homogenization is used to obtain equivalent properties used to model the heterogeneous structure as an equivalent continuum medium for the coarse-scale simulation, while a detailed fine-scale analysis is conducted over a region of the heterogeneous assembly. The limits of this analysis are dictated by the degree of compatibility between the original structure and the homogenized model. A relation can be established between the dispersive nature of the structure and the performance of the technique.

The rod example is also used to introduce a technique for the reduction of the computational time associated with the evaluation of the convolution integrals required by the method. The technique is based on the possibility to trigger the solution of the coupled equations only at instants when the wave is travelling through the region of interest, while relying on a simple coarse-scale analysis for all other stages. A considerable reduction of the simulation time is achieved and the effectiveness of the bridging scales method is improved.

CHAPTER VI

CONCLUDING REMARKS

6.1 Summary

This work has investigated the application of homogenization techniques to periodic solids with emphasis on lattices. Two homogenization techniques have been proposed for the analysis. The first one is a Fourier-based technique based on the evaluation of the symbol of the structure in the wavenumber domain. The second one involves a Taylor series expansion directly in the spatial domain. The two methods are equivalent, although the second one is to be preferred for complex assemblies as more prone to implementation. Both methods have been coupled with a finite element formulation of the unit cell which allows handling geometries of different complexity within a general framework.

Efforts have been devoted to the task of overcoming the limitations that the homogenization methods show for dynamic problems. Two techniques have been suggested to increase the accuracy of the method and extend its frequency region of applicability to the higher frequencies regime. The first one involves the correction of the coefficients of the homogenized equations of motion obtained by fitting the exact dispersion relations. The fitting process can be obtained from an exact unit cell analysis at very low cost and has been shown to improve dramatically the agreement between approximate and exact solutions. The second, called multi-cell technique, is based on the analysis of a macro-cell consisting of one or more neighboring unit cells. The homogenized models obtained through the multi-cell approach successfully approximate the short-wavelength limit.

The continuum PDEs obtained through the homogenization methods have also been used to estimate equivalent mechanical properties of lattices. The in-plane behavior of hexagonal and re-entrant honeycombs has been thoroughly investigated and the Taylor series-based technique has been used to calculate equivalent elastic parameters for a variety of honeycomb configurations. These values have been compared with published results

showing a high degree of accuracy. For some configurations it has been noted that the homogenization method allows overcoming shortcomings embedded in most analytical formulae available in the literature. The application has been extended to wave propagation problems where it has been shown that the homogenized equations can be used to correctly estimate the phase velocities for the low-frequency propagation modes.

The analysis of wave propagation in homogenized media has been furthermore investigated by using the bridging scales method to address the problem of modelling travelling waves in homogenized media with localized discontinuities. This multi-scale approach reduces the computational cost associated with a detailed finite element analysis and can yield considerable savings in CPU time. The effect of the mismatch between the homogenized model and the detailed periodic assembly has been explored and the lower limit of the frequency range of applicability for the technique has been investigated.

6.2 Conclusions

The first important insight that can be obtained from this work regards the potentials and the flexibility of a finite element description of lattice unit cells towards the formulation of a general homogenization technique. The matrix formulation that results from the FE description of the periodic assembly allows considering structures featuring different levels of complexity within one general framework and therefore carrying out the steps of the homogenization process as a sequence of *black box* operations.

It has been observed that, although structural complexity can be generally handled by the adopted technique, some important requirements on the internal organization of the unit cell are to be met. The derivation of homogenized PDEs having the form of an elasticity operator is in fact possible only when the unit cell behavior can be expressed in terms of the degrees of freedom of one reference node. This notion, which was learnt during the derivation of equivalent equations for the hexagonal lattice, has inspired the inclusion of condensation techniques in the FE model of the unit cell.

As far as the effectiveness of the dynamic homogenization method is concerned, a few

conclusions can be drawn from the results of Chapters II and III. The reduction of the computational cost associated with the numerical analysis of large lattices, which was introduced as one of the main motivations behind this work, can be achieved through the formulation of macro-elements based on the homogenized equations. The estimation of equivalent static properties can also be carried out with considerable agreement with reference analytical results. Symbolic expressions for the properties can be found with this approach only for relatively simple geometries, while the numerical identification has been shown to perform accurately for virtually all configurations. In the wave propagation context in which this work was conducted, the proposed technique presents higher capability than most existing analysis, since it also allows estimating dynamic quantities such as phase velocities.

Both homogenization approaches employed in this work are designed to operate in the long-wavelength limit, which in general coincides with the low-frequency regime for most lattices. The solution methods can be refined to extend the range of approximation to include higher frequencies. The implementations performed in this work have shown that the feasibility of the refinement highly depends on the complexity of the differential equations, and therefore on the family of lattice considered, and not that much on the internal configuration of the unit cell.

6.2.1 Challenges remained unsolved and potentials of application

The distinctive goal of this work is the exploration of a wide range of analysis tools and of their combined use through the application to fairly simple test problems. Among the challenges that sill remain to be solved, most regard the extension of the proposed techniques to structures of greater complexity, such as three-dimensional periodic assemblies. From a theoretical stand point, such extension should follow from the same mathematical outline, but the effects of additional geometric complexity might raise practical issues to be addressed on a case-to-case basis. The multi-cell technique, in particular, has been limited in this work to one-dimensional applications, and so has the study of the effects of the approximation embedded in the homogenization method upon the reliability of the bridging scales method. Lastly, the extension to complex assemblies would require the integration of the presented

formulation with some commercial FE software packages, like ANSYS® or ABAQUS®.

6.3 Future Work

6.3.1 Homogenization techniques

The main objective of this work is to explore the potentials of the homogenization method outside the field of static analysis for which it was originally designed. This has been done by applying the technique to a variety of dynamic and wave propagation problems. Emphasis has been placed on the width of the spectrum of application rather than on the complexity of the single examples. However, each of the suggested techniques can be extended to more complicated assemblies, taking advantage of the generality of the proposed formulation. Solids of interest with high structural complexity include three-dimensional lattices, multi-phase materials, composites, sandwich panels. The homogenization technique could also be coupled with statistical calculations to model non-deterministic assemblies such as foams.

The multi-cell analysis discussed in Chapter IV has proved to be very effective at providing multiple sets of approximating PDEs for periodic lattices. In this work its applicability has been limited for simplicity to one-dimensional lattices. Future research extend the technique to two-dimensional and three-dimensional structures.

6.3.2 Bridging scales method

The original formulation of the bridging scales method [49] was originally developed for non-linear systems, which, however, requires the linearization of the equations of motion about equilibrium configurations. Future work could be done towards exploring the application to nonlinear problems and the consequent necessary changes in the procedure.

Another possible expansion of the work might involve the development of an adaptive bridging scales technique, consisting of a multi-scale bridging method where the location, size and shape of the fine scale window can change in time in order to follow the evolution of a particular phenomenon. An interesting application could be the analysis of crack propagation in solids: the fine scale window would have to be limited to the region immediately around the moving crack front, where a very detailed mesh is needed to pick up the propagation phenomenon. The localized energy associated with the existence of the crack

itself could be used as a threshold to trigger the superposition of the fine-scale window to the coarse scale when needed.

Multi-scale simulations actually combining lattice structures and homogenized models could also be run for systems with internal complexity higher than those presented in this work. The challenge of this research would lie in the development of a general and reliable formulation capable of providing the time kernel history functions for the considered assemblies.

CHAPTER VII

APPENDICES

7.1 APPENDIX A - Derivation of the Discrete Symbol for a Two-dimensional Domain

Let us consider a two-dimensional domain. Each node is defined by a pair of integers n and m. Let $\mathbf{u}(n,m)$ and $\mathbf{f}(n,m)$ be the array of nodal displacements and the array of forces acting on the node in position (n,m), respectively. The equations of motion for the selected node can be written in convolution form as:

$$\sum_{n'=-n-1}^{n+1}\sum_{m'=-m-1}^{m+1}\mathbf{D}(n-n',m-m')\mathbf{u}(n',m')=\mathbf{f}(n,m) \tag{213}$$

where $\mathbf{D}$ is here a dynamic stiffness matrix defined as:

$$\mathbf{D}=\mathbf{K}-\omega^2\mathbf{M} \tag{214}$$

with $\mathbf{K}$ and $\mathbf{K}$ being the stiffness and mass matrices, respectively. The two-dimensional discrete Fourier Transforms of nodal displacements and nodal forces are:

$$\hat{\mathbf{u}}(p,q)=\sum_{n=0}^{N}\sum_{m=0}^{M}\mathbf{u}(n,m)e^{-i2\pi\left[\frac{pn}{N+1}+\frac{qm}{M+1}\right]} \tag{215}$$

$$\hat{\mathbf{f}}(p,q)=\sum_{n=0}^{N}\sum_{m=0}^{M}\mathbf{f}(n,m)e^{-i2\pi\left[\frac{pn}{N+1}+\frac{qm}{M+1}\right]} \tag{216}$$

where N and M are the number of cells along the x and y directions, respectively. Applying the transformations in eq. (215) and eq. (216) to both sides of eq. (213), yields

$$\sum_{n=0}^{N}\sum_{m=0}^{M}\sum_{n'=-n-1}^{n+1}\sum_{m'=-m-1}^{m+1}\mathbf{D}(n-n',m-m')\mathbf{u}(n',m')e^{-i2\pi\left[\frac{pn}{N+1}+\frac{qm}{M+1}\right]}=\hat{\mathbf{f}}(p,q) \tag{217}$$

The left hand side of the last equation can be manipulated as:

$$\sum_{n=0}^{N}\sum_{m=0}^{M}\sum_{n'=-n-1}^{n+1}\sum_{m'=-m-1}^{m+1}\mathbf{D}(n-n',m-m')e^{-i2\pi\left[\frac{p(n-n')}{N+1}+\frac{q(m-m')}{M+1}\right]}\mathbf{u}(n',m')e^{-i2\pi\left[\frac{p(n')}{N+1}+\frac{q(m')}{M+1}\right]} \tag{218}$$

Introducing the auxiliary variables s and r

$$s = n - n' \tag{219}$$

$$r = m - m' \tag{220}$$

eq. (218) becomes:

$$\sum_{n=0}^{N}\sum_{m=0}^{M}\sum_{s=-1}^{1}\sum_{r=-1}^{1}\mathbf{D}(s,r)e^{-i2\pi\left[\frac{ps}{N+1}+\frac{qr}{M+1}\right]}\mathbf{u}(n-s,m-r)e^{-i2\pi\left[\frac{p(n-s)}{N+1}+\frac{q(m-r)}{M+1}\right]} \tag{221}$$

The periodicity of the domain along x and y can be used at this point to write

$$\sum_{n=0}^{N}\sum_{m=0}^{M}\mathbf{u}(n-s,m-r)e^{-i2\pi\left[\frac{p(n-s)}{N+1}+\frac{q(m-r)}{M+1}\right]} = \sum_{n=0}^{N}\sum_{m=0}^{M}\mathbf{u}(n,m)e^{-i2\pi\left[\frac{pn}{N+1}+\frac{qm}{M+1}\right]} = \hat{\mathbf{u}}(p,q) \tag{222}$$

where the last equality follows from the definition of eq. (216). The equations of motion in the Fourier space can then be written as

$$\mathbf{\Gamma}(p,q)\hat{\mathbf{u}}(p,q) = \hat{\mathbf{f}}(p,q) \tag{223}$$

where the quantity $\mathbf{\Gamma}(p,q)$ is the symbol of the considered domain defined as:

$$\mathbf{\Gamma}(p,q) = \sum_{n'=n-1}^{n+1}\sum_{m'=m-1}^{m+1}\mathbf{D}(n-n',m-m')e^{-i2\pi\left[\frac{p(n-n')}{N+1}+\frac{q(m-m')}{M+1}\right]} \tag{224}$$

The non-trivial consideration out of the last result is that, while the Fourier Transform of $\mathbf{u}$ and $\mathbf{f}$ involves a summation over the whole domain, the symbol is obtained from the dynamic stiffness matrix through a local cell analysis with contributions from the neighboring elements only. The quantities $-i2\pi\left[\frac{p(n-n')}{N+1}\right]$ and $-i2\pi\left[\frac{q(m-m')}{M+1}\right]$ can be read respectively as $-i(n-n')\xi_1$ ad $-i(m-m')\xi_2$ and eq. (223) can be recast in terms of ξ_1 and ξ_2 as:

$$\mathbf{\Gamma}(\xi_1,\xi_2)\hat{\mathbf{u}}(\xi_1,\xi_2) = \hat{\mathbf{f}}(\xi_1,\xi_2) \tag{225}$$

For the sake of completeness, it can also be noted that, by means of Bloch's theorem,

$$\mathbf{u}(n-n',m-m') = \mathbf{u}(n,m)e^{-i[(n-n')\xi_1+(m-m')\xi_2]} \tag{226}$$

Substituting eq. (226) in the homogeneous part of eq. (213) yields the expression for the dispersion relation as used in Chapter II.

$$\left[\sum_{n'=-n-1}^{n+1}\sum_{m'=-m-1}^{m+1}\mathbf{D}(n-n',m-m')e^{-i[(n-n')\xi_1+(m-m')\xi_2]}\right]\mathbf{u}(n,m) = \mathbf{0} \tag{227}$$

7.2 APPENDIX B - Equivalence of Fourier-based and Direct Taylor Series-based Homogenization Techniques

Let us consider the convolution form of the equations of motion for node $(0,0)$ under the assumption of lumped mass. They read:

$$\sum_{m,n=-1}^{+1} \mathbf{K}^{(m,n)}\mathbf{u}^{(m,n)} - \omega^2\mathbf{M}^{(0,0)}\mathbf{u}^{(0,0)} = \mathbf{f}^{(0,0)} \tag{228}$$

Approximation is introduced by letting:

$$\mathbf{u}^{(m,n)} \approx \boldsymbol{u}(\eta_1,\eta_2) + m\frac{\partial \boldsymbol{u}}{\partial \eta_1} + n\frac{\partial \boldsymbol{u}}{\partial \eta_2} + \frac{1}{2}m^2\frac{\partial^2 \boldsymbol{u}}{\partial \eta_1^2} + \frac{1}{2}n^2\frac{\partial^2 \boldsymbol{u}}{\partial \eta_2^2} + mn\frac{\partial^2 \boldsymbol{u}}{\partial \eta_1 \partial \eta_2} + ... \tag{229}$$

where $\boldsymbol{u}$ is now a continuous variable. Transforming eq. (228) in the Fourier domain, yields:

$$\sum_{m,n=-1}^{+1} \mathbf{K}^{(m,n)}\hat{\mathbf{u}}(\xi_1,\xi_2) - \omega^2\mathbf{M}^{(0,0)}\hat{\mathbf{u}}(\xi_1,\xi_2) = \hat{\mathbf{f}}(\xi_1,\xi_2) \tag{230}$$

where $\hat{\mathbf{u}}(\xi_1,\xi_2)$ is the Fourier transform of $\mathbf{u}^{(m,n)}$ which, from eq. (229), can be expressed as:

$$\hat{\mathbf{u}}(\xi_1,\xi_2) \approx \hat{\boldsymbol{u}} - im\xi_1\hat{\boldsymbol{u}} - in\xi_2\hat{\boldsymbol{u}} + \frac{1}{2}m^2\xi_1^2\hat{\boldsymbol{u}} + \frac{1}{2}n^2\xi_2^2\hat{\boldsymbol{u}} + \ldots\mathcal{O}(\xi^p) \tag{231}$$

The expression in eq. (230), upon substitution of eq. (231), assumes the following form.

$$\left[\sum_{m,n=-1}^{+1} \mathbf{K}^{(m,n)}\left(1 - im\xi_1\hat{\boldsymbol{u}} - in\xi_2\hat{\boldsymbol{u}} + \frac{1}{2}m^2\xi_1^2\hat{\boldsymbol{u}} + \frac{1}{2}n^2\xi_2^2\hat{\boldsymbol{u}} + \ldots\mathcal{O}(\xi^p)\right) + \right. \tag{232}$$

$$\left. -\omega^2\mathbf{M}^{(0,0)}\right]\hat{\boldsymbol{u}}(\xi_1,\xi_2) = \hat{\boldsymbol{f}}(\xi_1,\xi_2)$$

Equation. (232) can be expressed in compact form as:

$$[\boldsymbol{S}^{(p)}]\hat{\boldsymbol{u}}(\xi_1,\xi_2) = \hat{\boldsymbol{f}}(\xi_1,\xi_2) \tag{233}$$

where $\boldsymbol{S}^{(p)}$ is the polynomial of order p retained after truncation of the expression in eq. (231). This quantity coincides with the symbol of the structure upon Taylor series expansion introduced above. This shows the equivalence between the Fourier-based technique and the approach based on direct Taylor series expansion in the spatial domain.

7.3 APPENDIX C - Derivation of Bridging Interpolation Matrix Q

Let us consider the array of nodal displacements $\mathbf{u}$. We can enforce the following:

$$\mathbf{u} = \bar{\mathbf{u}} + \mathbf{q} - \mathbf{P}\mathbf{q} \tag{234}$$

where $\bar{\mathbf{u}}$ is the coarse-scale solution interpolated at the fine-scale nodal positions, $\mathbf{q}$ is the fine-scale solution and $\mathbf{P}\mathbf{q}$ is a bridging scale term whose purpose is to subtract from $\mathbf{q}$ the information shared between the scales through a projection operator $\mathbf{P}$ yet to be determined at this point. Since $\mathbf{u} = \bar{\mathbf{u}} + \mathbf{u}'$ still holds, the following can be written

$$\mathbf{u}' = \mathbf{Q}\mathbf{q} \tag{235}$$

where

$$\mathbf{Q} = \mathbf{I} - \mathbf{P} \tag{236}$$

with $\mathbf{I}$ being an identity matrix of size $n_f \times n_f$. The projection operator $\mathbf{P}$ is to be selected to minimize the mass weighted least square error between $\mathbf{q}$ and its projection $\mathbf{P}\mathbf{q}$. The technique consists of selecting the displacement field $\mathbf{w}$ such that the error defined as

$$E \triangleq (\mathbf{q} - \mathbf{N}\mathbf{w})^T \mathbf{M}_f (\mathbf{q} - \mathbf{N}\mathbf{w}) \tag{237}$$

has a minimum. Performing the minimization yields the following displacement field:

$$\mathbf{w} = \mathbf{M}^{-1}\mathbf{N}^T\mathbf{M}_f\mathbf{q} \tag{238}$$

The meaning of matrices $\mathbf{M}_f$ and $\mathbf{M}$ has been widely discussed in Chapter V. Matrix $\mathbf{N}$ can now be used to interpolate the found field $\mathbf{w}$ at the fine-scale nodal locations. In formulae:

$$\mathbf{P}\mathbf{q} = \mathbf{N}\mathbf{w} = \mathbf{N}\mathbf{M}^{-1}\mathbf{N}^T\mathbf{M}_f\mathbf{q} \tag{239}$$

$$\mathbf{Q} = \mathbf{I} - \mathbf{N}\mathbf{w} = \mathbf{N}\mathbf{M}^{-1}\mathbf{N}^T\mathbf{M}_f \tag{240}$$

REFERENCES

[1] Achenbach, J., *Wave propagation in elastic solids*. North Holland, 1999.

[2] Babuska, I., "The computational aspects of the homogenization problem," *Third International Symposium on Computing Methods in Applied Sciences and Engineering*, vol. I, pp. 309 – 16, 1979.

[3] Bakhvalov, N., Panasenko, G., and Eglit, M., "The effective properties of structures and composites with inclusions in the form of walls and rods," *Computational Mathematics and Mathematical Physics*, vol. 36, no. 12, pp. 1701 – 6, 1996.

[4] Belytschko, T., Fish, J., and Bayliss, A., "Spectral overlay on finite elements for problems with high gradients," *Computer Methods in Applied Mechanics and Engineering*, vol. 81, no. 1, pp. 71 – 89, 1990.

[5] Belytschko, T., Liu, W., and Moran, B., *Nonlinear finite elements for continua and structures*. Chichester, UK: Wiley, 2001.

[6] Bendsoe, M. and Kikuchi, N., "Generating optimal topologies in structural design using a homogenization method," *Computer Methods in Applied Mechanics and Engineering*, vol. 71, no. 2, pp. 197 – 224, 1988.

[7] Bensoussan, A., Lions, J., and Papanicolaou, G., "Asymptotic analysis for periodic structures," pp. xxiv+700, 1978.

[8] Boutin, C., "Microstructural effects in elastic composites," *International Journal of Solids and Structures*, vol. 33, no. 7, pp. 1023 – 51, 1996.

[9] Boutin, C. and Auriault, J., "Rayleigh scattering in elastic composite materials," *International Journal of Engineering Science*, vol. 31, no. 12, pp. 1669 – 1689, 1993.

[10] Brillouin, L., *Wave Propagation in Periodic Structures*. New York: Dover, 1953.

[11] Brown, G. and Byrne, K., "Determining the response of innite, one-dimensional, non-uniform peri- odic structures by substructuring using waveshapes coordinates," *Journal of Sound and Vibration*, vol. 287, pp. 505 – 523, 2005.

[12] Chen, W. and Fish, J., "A dispersive model for wave propagation in periodic heterogeneous media based on homogenization with multiple spatial and temporal scales," *Transactions of the ASME. Journal of Applied Mechanics*, vol. 68, no. 2, pp. 153 – 61, 2001.

[13] Cook, R., Malkus, D., Plesha, M., and Witt, R., *Concepts and applications of finite element analysis*. New York, NY: Wiley, 2001.

[14] Drumheller, D. S. and Bedford, A., "Wave propagation in elastic laminates using a second order microstructure theory.," *International Journal of Solids and Structures*, vol. 10, no. 1, pp. 61 – 76, 1974.

[15] Fish, J. and Belsky, V., "Multi-grid method for periodic heterogeneous media. 2. multiscale modeling and quality control in multidimensional case," *Computer Methods in Applied Mechanics and Engineering*, vol. 126, no. 1-2, pp. 17 – 38, 1995.

[16] Fish, J. and Chen, W., "Higher-order homogenization of initial/boundary-value problem," *Journal of Engineering Mechanics*, vol. 127, no. 12, pp. 1223 – 1230, 2001.

[17] Fish, J. and Belsky, V., "Multigrid method for periodic heterogeneous media part 1: Convergence studies for one-dimensional case," *Computer Methods in Applied Mechanics and Engineering*, vol. 126, no. 1-2, pp. 1 – 16, 1995.

[18] Fish, J. and Chen, W., "Rve-based multilevel method for periodic heterogeneous media with strong scale mixing," *Journal of Engineering Mathematics*, vol. 46, no. 1, pp. 87 – 106, 2003.

[19] Fish, J. and Chen, W., "Rve-based multilevel method for periodic heterogeneous media with strong scale mixing," *Journal of Engineering Mathematics*, vol. 46, no. 1, pp. 87 – 106, 2003.

[20] Fish, J., Chen, W., and Nagai, G., "Non-local dispersive model for wave propagation in heterogeneous media: Multi-dimensional case," *International Journal for Numerical Methods in Engineering*, vol. 54, no. 3, pp. 347 – 363, 2002.

[21] Fish, J., Chen, W., and Nagai, G., "Non-local dispersive model for wave propagation in heterogeneous media: One-dimensional case," *International Journal for Numerical Methods in Engineering*, vol. 54, no. 3, pp. 331 – 346, 2002.

[22] Fish, J., Shek, K., Pandheeradi, M., and Shephard, M. S., "Computational plasticity for composite structures based on mathematical homogenization: theory and practice," *Computer Methods in Applied Mechanics and Engineering*, vol. 148, no. 1-2, pp. 53 – 73, 1997.

[23] Fish, J. and Wagiman, A., "Multiscale finite element method for a locally nonperiodic heterogeneous medium," *Computational Mechanics*, vol. 12, no. 3, pp. 164 – 180, 1993.

[24] Friis, E., Lakes, R., and Park, J., "Negative poisson's ratio polymeric and metallic foams," *Journal of Materials Science*, vol. 23, no. 12, pp. 4406 – 4414, 1988.

[25] Ghosh, S. and Mukhopadhyay, S. N., "Material based finite element analysis of heterogeneous media involving dirichlet tessellations," *Computer Methods in Applied Mechanics and Engineering*, vol. 104, no. 2, pp. 211 – 247, 1993.

[26] Gibson, L. and Ashby, F., *Cellular solids. Structures and properties.* Cambridge, UK: Cambridge University Press, 2001.

[27] Gonella, S. and Ruzzene, M., "Homogenization of vibrating periodic lattice structures," *Applied Mathematical Modelling.*

[28] Guedes, J. M. and Kikuchi, N., "Preprocessing and postprocessing for materials based on the homogenization method with adaptive finite element methods," *Computer Methods in Applied Mechanics and Engineering*, vol. 83, no. 2, pp. 143 – 198, 1990.

[29] Guedes, J. M. and Kikuchi, N., "Preprocessing and postprocessing for materials based on the homogenization method with adaptive finite element methods," *Computer Methods in Applied Mechanics and Engineering*, vol. 83, no. 2, pp. 143 – 198, 1990.

[30] Hassani, B. and Hinton, E., "Review of homogenization and topology optimization i - homogenization theory for media with periodic structure," *Computers and Structures*, vol. 69, no. 6, pp. 707 – 717, 1998.

[31] Hassani, B. and Hinton, E., "Review of homogenization and topology optimization ii - analytical and numerical solution of homogenization equations," *Computers and Structures*, vol. 69, no. 6, pp. 719 – 738, 1998.

[32] Hassani, B. and Hinton, E., "Review of homogenization and topology optimization iii - topology optimization using optimality criteria," *Computers and Structures*, vol. 69, no. 6, pp. 739 – 756, 1998.

[33] Hollister, S. and Kikuchi, N., "Comparison of homogenization and standard mechanics analyses for periodic porous composites," *Computational Mechanics*, vol. 10, no. 2, pp. 73 – 95, 1992.

[34] Hollister, S. and Kikuchi, N., "Homogenization theory and digital imaging: a basis for studying the mechanics and design principles of bone tissue," *Biotechnology and Bioengineering*, vol. 43, no. 7, pp. 586 – 596, 1994.

[35] Hollister, S. and Kikuchi, N., "Homogenization theory and digital imaging: a basis for studying the mechanics and design principles of bone tissue," *Biotechnology and Bioengineering*, vol. 43, no. 7, pp. 586 – 596, 1994.

[36] Hussein, M. I., Hulbert, G. M., and Scott, R. A., "Band-gap engineering of elastic waveguides using periodic materials," *American Society of Mechanical Engineers, Design Engineering Division (Publication) DE*, vol. 116, no. 2, pp. 799 – 807, 2003.

[37] Jeong, S. M. and Ruzzene, M., "Analysis of vibration and wave propagation in cylindrical grid-like structures," *Shock and Vibration*, vol. 11, no. 3-4, pp. 311 – 331, 2004.

[38] Kadowaki, H. and Liu, W. K., "Bridging multi-scale method for localization problems," *Computer Methods in Applied Mechanics and Engineering*, vol. 193, no. 30-32, pp. 3267 – 3302, 2004.

[39] Kadowaki, H. and Liu, W. K., "A multiscale approach for the micropolar continuum model," *Laser Physics*, vol. 15, no. 3, pp. 269 – 282, 2005.

[40] Kam Liu, W., Karpov, E., and Stephen, N., "Initial tension in randomly disordered periodic lattices," *International Journal of Solids and Structures*, vol. 40, no. 20, pp. 5371 – 5388, 2003.

[41] Karpov, E., Liu, W., and Park, H., *Nano Mechanics and Materials*. Chichester, UK: Wiley, 2006.

[42] Karpov, E., Stephen, N., and Dorofeev, D., "On static analysis of finite repetitive structures by discrete fourier transform," *International Journal of Solids and Structures*, vol. 39, no. 16, pp. 4291 – 4310, 2002.

[43] Knap, J. and Ortiz, M., "An analysis of the quasicontinuum method," *Journal of the Mechanics and Physics of Solids*, vol. 49, no. 9, pp. 1899 – 1923, 2001.

[44] Lakes, R., "Elastic and viscoelastic behavior of chiral materials," *International Journal of Mechanical Sciences*, vol. 43, no. 7, pp. 1579 – 1589, 2001.

[45] Langley, R., "Response of two-dimensional periodic structures to point harmonic forcing," *Journal of Sound and Vibration*, vol. 197, no. 4, pp. 447 – 469, 1996.

[46] Larsen, U. D., Sigmund, O., and Bouwstra, S., "Design and fabrication of compliant micromechanisms and structures with negative poisson's ratio," *Proceedings of the IEEE Micro Electro Mechanical Systems (MEMS)*, pp. 365 – 371, 1996.

[47] Lee, U., "Equivalent continuum models of large platelike lattice structures," *International Journal of Solids and Structures*, vol. 31, no. 4, pp. 457 – 467, 1994.

[48] Lions, J.-L., "Some methods of resolution of free surface problems," *Proceedings of the 5th International Conference on Numerical Methods in Fluid Dynamics*, pp. 1 – 31, 1976.

[49] Liu, W. K., Park, H. S., Qian, D., Karpov, E. G., Kadowaki, H., and Wagner, G. J., "Bridging scale methods for nanomechanics and materials," *Computer Methods in Applied Mechanics and Engineering*, vol. 195, no. 13-16, pp. 1407 – 1421, 2006.

[50] Liu, W., Chen, Y., Chang, C., and Belytschko, T., "Advances in multiple scale kernel particle methods," *Computational Mechanics*, vol. 18, no. 2, pp. 73 – 111, 1996.

[51] Liu, W., Karpov, E., Zhang, S., and Park, H., "An introduction to computational nanomechanics and materials," *Computer Methods in Applied Mechanics and Engineering*, vol. 193, no. 17-20, pp. 1529 – 1578, 2004.

[52] Maewal, A., "Construction of models of dispersive elastodynamic behavior of periodic composites: A computational approach.," *Computer Methods in Applied Mechanics and Engineering*, vol. 57, no. 2, pp. 191 – 205, 1986.

[53] Martinsson, P.-G. and Rodin, G., "Asymptotic expansions of lattice green's functions," *Proceedings of the Royal Society of London, Series A (Mathematical, Physical and Engineering Sciences)*, vol. 458, no. 2027, pp. 2609 – 22, 2002.

[54] Martinsson, P., *Fast Multiscale Methodos for Lattice Equations*. PhD thesis, University of texas at Austin, 2002.

[55] Martinsson, P. and Movchan, A., "Vibrations of lattice structures and phononic band gaps," *Quarterly Journal of Mechanics and Applied Mathematics*, vol. 56, no. 1, pp. 45 – 64, 2003.

[56] McDevitt, T. W., Hulbert, G. M., and Kikuchi, N., "Plane harmonic wave propagation in three-dimensional composite media," *Finite Elements in Analysis and Design*, vol. 33, no. 4, pp. 263 – 282, 1999.

[57] McDevitt, T., *Elastodynamics and Wave Propagation in Periodic Structures*. PhD thesis, University of Michigan, 1998.

[58] McDevitt, T., Hulbert, G., and Kikuchi, N., "An assumed strain method for the dispersive global-local modeling of periodic structures," *Computer Methods in Applied Mechanics and Engineering*, vol. 190, no. 48, pp. 6425 – 40, 2001.

[59] Meirovitch, L., *Analytical Methods in Vibrations*. New York: MacMillan Publishers Ltd., 1967.

[60] Miller, R., Ortiz, M., Phillips, R., Shenoy, V., and Tadmor, E., "Quasicontinuum models of fracture and plasticity," *Engineering Fracture Mechanics*, vol. 61, no. 3-4, pp. 427 – 444, 1998.

[61] Miller, R., Tadmor, E., Phillips, R., and Ortiz, M., "Quasicontinuum simulation of fracture at the atomic scale," *Modelling and Simulation in Materials Science and Engineering*, vol. 6, no. 5, pp. 607 – 638, 1998.

[62] Murakami, H., "Mixure theory for wave propagation in angle-ply laminates. part 1: Theory.," *Journal of Applied Mechanics, Transactions ASME*, vol. 52, no. 2, pp. 331 – 337, 1985.

[63] Murakami, H. and Akiyama, A., "Mixture theory for wave propagation in angle-ply laminates. part 2: Application.," *Journal of Applied Mechanics, Transactions ASME*, vol. 52, no. 2, pp. 338 – 344, 1985.

[64] Murakami, H. and Hegemier, G. A., "Mixture model for unidirectionally fiber-reinforced composites.," *Journal of Applied Mechanics, Transactions ASME*, vol. 53, no. 4, pp. 765 – 773, 1986.

[65] Nair, P. S. and Durvasula, S., "On quasi-degeneracies in plate vibration problems.," *International Journal of Mechanical Sciences*, vol. 15, no. 12, pp. 975 – 986, 1973.

[66] Noor, A., "Continuum modeling for repetitive lattice structures," *Applied Mechanics Reviews*, vol. 41, no. 7, pp. 285 – 296, 1988.

[67] Oden, J., Vemaganti, K., and Moes, N., "Hierarchical modeling of heterogeneous solids," *Computer Methods in Applied Mechanics and Engineering*, vol. 172, no. 1-4, pp. 3 – 25, 1999.

[68] Park, H. S. and Liu, W. K., "An introduction and tutorial on multiple-scale analysis in solids," *Computer Methods in Applied Mechanics and Engineering*, vol. 193, no. 17-20, pp. 1733 – 1772, 2004.

[69] Perkins, N. C. and Mote, C. D. J., "Comments on curve veering in eigenvalue problems.," *Journal of Sound and Vibration*, vol. 106, no. 3, pp. 451 – 463, 1986.

[70] Piltner, R., "Special finite elements with holes and internal cracks.," *International Journal for Numerical Methods in Engineering*, vol. 21, no. 8, pp. 1471 – 1485, 1985.

[71] Prall, D. and Lakes, R., "Properties of a chiral honeycomb with a poisson's ratio of -1," *International Journal of Mechanical Sciences*, vol. 39, no. 3, pp. 305 – 14, 1997/03/.

[72] Rank, E. and Krause, R., "Multiscale finite-element method," *Computers and Structures*, vol. 64, no. 1-4, pp. 139 – 144, 1997.

[73] Reddy, J., *An introduction to the finite element method*. New York: McGraw-Hill, 1993.

[74] Ruzzene, M., Scarpa, F., and Soranna, F., "Wave beaming effects in two-dimensional cellular structures," *Smart Materials and Structures*, vol. 12, no. 3, pp. 363 – 372, 2003.

[75] Sanchez-Palencia, E., "Non-homogeneous media and vibration theory," pp. ix+398, 1980.

[76] Shenoy, V., Miller, R., Tadmor, E., Phillips, R., and Ortiz, M., "Quasicontinuum models of interfacial structure and deformation," *Physical Review Letters*, vol. 80, no. 4, pp. 742 –, 1998.

[77] Shenoy, V., Miller, R., Tadmor, E., Rodney, D., Phillips, R., and Ortiz, M., "Adaptive finite element approach to atomic-scale mechanics - the quasicontinuum method," *Journal of the Mechanics and Physics of Solids*, vol. 47, no. 3, pp. 611 – 642, 1999.

[78] Sigmund, O. and Jensen, J., "Systematic design of phononic band-gap materials and structures by topology optimization," *Philosophical Transactions of the Royal Society London, Series A (Mathematical, Physical and Engineering Sciences)*, vol. 361, no. 1806, pp. 1001 – 19, 2003.

[79] Sigmund, O. and Torquato, S., "Design of materials with extreme thermal expansion using a three-phase topology optimization method," *Journal of the Mechanics and Physics of Solids*, vol. 45, no. 6, pp. 1037 – 1067, 1997.

[80] Srikantha Phani, A., Woodhouse, J., and Fleck, N., "Wave propagation in two-dimensional periodic lattices," *Journal of the Acoustical Society of America*, vol. 119, no. 4, pp. 1995 – 2005, 2006.

[81] Suiker, A., Metrikine, A., and de Borst, R., "Comparison of wave propagation characteristics of the cosserat continuum model and corresponding discrete lattice models," *International Journal of Solids and Structures*, vol. 38, no. 9, pp. 1563 – 1583, 2001.

[82] Sun, C., Achenbach, J., and Herrmann, G., "Continuum theory for laminated medium," *American Society of Mechanical Engineers – Papers*, pp. 9 –, 1968.

[83] Tadmor, E., Ortiz, M., and Phillips, R., "Quasicontinuum analysis of defects in solids," *Philosophical Magazine A: Physics of Condensed Matter, Structure, Defects and Mechanical Properties*, vol. 73, no. 6, pp. 1529 – 1563, 1996.

[84] Thorp, O., Ruzzene, M., and Baz, A., "Attenuation of wave propagation in fluid-loaded shells with periodic shunted piezoelectric rings," *Smart Materials and Structures*, vol. 14, no. 4, pp. 594 – 604, 2005.

[85] Vasiliev, A., Dmitriev, S., Ishibashi, Y., and Shigenari, T., "Elastic properties of a two-dimensional model of crystals containing particles with rotational degrees of freedom," *Physical Review B (Condensed Matter and Materials Physics)*, vol. 65, no. 9, pp. 094101 – 1, 2002.

[86] Vasiliev, A., Dmitriev, S., and Miroshnichenko, A., "Multi-field continuum theory for medium with microscopic rotations," *International Journal of Solids and Structures*, vol. 42, no. 24, pp. 6245 – 6260, 2005.

[87] Wagner, G., Karpov, E., and Liu, W., "Molecular dynamics boundary conditions for regular crystal lattices," *Computer Methods in Applied Mechanics and Engineering*, vol. 193, no. 17-20, pp. 1579 – 601, 2004.

[88] Wagner, G. and Liu, W., "Coupling of atomistic and continuum simulations using a bridging scale decomposition," *Journal of Computational Physics*, vol. 190, no. 1, pp. 249 – 74, 2003.

[89] Wagner, G. J., Karpov, E. G., and Liu, W. K., "Molecular dynamics boundary conditions for regular crystal lattices," *Computer Methods in Applied Mechanics and Engineering*, vol. 193, no. 17-20, pp. 1579 – 1601, 2004.

[90] Weeks, W., "Numerical inversion of laplace transforms using laguerre functions," *Journal of the Association for Computating Machinery*, vol. 13, no. 3, p. 419, 1966.

[91] Weideman, J., "Algorithms for parameter selection in the weeks method for inverting the laplace transform," *SIAM Journal on Scientific Computing*, vol. 21, no. 1, pp. 111–128, 1999.

[92] Xiao, S. and Belytschko, T., "A bridging domain method for coupling continua with molecular dynamics," *Computer Methods in Applied Mechanics and Engineering*, vol. 193, no. 17-20, pp. 1645 – 1669, 2004.